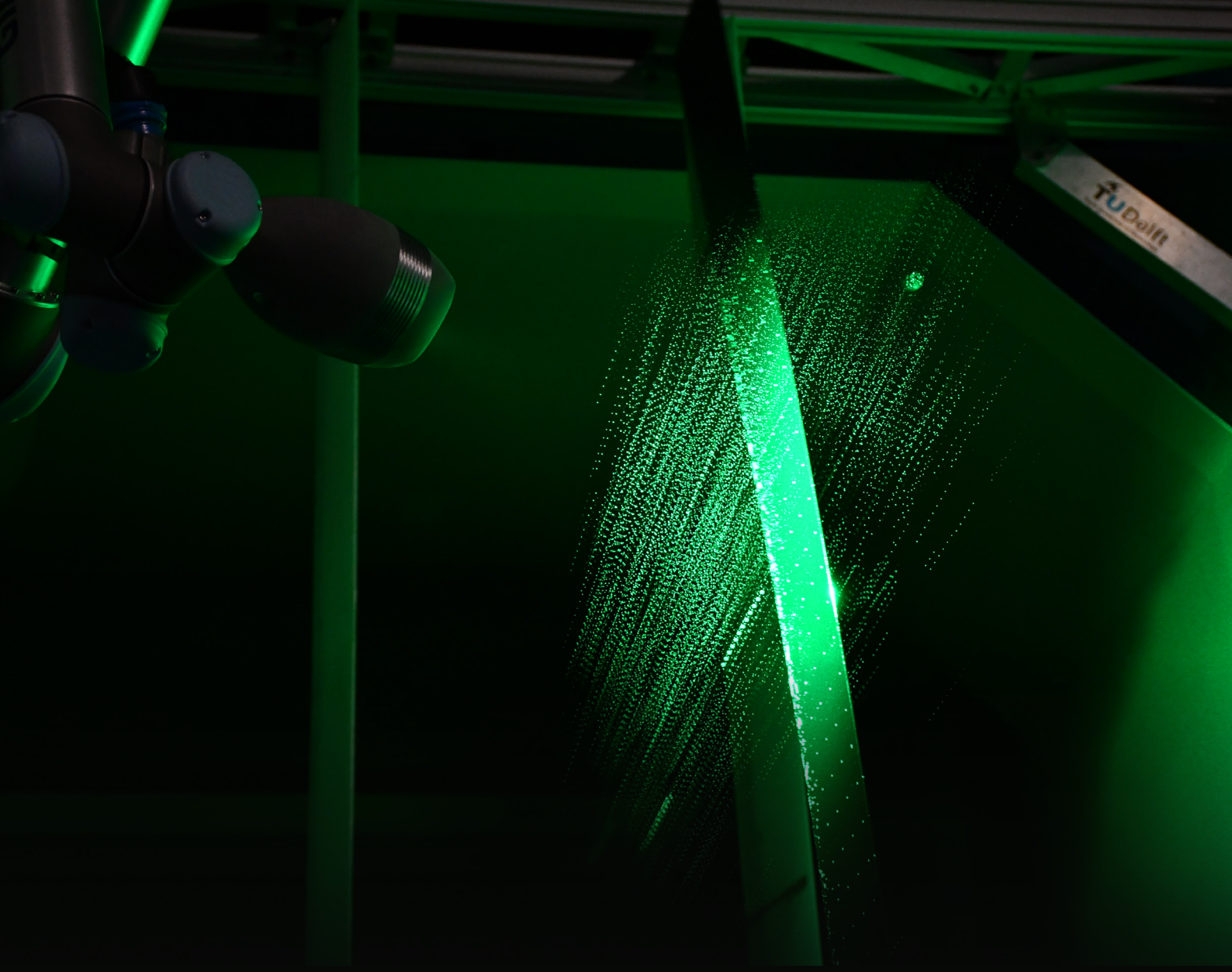

Experimental Fluid-Structure Interaction of a Flexible Plate Under Gust Excitation

A Wind-tunnel Investigation by Means of Robotic Volumetric PIV

F. M. A. Mitrotta

TU Delft

Experimental Fluid-Structure Interaction of a Flexible Plate Under Gust Excitation

A Wind-tunnel Investigation by Means of Robotic Volumetric PIV

by

Francesco Mario Antonio Mitrotta

to obtain the degree of Master of Science
at the Delft University of Technology,
to be defended publicly on Friday April 3rd, 2020 at 01:30 PM.

Student number: 4522249
Project duration: November 1st, 2018 – April 3rd, 2020
Thesis committee:

Dr. ir. B. W. van Oudheusden,	TU Delft, chair of assessment committee
Dr. A. Sciacchitano,	TU Delft, supervisor
Dr. D. Ragni,	TU Delft, committee member
Dr. J. Sodja,	TU Delft, committee member

An electronic version of this thesis is available at `http://repository.tudelft.nl/`.

TU Delft

Preface

It has taken me a while to get to the end of my journey here at TU Delft. Now, while I am writing this preface, only few days are missing to my graduation and it does not seem almost true. When I look back at my path, since when I started in 2015, I have conflicting thoughts. On one hand I am happy of all my experiences and of all the things that I could learn through those. On the other hand I wonder if I could made different choices that could bring me earlier to the finish line of my master programme and consequently to new challenges. In fact, there is one very important learning from these years that I believe to be useful for an ambitious person like me and that I will always try to keep in mind. We should not only look at the amount of things we want to learn but also at the time we need to spend on those. We need to look at the ratio between the two elements and we should try to keep that high. In this way, we will be able to learn a good number of interesting and rewarding things and at the same time not to get stuck in commitments that result longer than what we would like. This is because the world is constantly evolving and it is full of things that we do not know and that may change our perspective. For this reason, we change as well as people and our ambition, motivation and desires are not fixed in time. Making a smart use of time allows us to ride these changes and to be free to seize the opportunities we want. I understand that this may not be the same for everyone, but at least this is what I have realized for myself.

Indeed, my journey at TU Delft has been full of changes and of personal development. I recognize that I am not the same person of when I started my master programme. In general, I feel more aware of myself and of the world around me. I consider myself privileged in having had the opportunity to face such path and to grow as a human thanks to it. And I believe this thought does not apply only to my journey at TU Delft, but probably to my entire life so far. I was lucky to be born in a developed country that allowed me to live a comfortable childhood. I was lucky to be born in a family that allowed me to study away from my hometown, first in Turin and then in Delft, never lacking the moral and economic support. Of course I do not think that it was only a matter of luck, as I believe that I have worked hard to deserve every goal I have achieved. But it would be unfair not to recognize how the boundary conditions of my life were quite favourable. And the main part of these favourable boundary conditions is constituted by the people who raised me and by the ones with whom I had the possibility to share my experiences during these years. We should never forget that many times other people is what can make ourselves better. This is definitely the case for me and the least that I can try to do is to acknowledge their contribution to my personal growth.

At first I would like to thank my thesis supervisor, *Dr. Andrea Sciacchitano*. I feel that my thesis project has been a long journey inside a longer journey and I am thankful to have had Andrea guiding me through it. He has been very available since the first moment I spoke with him about what I wanted to do for my thesis. I will always remember his help in the wind-tunnel in the most critical moments of my experimental campaign. Besides this, I really appreciate his constant indication of the final goal, which was needed when my curiosity towards doing more things was turning into dispersion. Finally, I am also thankful for the opportunity he gave me to write a paper about my work for the *13th International Symposium of on Particle Image Velocimetry*.

I would also like to thank the other co-authors of the mentioned paper, *Dr. Jurij Sodja*, *Dr.ir. Roeland de Breuker* and *Dr.ir. Bas van Oudheusden*. I am very thankful to Jurij for his technical and moral support during my wind-tunnel campaign and the time I spent working on another project in the aeroelasticity group. His passion, dedication and availability will stay as an example for me. My gratitude goes as well to Roeland for making me discover the subject of aeroelasticity, for believing in my abilities and for allowing me to work in a very interesting project within his group. Finally, I wish to thank Bas for considering me for one of the PhD positions of the *Homer* project and for his patience in answering my questions related to the uncertainty of my graduation due to the virus matter in this last period.

Within the Aerospace Faculty there are many other people to whom I would like to express my gratitude. The first is *Darwin*, who supervised my work in the aeroelasticity group. He was always super available with me and made me learn a lot, so I am really thankful to him. I also greatly appreciate the availability of *Paul*, who did not miss a chance to answer my questions, both technical and not. For sure I also cannot forget the time spent with *Carlo* working in the same room. Our relaxing moments with the videos of Germano Mosconi will stay in my hearth. I would also like to thank the guys from the Aerodynamics department who were always up for jokes, interesting chats or for techical suggestions; in particular *Constantin*, *Gabriel* and

Varun. Finally, I am grateful to the people of the staff that helped me in different ways during my thesis project: *Colette*, *Dennis*, *Frits*, *Henk-Jan*, *Nando*, *Nico* and *Peter*.

I cannot miss a special thought for all the people I have met in the legendary *Basement*, where I have spent most of my time since I started my thesis. I feel that we are lucky to have a relatively large community with whom we can share the experience of the thesis. In particular I am grateful for having met *Blanca*, who introduced me to the world of Robotic Volumetric PIV, *Francesco*, whose help was fundamental for my experiment and *Manfredi*, with whom I shared the last months very pleasantly as neighbours.

Not less than a huge quantity of love can go to the people of *A.S. Troonz*, my amazing football team of the Monday League. It has been an honour to guide you from the defence and to shout all the time during the game. I hope you will keep hearing my voice in your heads for a long time to come. Thanks a lot for all the fun we had in these years, the monday evening game with you is going to be one of the things I will miss the most once I leave Delft. I wish you good luck for everything: *Aron*, *Ale Parisi*, *Andrea*, *Anton*, *Davide*, *Kushal*, *Miguel*, *Niklas*, *Pietro*, *Sebas*, *Seba*.

Non posso non dedicare un pensiero ai miei coinquilini di questi ultimi anni, con cui ho condiviso un tetto e molto piú. Innanzituto a *Vittorio*, disponibile nei momenti del bisogno e partner di mille discorsi, dai piú ai meno impegnati. Un ringraziamento particolare va ovviamente a *Damieno Terrapieno* (l'altro nome é probabilmente troppo politicamente scorretto per i ringraziamenti di una tesi), vittima delle mie canzoncine, delle mie foto durante le sue sedute di yoga e piú in generale delle mie molestie. Hugo de Grootstraat 49A non sarebbe la stessa cosa senza di te. Infine un grande grazie va anche a *Marco* che é diventato in poco tempo un mio compagno in tutto: Monday League, Age of Empires, pranzi, cene, paste al forno, body power, synergy 360 ed infine il leggendario XCORE. In questi ultimi mesi ho trovato un amico sincero e te ne sono grato.

Un ringraziamento ed una dedica speciale va alla comunitá italiana con cui ho condiviso la mia esperienza in Olanda, quella che si identifica con i gruppi WhatsApp de *LaRibellione* e per chi ha piú tempo da perdere con *Non É L'Arena*. Siete stati una fonte immensa di confronto e di svago allo stesso tempo, parte della mia crescita personale in questi anni la devo soprattutto a voi: *Nanna*, *FantAntonio*, *Baudo*, *Corrado*, *Davide*, *Federica*, *Fede Cat*, *Trovarello*, *Pippone*, *Mr. Fazzi*, *Francesco*, *Beppone* (mannaggia a te ed alla Protezione Civile che ci ha fatto perdere il torneo), *Greta*, *Ilario*, *Hans*, *Defra*, *Lucrezia*, *Gigi*, *Teone* (non posso fare la rima), *Tommy*, *Umbe*. In particolare vorrei ringraziare *Simo Olto* (NdM) ed il *Prof. D'Aguanno* per la loro vicinanza e le loro attenzioni durante questi ultimi mesi. Un pensiero speciale va anche ad i *Massagondi*, ovvero *Cami* (maestra di quinoa) e *Simo* (maestro di cooling) per essersi presi cura di me da bravi vicini con mille pranzi e duemila cene. Infine un grosso grazie va ad *Edo*, con cui ho condiviso di tutto. Sei stato un compagno di vita eccezionale in questi anni, sempre pronto ad aiutarmi, grande fonte di discussioni costruttive e cene a base di hamburger, presidente allenatore e capitano alla Monday League, ad Age of Empires ed ai body power una volta al mese. Grazie di tutto.

Un pensiero ed un ringraziamento va anche agli amici della *Sezione Crocetta* del *Collegio Einaudi* che ho lasciato a Torino trasferendomi a Delft. Siete stati una famiglia per me durante i miei anni a Torino e ad ogni nostro ritrovo é come se il tempo non fosse mai passato. Vi sono grato di questo, in particolare a *Carletto*, *Jimi Jimi*, *Luciana*, *Marco*, *Michi Michi*, *Sexy Coco*, *Vane*.

Non posso inoltre dimenticare i miei amici di Brindisi, che non mi hanno fatto mai mancare il loro affetto non solo durante i ritorni nella mia terra, ma anche a distanza. Grazie tante *Andrea*, *Elio*, *Franco Bamba*, *Fra Valzano*, *Gigi*, *Melaccone*, *Penny*, *Sarda*, *Valentina*.

Un grosso ringraziamento va a tutte quelle persone che sono state e sono vicine a me ed alla mia famiglia. In particolare i miei cugini *Paolo*, *Daniela* e *Gabriella* con le loro famiglie, zio *Franco* e zia *Annamaria*, zio *Umberto* e zia *Isabella*, zia *Giulia* e zio *Fabrizio*, *Luana*, *Antonio* e *Maria*, i fratelli *Monopoli* con le loro famiglie.

Un pensiero in particolare va a mio fratello *Antonio*, che a suo modo non mi ha fatto mancare il supporto da fratello maggiore.

Ovviamente un ringraziamento piú che speciale non puó che andare ai miei fratelli *Giovanni* e *Davide*. Al di lá degli scontri e confronti, sapere che ci sono delle persone su cui puoi sempre contare é una cosa impagabile. Non dimenticheró mai l'armadio montato nella mia prima casa a Delft quando tutto quello che avrei voluto fare era tornare indietro. Grazie, vogliamoci sempre bene. Per mia madre invece non ho parole che possano spiegare la gratitudine verso tutto quello che ha fatto per me in questi anni. Mi ha sempre aiutato in tutto e non mi ha mai fatto mancare il suo supporto in nessuna maniera. Persino in un periodo di pandemia globale il suo pensiero é stato se avessi voluto l'amaro con il pacco da spedire a Delft. Grazie di cuore. Un pensiero non puó non andare anche a mio padre, a cui devo tantissimo di quello che sono ed i cui insegnamenti porto sempre dentro di me.

Infine vorrei ringranziare *Roberta*, che non ha mai smesso di starmi vicina da 7 anni a questa parte, spe-

cialmente da quando sono venuto qui in Olanda. Le tue attenzioni ed il tuo amore sono stati una costante fonte di forza per arrivare fino in fondo a questo percorso.

Francesco Mario Antonio Mitrotta
Delft, March 2020

Abstract

The reduction of atmospheric pollutants emission is one of the biggest challenges of modern aeronautical industry. This is testified by the commitment of international institutions such as the European Commission, with its *Flightpath 2050* document issued in 2011, and by research organization such as NASA, with its *Fixed Wing* project. This attention towards the reduction of fuel burn and consequently of emissions constitutes a drive towards the employment of lightweight aerospace structures, leading in this way to the rise of a variety of so-called aeroelastic problems. Despite the many progresses made in the development of numerical tools for the prediction of aeroelastic phenomena, some aspects still constitute a challenge in the computational field and as a consequence wind-tunnel testing remains an important tool for the study of aeroelastic problems.

Modern aeroelastic models employed in wind-tunnel tests are usually heavily instrumented in their inside in order to host common measurement devices such as pressure sensors, accelerometers and strain gauges. These devices provide accurate experimental data for the characterization of both flow and structure, however they are not ideal both in terms of structural intrusiveness and in terms of the complexity of the model's instrumentation phase. At this purpose, optical metrology offers a valid alternative for both flow and structural measurements. In particular, quantitative flow visualization techniques such as Particle Image Velocimetry (PIV) allow for a thorough characterization of flow fields which for certain aspects results superior to more traditional point-wise measurements. A literature survey on the combination of PIV with optical structural measurements for Fluid-Structure Interaction (FSI) experiments reveals how volumetric flow measurements are almost never carried out. Since a large variety of aeroelastic phenomena involves the presence of 3D unsteady flows and large scale structures, a gap in the simultaneous assessment of volumetric flow fields and of structural displacements emerges from the literature review. Besides this, it is observed how at least two systems are always used to obtain quantitative measurements of both flow and structure, leading to complex setups with challenges related to both the synchronization and the optical isolation of the two systems.

In the field of large-scale aerodynamic testing, the introduction of Helium Filled Soap Bubbles (HFSB) as flow tracers for PIV measurements and the development of efficient particle tracking algorithms such as Shake-the-Box (STB) have enabled a substantial extension of the achievable measurement domain at an affordable computational cost. The development of Robotic Volumetric PIV has allowed to exploit even further the potential of HFSB and STB, revealing a capability of volumetric measurements in domains of several cubic meters. Furthermore, being based on particle tracking, Robotic Volumetric PIV appears as a good candidate for the tracking of markers on a structure and thus for the realization of aeroelastic measurements where a 3D flow and a large structure are characterized with a single measurement system.

The aim of this work is then to assess the feasibility of Robotic Volumetric PIV for aeroelastic investigations. This is achieved studying the dynamic response of a flexible aluminium plate subjected to gust excitation. The experiment is carried out in the Open Jet Facility at Delft University of Technology, which is equipped with a gust generator. Phase-averaged structural displacement of the entire plate together with the volumetric near flow field is measured, with a total measurement volume of approximately 150 litres. Small circular markers are applied to the surface of the plate in order to carry out the structural measurement, which is validated by means of a Scanning Vibrometer. The assessment of the FSI phenomenon is conducted at a wind-tunnel speed of 12 m/s and at a reduced frequency of 0.045. In this way, the capability of Robotic Volumetric PIV to deliver unprecedented quantitative volumetric flow visualization coupled to the measurement of structural displacement over large scales is demonstrated. The challenges faced to achieve such objective include the possibility to distinguish between flow particles and structural markers in the acquired images, the validity of the instantaneous structural displacements measured by the PIV system, the feasibility of the phase-average approach and the consistency of the combined structural and flow information. A visualization of the FSI phenomenon is finally presented, together with a quantitative analysis of its dynamics.

Contents

List of Tables

List of Figures

1 Introduction

On August 28th 2019 the 16-year-old Swedish climate activist Greta Thunberg arrived in New York to participate at the United Nations Climate Action Summit of the following month[1]. As expectable, many activists were present to welcome her, however they did not have to go to any of the Big Apple's airports. They instead gathered in Lower Manhattan as Greta did not fly from Europe to New York, rather she decided to embark a 15-days sail across the Atlantic on the *Malizia II*, an emission-free racing yacht. Indeed the young climate activist is known to avoid flying because of aircrafts' emissions and this initiative is shared by other activists and non-activists around the world. In Sweden, a new expression has even emerged to indicate people's attitude to stop flying in order to lower carbon emission. *Flygskam*, literally translated as "flight shame", is not merely a buzzword, but it actually reflects the change in Swedish travel habits as indicated by some figures showing a decrease in the number of passengers across Swedish airports[2]. If on one hand the idea of giving up flying is at least debatable in today's globalised society, on the other hand this kind of initiatives show how people's concern on environmental issues are real and how transport aircraft industry is not exempted from the matter.

The reduction of atmospheric pollutants emission is indeed one of the biggest challenges of modern aeronautical industry. Besides the actions and initiatives undertaken by part of the civil society, also international institutions and research organizations are playing a role in this challenge. In 2011, the European Commission issued the *Flightpath 2050* document [European Commission, 2011], where a vision for the European aviation community in 2050 is outlined. Environmental goals include a 75% reduction in CO2 emissions per passenger kilometre and a 90% reduction of NOx with respect to the capabilities of a typical new aircraft in 2000. Another example of commitment to a greener future for aviation is given by NASA's *Fixed Wing* project [Del Rosario et al., 2014], which by 2025 aims at developing technologies that should enable 80% reduction in cruise NOx emissions and 60% reduction in fuel consumption with respect to a best-in-class aircraft of 2005.

A common strategy that pursues reduction of fuel burn and consequently of emissions is the employment of lightweight structures, which have become extensively applied in aircraft design thanks to the use of composite materials. However, the lightweight design approach can result in very flexible structures, especially for slender objects like aircraft wings. An example of this is given by the Boeing 787, first commercial aircraft employing composite materials for the majority of primary structures, including the fuselage, with the relative large displacement that its wing exhibits at take-off (see Figure 1.1). The interaction of such enhanced structural flexibility with the air flow entails a set of complex physical phenomena that makes the design of an aircraft more challenging.

In general, Fluid-Structure Interaction (FSI) problems arise when a flowing fluid interacts with a submerged or bounding flexible structure. More in particular, aeroelasticity is the discipline within the aerospace field that studies the interaction of the air flow with a flexible structure. A well-known classification of aeroelastic problems is given by Collar's triangle of forces [Collar, 1946]. In this representation, aerodynamic, elastic and inertial forces are placed at the vertices of a triangle, as it can be observed in Figure 1.2. The interaction between two or among all three vertices is then used to identify the possible aeroelastic problems. These include control reversal, divergence, flutter, buffeting and gust loads, just to mention the most renowned ones.

[1] `https://www.nytimes.com/2019/08/28/nyregion/greta-thunberg-new-york.html`, accessed: 13-11-2019.
[2] `https://www.bbc.co.uk/newsround/49032117`, accessed: 13-11-2019.

Figure 1.1: Boeing 787 at take-off showing the large flexibility of its wing. Reproduced from `https://aviation.stackexchange.com/questions/14719/is-wing-flex-good` (accessed: 13-11-2019).

As a matter of fact, with lighter (less inertia) and more flexible structures, the interaction among the vertices of the triangle is stronger and aeroelastic problems become more relevant.

Thanks to the constant increase in available computational power, aeroelastic problems have been tackled by means of numerical tools leading to the successful establishment of some methodologies that today are considered to be mature [Schuster et al., 2003]. These methodologies include linear analysis for flutter, aeroservoelasticity and gust response. However, there are still a number of problems for which computational tools have been shown to work only for limited cases or have fallen short of meeting analysis requirement [Schuster et al., 2003]. One main aspect of simulations that is not yet considered mature enough is the application of high-order viscous unsteady aerodynamics models. In addition to this, computations of transonic dip of flutter velocity for entire vehicle configuration, nonlinear aeroservoelastic analyses and Limit-Cycle Oscillation (LCO) assessments are not at a reliable level for routine use. Furthermore, the computational cost of nonlinear unsteady aerodynamic analysis together with a robust moving grid methodology hampers the possibility of an extensive use of simulations. In fact, when dealing with complex aircraft configurations such as fighter jets, there is a long list of geometric details that can have a dramatic impact on the aeroelastic performance of the air vehicle and their thorough assessment may result impractical. For these reasons, aeroelastic wind-tunnel and flight tests are and will be needed to investigate possible problems that cannot be identified by means of computational tools, especially if structures with higher degrees of flexibility are envisioned in the future [Schuster et al., 2003].

Aeroelastic wind-tunnel tests are reported to have been conducted since the time of Theodorsen's development of flutter theory [Ricketts, 1990]. Purposes of aeroalstic experiments include verification of analitycal methods, understading of the physics underlying aeroelastic phenomena, assessment before flight tests and validation of computational tools. Since the interaction between flow and structure is studied in aeroelastic experiments, static and dynamic measurements of both flow and structure are of interest. A general requirement for the instrumentation used to perform such measurements is the non-intrusiveness. This is done in order to minimize the alteration of wind-tunnel model mass and of the flow field around it. In 1990, strain gages, potentiometers, accelerometers and gyros were reported to be used for structural measurement, whereas pressure transducers were the main tool for steady and unsteady aerodynamic measurements [Ricketts, 1990]. The awareness of the need of a proper flow characterization for the understanding of aeroelastic phenomena was already present at that time. However, mature techniques for quantitative measurements were limited to laser velocimetry methods, which did not allow flow visualization. For the latter only qualitative tools were available, such as schlieren and shadowgraphy. Yet, these two techniques cannot be employed for incompressible flow regimes, where many aeroelastic wind tunnel tests were and are currently conducted. At this purpose, an advancement in terms of quantitative flow visualization was indicated to lay in the devel-

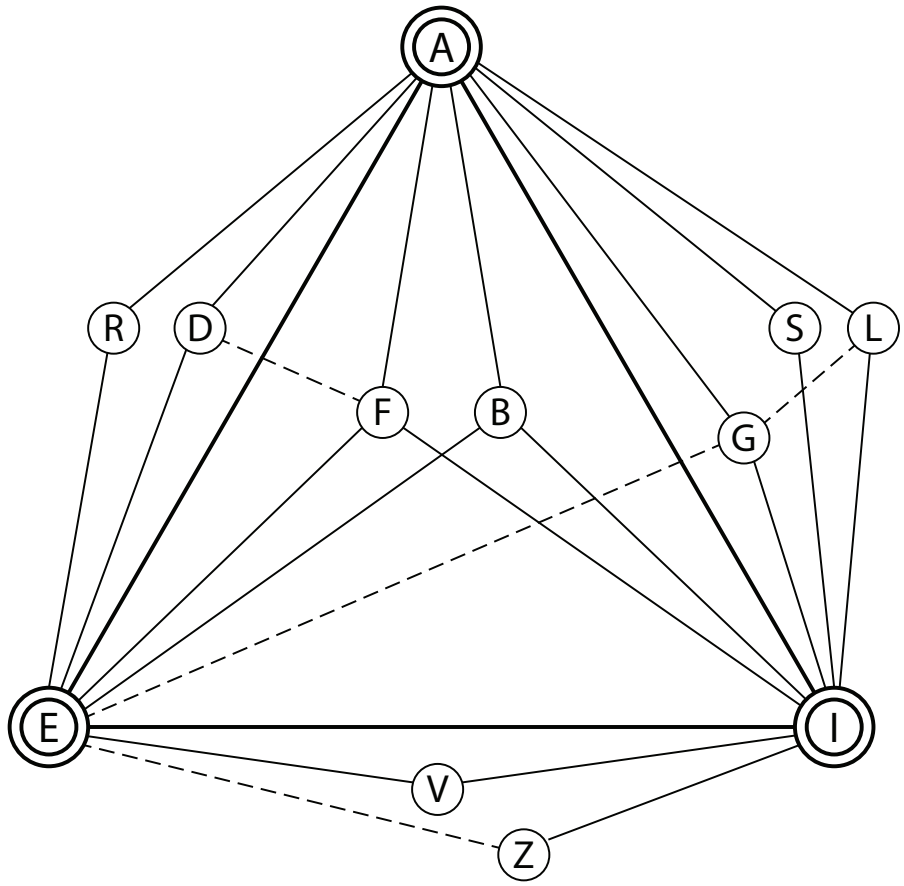

Figure 1.2: Collar's triangle of forces. Adapted from Collar [1946].

opment of so called "global velocimetry methods", which corresponded to a primitive form of the technique known today as Particle Image Velocimetry (PIV)[Ricketts, 1990].

In the last decades, PIV has emerged as the main technique for quantitative flow visualization in a wind-tunnel environment [Raffel et al., 2018]. At the same time, many aeroelastic experiments involving large-scale models have been carried out, see e.g. the work of Ballmann et al. [2008], Mai et al. [2011], Silva et al. [2012]. Structural measurements are still performed by means of strain gauges and accelerometers, needing complex instrumentation of wind-tunnel models. However, also optical measurements of deformation are being used nowadays, enabling non-intrusive evaluation of structural displacements. As far as aerodynamic measurements are concerned, the use of quantitative flow visualization is very limited if not completely absent, with force balances and pressure sensors remaining the main tool for aerodynamic assessment. More in general, the use of PIV for volumetric flow measurements is considered to be hampered by limitations in achievable measurement volume and by system complexity together with cost of data processing [Jux et al., 2018].

A large variety of aeroelastic phenomena involves the presence of 3D unsteady flows and large scale structures, making the experimental assessment of the components of Collar's triangle dependent on the availability of volumetric flow measurement in unsteady flows over large volumes. The recent introduction of Robotic Volumetric PIV by Jux et al. [2018] has opened new possibilities in terms of quantitative flow visual-

ization over large scales. Furthermore, if the aerodynamic data could be coherently combined with full-field measurements of structural deformation, the understanding of aeroelastic phenomena in a wind-tunnel environment would increase, together with the thoroughness of validation of computational tools. This consideration brings to the research objective of the present master's thesis:

"Assess the feasibility of Robotic Volumetric PIV for large-scale experimental aeroelastic investigations, where both an unsteady flow field and dynamic structural displacements are simultaneously measured."

In order to achieve such objective, a wind-tunnel experiment involving a representative configuration of a dynamic aeroelastic system is designed and executed. The investigated case consists in a flexible aluminium plate excited by a periodic gust. The structural displacements measured by the Robotic Volumetric PIV system are validated with simultaneous measurements performed with a Scanning Vibrometer (SV). The phase-averaged structural displacements and flow field are combined together in order to present a full visualization of the FSI phenomenon.

A brief summary of the organization of the present master thesis is given to conclude this introduction. The few examples available in literature regarding optical metrology applied to combined aerodynamic and structural measurements are discussed in Chapter 2. Following that, the Robotic Volumetric PIV technique is described in all its components in Chapter 3, which is concluded with the formulation of the research questions. Chapter 4 deals with the experimental setup and procedures employed for the achievement of the research objective. The applied data reduction techniques are described in Chapter 5, followed by a discussion of the obtained results in Chapter 6. Finally Chapter 7 summarizes the achievements of this thesis and provides some recommendations for future studies.

2

Optical Metrology Applied to FSI

An ideal aeroelastic wind-tunnel test requires non-intrusive measurement systems for both flow and structure, such that an intangible alteration of flow field and structural dynamics is achieved. However, modern aeroelastic models are usually heavily instrumented in their inside in order to host common measurement devices such as pressure sensors, accelerometers and strain gauges (see Figure 2.1). Even if this practice provides accurate experimental data, it is not ideal both in terms of structural intrusiveness and in terms of the complexity of the model's instrumentation phase. At this purpose optical metrology offers a valid alternative for both flow and structural measurements.

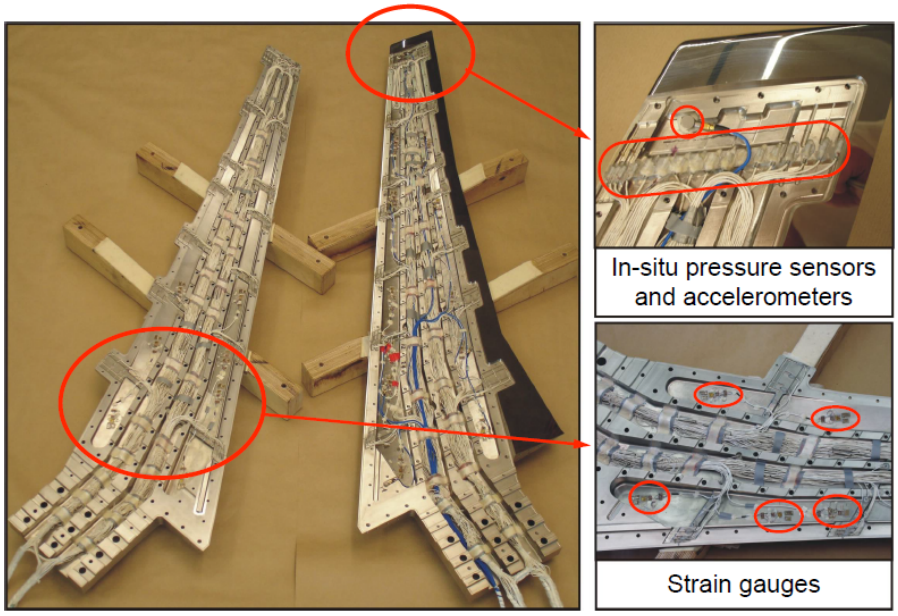

Figure 2.1: Example of an instrumented aeroelastic wing model. Reproduced from Ballmann et al. [2008].

In general, optical metrology is the science of measuring making use of light and of its properties. In the context of wind-tunnel testing a variety of different techniques shares the use of a camera to acquire images and subsequently process those in order to obtain a measurement of the quantity of interest. These techniques offer the advantage of being relatively non-intrusive with respect to more traditional measurement devices and in some cases they allow full-field rather than point-wise measurements.

For this reason, a survey on the application of optical techniques to FSI investigations in a wind-tunnel environment is presented in this chapter. As far as flow measurement is concerned, the focus is given to PIV, which is considered an established technique for quantitative flow visualization. Therefore, the discussion deals with the combination of PIV with optical techniques used for structural assessment. At first, the coupling of PIV with Digital Image Correlation (DIC) is examined, being it the most popular combination found

in the literature. Later, the application of PIV together with alternative methods for structural measurements is discussed.

Contents

2.1. Coupled PIV and DIC

The majority of experimental FSI investigations involving optical techniques for measurement of both flow and structure were performed coupling PIV and DIC [Bleischwitz et al., 2017, Marimon Giovannetti et al., 2017, Timpe et al., 2013, Zhang et al., 2019]. A schematic illustration of the two techniques is given in Figure 2.2 and a brief discussion of their principles is provided. For a detailed description of the specific working principles the reader is referred to the literature, see e.g. Raffel et al. [2018] and Pan et al. [2009].

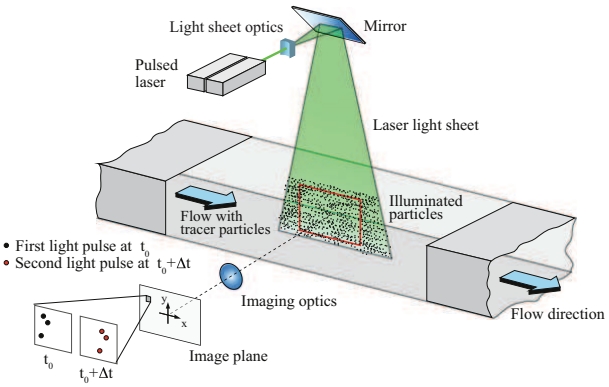

(a) Generic experimental arrangement for planar 2C-2D PIV. Reproduced from Raffel et al. [2018].

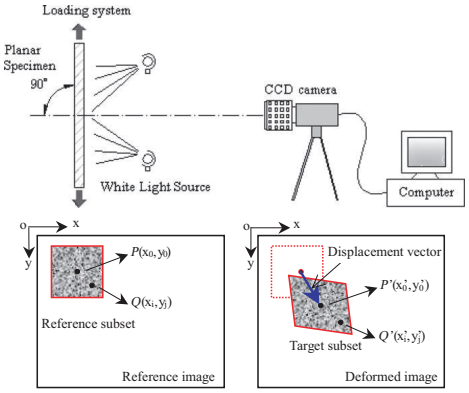

(b) Generic experimental arrangement for 2D DIC. Adapted from Pan et al. [2009].

Figure 2.2: Illustration of the PIV and DIC techniques.

Figure 2.2a shows a generic experimental arrangement used for planar PIV. In such kind of experiment, the fluid is seeded with micron-sized particles that are used as flow tracers. A pulsed laser generates a light beam which is conveyed through some lenses and mirrors in such a way to form a thin light sheet illuminating the region of interest of the flow. This arrangement allows the particles in the flow to be illuminated twice with a short time delay between the two laser pulses so that their scattered light can be recorded by a digital camera. The acquired images are divided in small interrogation areas and the average displacement of the particles in each area between the first and the second image is evaluated by means of statistical methods. The result is a displacement field of the particles over the imaged region, the so-called field of view (FOV), which can be transformed in a velocity field knowing the laser pulse separation time. In this way the two components of the velocity field over the illuminated plane are calculated. This basic PIV arrangement is in fact called two-components (2C) two-dimensional (2D) PIV. The addition of a second camera imaging with a different viewing direction allows to recover the out-of-plane component of the velocity, leading to the measurement of the three-dimensional velocity field over the illuminated plane. This advanced PIV arrangement is known as 3C-2D PIV or stereoscopic PIV.

The measurement of solid structures response to applied loads by means of DIC exploits similar principles with respect to PIV. A generic experimental arrangement for 2D DIC is composed by a specimen, white light source, a digital camera and a processing computer, as shown in Figure 2.2b. The surface of the tested specimen presents a natural or an artificial speckle pattern, providing in this way a random gray intensity distribution for the imaging camera. The specimen is then illuminated with white light in order to make the speckle pattern clearly visible by the camera, which records images of the unloaded and loaded structure. Analogously to PIV, the images are divided into small interrogation areas and statistical methods are applied to find the in-plane displacement field of the loaded structure with respect to the unloaded configuration. The strain field of the surface can then be assessed by differentiation of the displacement field. In a similar way as mentioned for PIV, the addition of another camera to the measurement setup allows for the assessment of out-of-plane displacements and strains of the structure, leading to a full three-dimensional measurement of the structural deformation.

A first application of coupled PIV and DIC can be found in the work of Timpe et al. [2013], where the FSI related to a Micro-Air-Vehicle (MAV) wing was investigated. More specifically the authors employed a synchronized, time-resolved PIV and DIC to study the passive flow control mechanism of a free trailing-edge scalloped membrane wing. They were able to obtain three-dimensional membrane displacement of the central part of the wing by means of two high-speed DIC cameras and two-dimensional flow field in the symmetry plane of the wing by means of two high-speed PIV cameras in a side-by-side configuration capturing fields

of view of 8.9 cm × 4.2 cm (width × height) and 11.9 cm × 5.6 cm. An illustration of the used wing model is presented in Figure 2.3, together with a representative result obtained from the experiments. The combined use of PIV and DIC proved to be decisive as the authors were able to assess the correlation between fluctuating membrane displacement and fluctuating velocity components showing how the wake velocity field was first forced by the membrane motion at low angles of attack, while for high angles of attack it was mainly dominated by the bluff body shedding from the rigid leading edge. Despite this remarkable result, the measurement regions of both DIC and PIV were relatively small and did not allow a full three-dimensional FSI investigation.

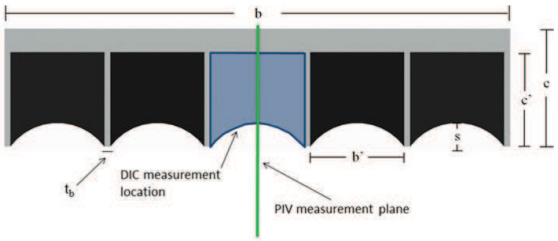

(a) Dimensions of the batten reinforced wing model with location of the PIV and DIC measurements. Rigid parts are indicated in gray, flexible membranes in black, the PIV measurement plane in green and the membrane measured by the DIC in light blue. The DIC measurement region corresponds to $b' \times c' = 61.4$ mm × 61.4 mm.

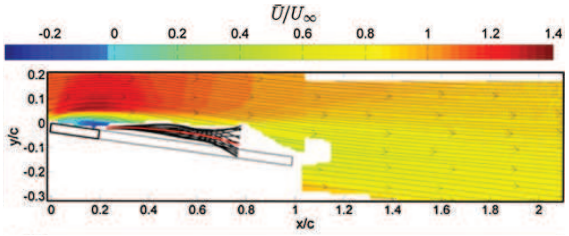

(b) Ratio of time-averaged horizontal component of velocity to free-stream velocity at an angle of attack of 8°. The time-averaged membrane position is indicated with a red lines, while the black lines indicate instantaneous membrane positions.

Figure 2.3: Illustration of the wing model used by Timpe et al. [2013] and representative results. Adapted from Timpe et al. [2013].

Another example of coupled PIV and DIC applied to an experimental investigation of a MAV wing is given by the work of Bleischwitz et al. [2017]. In such study the authors assessed the coupling dynamics between flow and membrane involved in the operation of a flexible membrane wing in and out of ground-effect. Also in this case four synchronized high-speed cameras were used: two for stereoscopic DIC, measuring instantaneous membrane deformations, and two for planar PIV, measuring the instantaneous two-dimensional flow field around the wing and in the wake. Differently from Timpe et al. [2013], Bleischwitz et al. [2017] measured the deformation of the entire wing and set the PIV measurement plane at the quarter-span of the model, halfway between the wing tip and the supporting sting system. Furthermore, the authors mention the use of different light sources for PIV and DIC and consequently the use of different bandpass filters on the respective cameras in order to remove the light content corresponding to the undesired light source. The resulting measured area by the DIC cameras was 100 mm × 200 mm (chord × wingspan) and the FOV obtained by the PIV cameras amounted to 148 mm × 100 mm (streamwise × height). An illustration of the experimental setup is shown in Figure 2.4, together with a representative result obtained from the measurements. Once again the synchronized PIV and DIC measurements proved to be crucial for the investigation of the FSI phenomena, this time revealing the beneficial performance effect of the in-phase coupling between the membrane and the flow under separated flow conditions. Still, the flow measurements were only two-dimensional, preventing a thorough study of the three-dimensional phenomena arising from the interaction between flow and membrane.

Both Timpe et al. [2013] and Bleischwitz et al. [2017] performed synchronized PIV and DIC measurements, revealing two-dimensional velocity field of the flow and three-dimensional displacement field of the structure, however they did not attempt to estimate the aerodynamic load from such measurements. This approach was presented by Zhang et al. [2019], who demonstrated the feasibility of a combined PIV and DIC measurement for full-field flow pressure estimation and structural deformation assessment. The investigation was conducted using a flexible plate clamped at one end inside a water-tunnel. The plate was positioned such that its surface was perpendicular to the incoming flow and thus it could achieve a steady deflection under a steady hydrodynamic load. In this way the authors could perform the PIV and DIC measurements in separate experiments and avoid interference between different light sources. A single camera was used for both PIV and DIC, leading to two-dimensional field of both velocity and displacement with FOVs of 43 mm × 58 mm and 12 cm × 8 cm, respectively. A representation of the experimental setup and some representative results are given in Figure 2.5. Beyond direct measurement of velocity field, reconstruction of pressure field from velocity and direct measurement of structural displacement of the plate, the authors also assessed

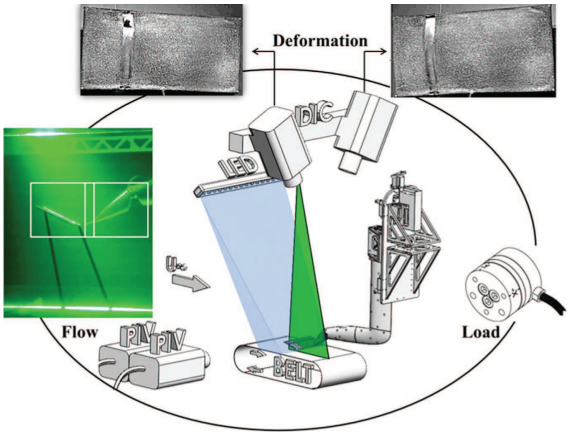

(a) Perimeter reinforced wing model and experimental setup of the time-synchronized PIV, DIC and load measurements. A 10 mm wide translucent latex region is visible in the wing model, which allows the PIV laser to illuminate both above and below the wing. PIV plane is indicated in green, LED illumination for DIC is indicated with blue shading.

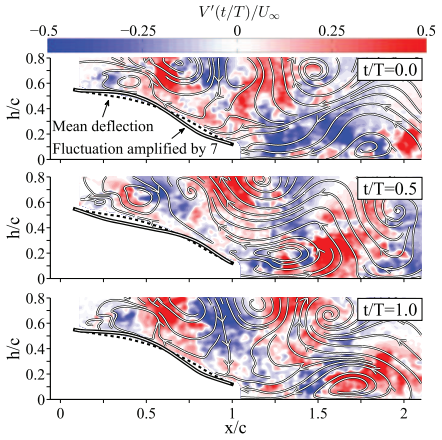

(b) Time-snapshots of vertical flow and membrane fluctuation (latter amplified by a factor of 7) for an extreme ground-effect condition at an angle of attack of 25°.

Figure 2.4: Illustration of the experimental setup used by Bleischwitz et al. [2017] and representative results. Adapted from Bleischwitz et al. [2017].

the feasibility of indirect estimation of loading on plate surface and plate deformation from DIC and PIV, respectively. The work of Zhang et al. [2019] is however limited to a steady two-dimensional configuration.

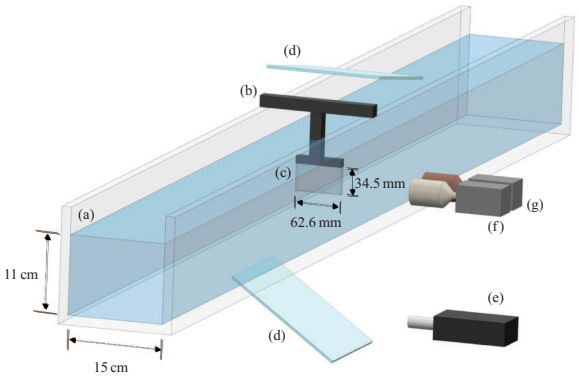

(a) Schematic of the experimental setup for the combined PIV/DIC system, including: (a) water tunnel, (b) support, (c) flexible plate, (d) mirrors, (e) laser, (f) camera for PIV, and (g) camera for DIC.

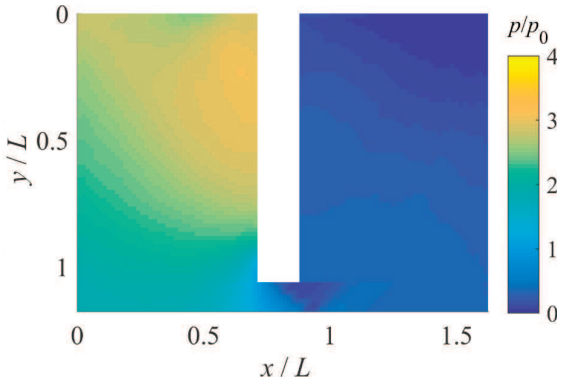

(b) Flow pressure around the plate reconstructed from the velocity field.

Figure 2.5: Illustration of the experimental setup used by Zhang et al. [2019] and representative results. Adapted from Zhang et al. [2019].

The assessment of the three velocity components of the flow combined with measurement of structural displacements can be found in the work of Marimon Giovannetti et al. [2017]. In such investigation the authors used synchronized stereoscopic PIV and three-dimensional DIC to measure the displacement of a flexible rectangular wing and the flow field in a plane of the wing's wake under steady inflow conditions at different wind-tunnel speeds. The measurement setup consisted in two PIV cameras mounted on the wind tunnel ceiling downstream of the tested wing and in two DIC cameras placed in the viewing room of the wind-tunnel. The tip of the wing was provided with a speckle pattern resulting in a total measured area of 450 mm × 450 mm. The PIV plane was set one chord downstream of the wing tip and it was generated to be orthogonal to the free-stream, as it can be observed in Figure 2.6. The resulting FOV was reported to be 400 mm × 120 mm. A special attention was given to ensure optical isolation between PIV and DIC. Low-pass filters were applied to the PIV cameras, so that only the laser light could be captured, and magenta gel filters were applied to

the LED lights providing illumination for the speckle pattern. In this way the green component of the white light was removed and the PIV cameras could detect only the particles in the thin laser sheet. The DIC FOV did not intersect the one of PIV, so no additional filters were necessary for the respective cameras. Beyond assessing the accuracy of the coupled measurement system, the authors discussed the relation between the wing tip displacement and the tip vortex position for different free-stream velocities. Representative results of the tip vortex flow field are reported in Figure 2.7. As mentioned by the authors, it is possible to notice that the increased inertial effects at the largest wind-tunnel velocity tested move the wrap-up location of the tip vortex downstream with respect to the position of the PIV plane. This indicates how a thorough assessment of the flow features in aeroelastic problems relies on the availability of volumetric flow measurements.

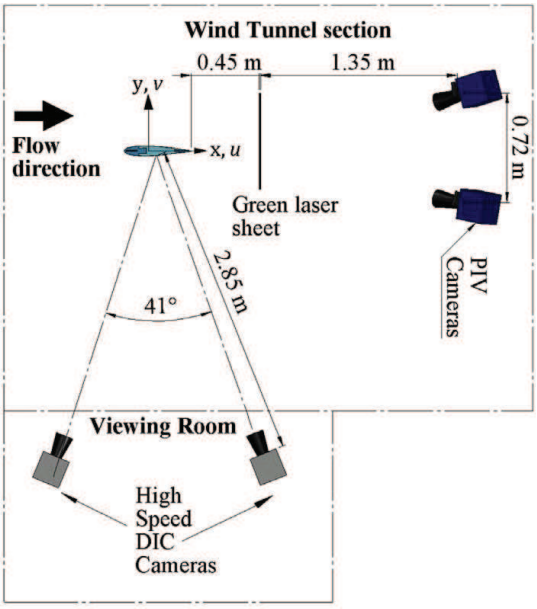

(a) Plan view of the measurement setup in the wind-tunnel.

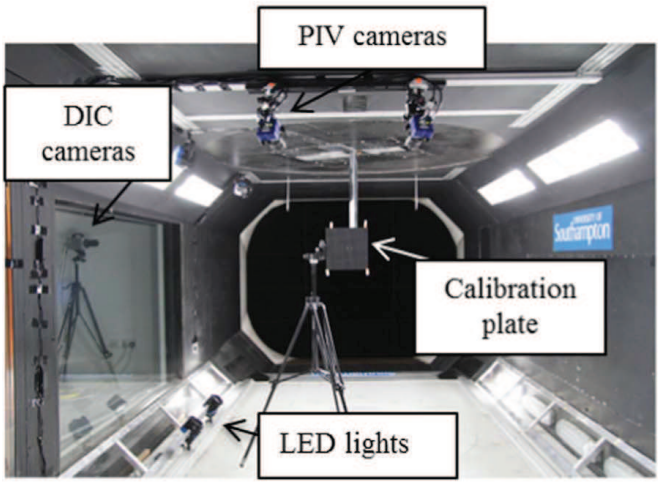

(b) Wind-tunnel test section during PIV calibration.

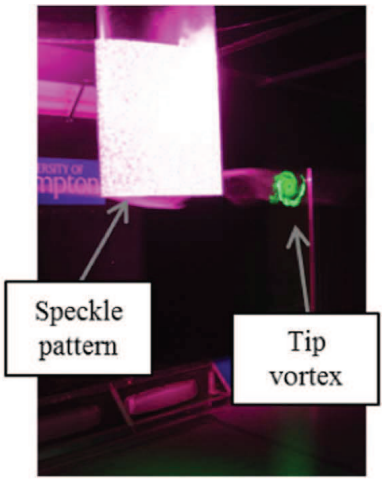

(c) Coupled illumination for PIV and DIC.

Figure 2.6: Illustration of the experimental setup used by Marimon Giovannetti et al. [2017]. Adapted from Marimon Giovannetti et al. [2017].

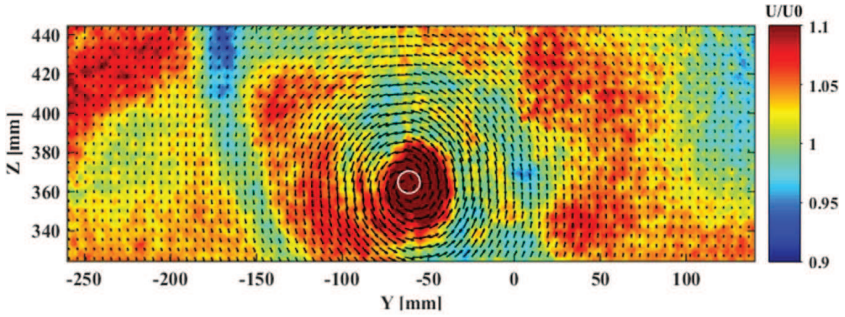

(a) $V_\infty = 10$ m/s.

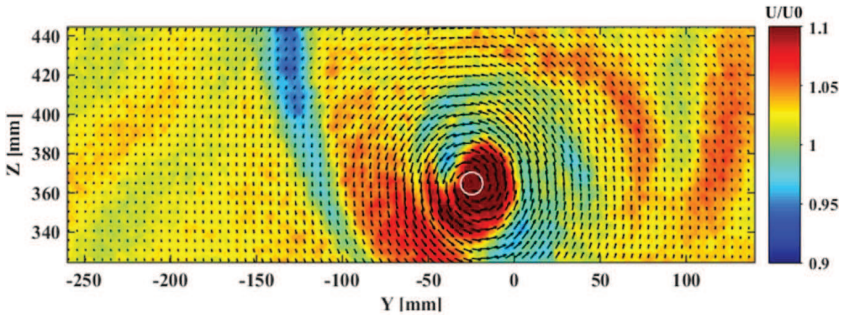

(b) $V_\infty = 20$ m/s.

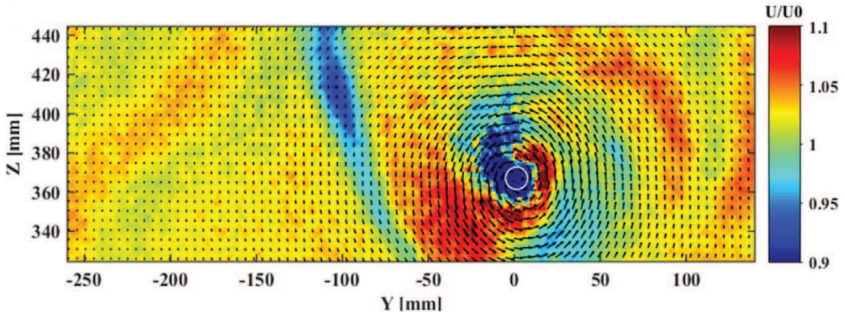

(c) $V_\infty = 25$ m/s.

Figure 2.7: Representative results of the tip vortex flow field studied by Marimon Giovannetti et al. [2017]. Contour represents the time-averaged axial velocity distribution relative to the free-stream velocity. Vector field represents the time-averaged in-plane velocity field. The vortex centre is calculated from the mean velocity field and it is indicated by a white circle. Adapted from Marimon Giovannetti et al. [2017].

2.2. PIV and alternative structural assessment

Only few studies where PIV is combined with some sort of assessment of structural response do not employ DIC. For example Khosla et al. [2009] performed an investigation on voice production, attempting to correlate the acoustic energy in the higher frequency harmonics with intraglottal vorticity [1]. A 2D PIV system was used to assess the phase-averaged flow field in excised canine larynges, while a high-speed video camera was used to visualize the vocal fold vibrations. The latter allowed to distinguish between symmetric or asymmetric vibrations of the vocal fold but did not yield substantial quantitative data. Another example of use of raw images to infer information on structural response is given in the work of Deshpande and Modani [2019]. In such study the FSI of a bird-like flapping wing was investigated and phase-averaged 2C-2D PIV measurements were performed on different planes parallel to the flow and perpendicular to the wing at rest. The dynamic deformation of the flapping wing was assessed through raw PIV images, leading only to qualitative information.

To the best of the author's knowledge, the only study where volumetric quantitative flow visualization is

[1] This experiment was not conducted in a wind-tunnel environment but it is reported here to give an idea about the possible use of optical systems for qualitative structural assessments.

coupled with a quantitative structural assessment is the one of Kalmbach and Breuer [2013], where the authors propose an experimental benchmark for a generic FSI test case. This test case involved a rigid cylinder with a flexible tail, where the vortex shedding induces dynamic deformation of the tail. Planar PIV and volumetric V3V measurements of the phase-averaged flow were separately performed and they were coupled with deformation measurement obtained by means of a multiple-point laser triangulation sensor. The latter allowed to measure the displacements along a laser line reflected on the surface of the tested object, generating in this way a two-dimensional profile of the structural deformation. The FOV of the planar PIV measurement was around 212 mm × 153 mm, while the measured volume by the V3V system amounted to approximately 0.3 m^3. A sketch of the geometrical configuration of the experiment and a representative result is shown in Figure 2.8. Despite the valuable experimental data provided for validation of numerical FSI methods, the volume measured was relatively small and the structural displacements were evaluated only along a line.

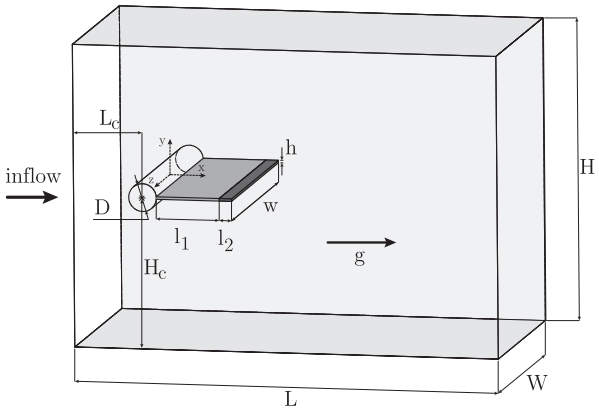

(a) Sketch of the geometrical configuration of the proposed benchmark case.

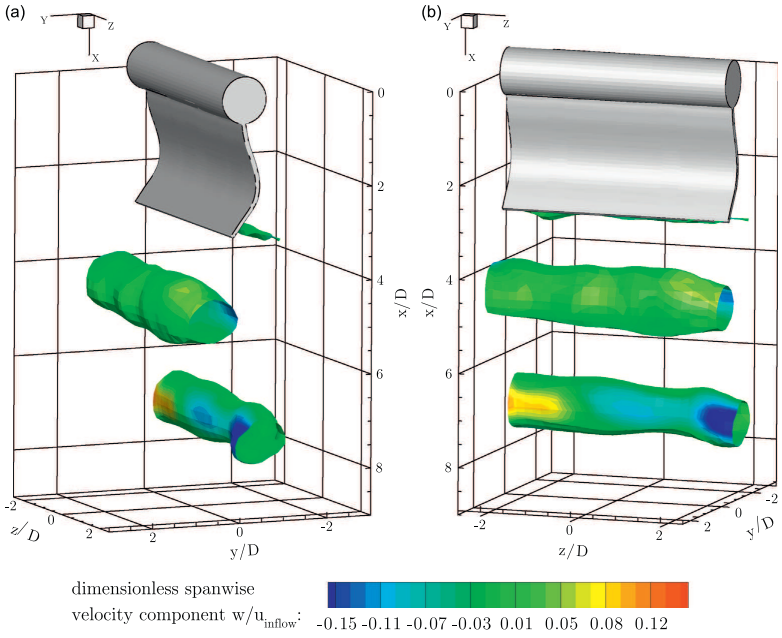

(b) Structure and flow results showing a phase-averaged coupled measurement at $t = \pi$, the iso-surfaces represent the dimensionless velocity magnitude $u = u_{inflow} = 0.79$, the contours on the iso-surfaces depict the spanwise velocity component.

Figure 2.8: Illustration of the geometrical configuration used by Kalmbach and Breuer [2013] and representative results. Adapted from Kalmbach and Breuer [2013].

To conclude this chapter on optical metrology applied to FSI investigations, the reviewed works are summarized in Table 2.1. It can be noticed how volumetric flow measurements are almost never carried out, and when they are the volume is relatively small and the coupled structural measurement is limited to a two-

dimensional profile. Thus a gap in the simultaneous assessment of volumetric flow fields and of structural displacements emerges from this literature review. Besides this, it is observed how at least two systems are always used to obtain quantitative measurements of both flow and structure. This leads to complex setups such as the ones where simultaneous PIV and DIC acquisitions are performed, with challenges related to both the synchronization and the optical isolation of the two systems.

In the last years, the introduction of helium-filled soap bubbles (HFSB) as flow tracers for wind-tunnel experiments [Scarano et al., 2015] has enabled measurement of flow fields in unprecedented large volumes. Besides, the development of advanced Lagrangian particle tracking algorithms [Schanz et al., 2016] presents a great potential for simultaneous flow and structural measurements with only one imaging system. Finally, considering FSI problems that present a periodicity, the recent introduction of Robotic Volumetric PIV [Jux et al., 2018] opens the possibility of filling the gap found in the literature using a single measurement system characterized by operational simplicity and flexibility. In the following chapter, the principles of such technique will be explained and a research objective will be proposed with the aim of achieving simultaneous measurement of volumetric flow fields and structural displacements over a large scale.

Table 2.1: Test matrix for the wind-tunnel experiment.

Reference work	Test object	Aerodynamic measurement		Structural measurement	
		Technique	Measurement domain	Technique	Measurement domain
Timpe et al. [2013]	Batten reinforced membrane wing	2C-2D PIV	148 mm × 100 mm	3D DIC	100 mm × 200 mm
Bleischwitz et al. [2017]	Perimeter reinforced membrane wing	2C-2D PIV	89 mm × 42 mm & 119 mm × 56 mm	3D DIC	61.4 mm × 61.4 mm
Zhang et al. [2019]	Flexible plate	2D-2C PIV	43 mm × 58 mm	2D DIC	120 mm × 80 mm
Marimon Giovannetti et al. [2017]	Flexible wing	3C-2D PIV	400 mm × 120 mm	3D DIC	450 mm × 450 mm
Khosla et al. [2009]	Excised canine larynge	2C-2D PIV	7 mm × 7 mm	High-speed video images	-
Deshpande and Modani [2019]	Bird-like flapping wing	2C-2D PIV	270 mm × 185 mm	Raw PIV images	-
Kalmbach and Breuer [2013]	Rigid cylinder with flexible tail	2C-2D PIV & V3V	212 mm × 153 mm & 0.3 m^3	Multiple-point laser triangulation	72 mm line

3

Robotic Volumetric PIV: Principles and Research Objective

In the field of large-scale aerodynamic testing, the introduction of Helium Filled Soap Bubbles (HFSB) as flow tracers for PIV measurements in a wind-tunnel environment [Scarano et al., 2015] has enabled a substantial extension of the achievable measurement domain with respect to traditional micron-size droplets. The development of Robotic Volumetric PIV [Jux et al., 2018] has allowed to exploit even further the potential of HFSB, revealing a capability of volumetric measurements in domains of several cubic meters. Jux et al. [2018] discussed the principles of Robotic Volumetric PIV and demonstrated its operation by measuring the time-averaged velocity field around a full-scale cyclist mannequin. The final measurement volume was approximately 2 m^3 large, resulting from the acquisition of 450 independent views. Since the technique is based on particle tracking rather than a statistical approach, it may be regarded suitable not only for the tracking of flow particles, but also for measurement of displacements of markers belonging to a moving structure. For this reason, in this chapter the principles of Robotic Volumetric PIV are first introduced and later its possible application to FSI problems is discussed, leading to the research objective of this thesis.

Contents

3.1. Principles of Robotic Volumetric PIV

Robotic Volumetric PIV is based on the use of a Coaxial Volumetric Velocimetry probe [Schneiders et al., 2018], on the employment of HFSB as flow tracers, in order to have detectable particles in large volumes, on processing techniques including an efficient particle tracking algorithm such as Shake-the-Box [Schanz et al., 2016] and a method for the conversion of Lagrangian tracks into an Eulerian flow field, and finally on the robotic manipulation of the measuring probe. These elements constitute the building blocks of the technique and are discussed in detail below.

3.1.1. Coaxial Volumetric Velocimetry

Coaxial Volumetric Velocimetry (CVV) is a recently introduced type of PIV for volumetric flow measurement in wind-tunnels. The technique is based on a measurement system rooted in the more established tomographic PIV [Scarano, 2012], employing a multi-camera (three or more) arrangement where the viewing directions of each couple of cameras subtend an angle called tomographic aperture β. One of the main characteristics of CVV is the solid angle of only few degrees formed by the viewing directions of the different cameras of the measurement system, resulting in a tomographic aperture that is one order of magnitude smaller with respect to usual tomographic PIV setups. Another distinguishable feature of CVV is the coaxial illumination, that is to say an illumination of the measurement volume along the same direction as the one used for imaging (see Figure 3.1).

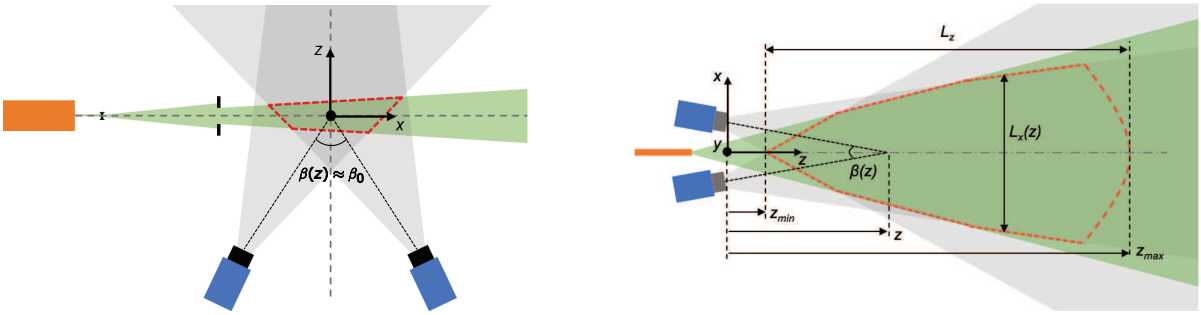

(a) Tomographic PIV, where the tomographic aperture β is almost constant due to the small depth of the illuminated volume.

(b) CVV, where a large variation in tomographic aperture β is present due to the large depth of the illuminated volume.

Figure 3.1: Comparison of the measurement setup for PIV and a coaxial velocimeter, showing the cameras (blue), field of view (grey) and laser illumination (green) provided from a laser device or from an optical fiber (orange). Adapted from Schneiders et al. [2018].

These characteristics permit the integration of both the imaging and the illumination devices in a single module, with an optical fiber transmitting the light coming from the laser head and allowing for its emission from the measurement probe itself. Furthermore, the laser light providing the illumination is expanded in a conical fashion so that the full field of view of the cameras can be potentially covered.

As observable in Figure 3.1, a CVV setup requires optical access along only one direction. The resulting depth of the measurement volume can be relatively large provided that enough laser pulse energy is available and that the cameras have a low noise level. In order to successfully detect particles within the entire measurement volume, a long focal depth is necessary for the cameras and the imaging aperture has to be selected accordingly. Besides the obvious dependency on the size of the active sensor of the cameras, Schneiders et al. [2018] report that the maximum measurement volume is dependent on the ratio between maximum and minimum measurement distance along the imaging direction, which in turn depends on the ratio between camera sensitivity and minimum detectable particle image intensity. A representative measurement volume of the CVV probe is indicated to be about 30 litres, however this can be smaller if the aerodynamic interference of the probe is taken into account [Jux et al., 2018].

An important consequence of the use of a low tomographic aperture is the large instantaneous particle positional error along the imaging direction. Schneiders et al. [2018] report this error to be in the order of 1 mm and in general one order of magnitude larger with respect to the other directions for standard CVV operations. In order to compensate this undesired feature, the employed imaging strategy involves the analysis of the particle's trajectory by means of a multi-framing technique. The velocity is estimated taking into considerations multiple subsequent frames, such that the discrete particle positions, with their anisotropic

uncertainty, can be fitted by a polynomial of second or higher order in time (see Figure 3.2). In this way, the concept of track regularization is realized and the velocity measurement error sees a reduction driven by a scaling factor $k^{-3/2}$ with respect to a double-pulse system, with k being the number of frames evaluated. As a consequence, the compensation of the poor positional accuracy along the imaging direction is achieved by reducing the measurement error of the velocity along the same direction down to a level comparable to the one of a double-pulse system. A typical uncertainty of instantaneous velocities is indicated to be approximately 4% for the component along the imaging direction and 0.2% for the other two components, considering a distance of 37 cm from the measurement probe (corresponding to a tomographic aperture of 0.1 radians), a sequence of 10 frames and a real particle displacement between frames of 5 mm [Schneiders et al., 2018]. However, it should be recalled that the mentioned values of uncertainty are not constant as they increase with the distance from the probe because of the decreasing tomographic aperture.

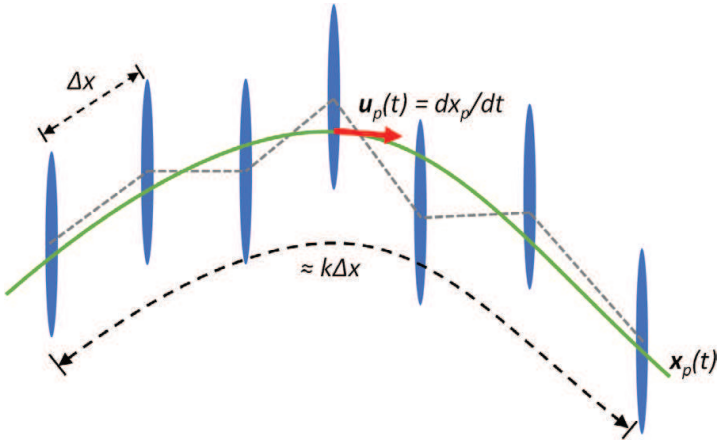

Figure 3.2: Schematic of a particle trajectory evaluated along a discrete number of exposure and with particle elongation due to the low tomographic aperture. The grey dotted lines show the result from two-frame analysis and green line shows a second order polynomial fit over a track length of $k\Delta x$. Reproduced from Schneiders et al. [2018].

The processing algorithms related to the estimation of Lagrangian particles' tracks and to the consequent evaluation of the velocity field are discussed more in detail in Section 3.1.3.

3.1.2. Helium-filled soap bubbles

The deep measurement volume of CVV poses challenging conditions as far as particle imaging is concerned. First of all, a small imaging aperture has to be employed by the lenses installed on the cameras in order to image in-focus all the particles along the deep illuminated volume. Besides this, since the laser light is expanded in a conical fashion from a point source, its intensity is inversely proportional to the square of the distance travelled along the imaging direction. As a consequence, there is a substantial variability of the illumination intensity along the measurement volume.

From these features, it follows that CVV relies on the availability of tracer particles with a high scattering efficiency. These particles are identified with the HFSB, which were first introduced by Bosbach et al. [2009] for PIV measurements in a closed volume and later by Scarano et al. [2015] for PIV measurements in a wind-tunnel environment. The main characteristics of HFSB is that their scattered light has been shown to be $10^4 - 10^5$ times more intense with respect to common PIV micrometer droplets [Caridi, 2018], thanks to their typical diameter ranging from 200 to 400 μm [Bosbach et al., 2009, Scarano et al., 2015].

Despite their scattering efficiency, HFSB could not be proper flow tracers without adequate mechanical properties. In fact, seeding particles used for PIV applications need to have the smallest discrepancy possible between their velocity and the velocity of the seeded fluid in order to introduce a negligible error in the measurement. In a continuously accelerating fluid, an estimate of the so-called velocity lag $\boldsymbol{U_s}$ can be obtained by an analogy with Stokes' drag law [Raffel et al., 2018]:

$$\boldsymbol{U_s} = \boldsymbol{U_p} - \boldsymbol{U} = d_p^2 \frac{(\rho_p - \rho)}{18\mu} \frac{\mathrm{d}\boldsymbol{U}}{\mathrm{d}t}, \tag{3.1}$$

where $\boldsymbol{U_p}$ is the particle velocity, $\boldsymbol{U}$ is the fluid velocity, d_p is the particle diameter, ρ_p is the particle density, ρ is the fluid density and μ is the fluid dynamic viscosity. A measure of the tendency of particles to attain

velocity equilibrium with the fluid is given by the response time τ_p, consisting in the ratio between the slip velocity and the fluid acceleration. Scarano et al. [2015] estimated the response time of HFSB with nominal diameter $d_p = 300$ μm to range from 10 to 40 μs. Thanks to the mentioned properties, HFSB were proven to be suitable for large-scale volumetric PIV experiments in wind-tunnel [Caridi et al., 2016, Scarano et al., 2015, Schneiders et al., 2016] and they have been used for CVV as well.

3.1.3. Particle tracking and Eulerian description

As already mentioned, CVV relies on Lagrangian particle tracking to process the acquired images and to estimate the particles' velocity. More precisely, the algorithm Shake-the-Box (STB) [Schanz et al., 2016] is employed in CVV to obtain the Lagrangian tracks of the particles. The main feature of this algorithm is the use of a prediction for the particle position at every new time-step, with a correction method based on image matching technique (what the authors refer as "shaking"). In comparison to standard tomorgraphic PIV processing algorithms, STB shows much higher computational efficiency and comparable spatial resolution, together with the nearly complete suppression of ghost particles.

As reported by Schanz et al. [2016], once the Lagrangian tracks of the particles have been obtained, the conversion of this information to an Eulerian description of the flow is desirable to allow for a better identification of the flow structures. Schanz et al. [2016] mention two approaches for the interpolation of the instantaneous Lagrangian data to an Eulerian grid. The first approach is constituted by a scheme called *FlowFit* [Gesemann, 2015], where the weighted sum of three-dimensional and evenly spaced quadratic B-splines is used to model each component of the flow field. The goal of the scheme is to evaluate the weights of the sum at arbitrary coordinates according to the data coming from the Lagrangian tracks. Additionally, the solution can be regularized by means of other equations that penalize non-zero curvatures and non-zero divergence (the latter in case of incompressible flows). Another possible approach suggested by Schanz et al. [2016] is the vortex-in-cell method (VIC+) [Schneiders et al., 2015]. The main feature of this method is the use of particle tracks' material derivative together with penalization of velocity divergence for the interpolation of scattered velocity measurement on a grid.

The possibility of obtaining instantaneous flow fields from CVV is hampered by two factors. One is the velocity uncertainty, which is not constant along the depth of the measurement volume and may become relatively large away from the measurement probe, especially considering the component along the imaging direction. The other challenge consists in the spatial resolution that can be obtained from instantaneous data. For example, in the experiment of Jux et al. [2018] the average instantaneous concentration of HFSB can be estimated to be in the order of 0.15 particle/cm^3/s [1]. Such concentration leads to an average inter-particle distance of approximately 1.88 cm in the measured volume [2] and thus to a poor spatial resolution when converting the Lagrangian tracks into an Eulerian description.

For this reason, CVV has mainly been used so far to obtain time-averaged velocity fields. At this purpose, both Schneiders et al. [2018] and Jux et al. [2018] use the technique of ensemble averaging to achieve an Eulerian description of the flow field from the particle tracks resulting from the application of STB. This technique consists in interrogating the measurement volume containing the entire set of Lagrangian tracks with small cubic cells, also referred to as interrogation bins, and in taking the average of all the instantaneous velocity information that falls inside such cells. In this way an Eulerian description of the flow field can be obtained on a structured cartesian grid. Advanced ensemble averaging methods for particle-based measurements are discussed by Agüera et al. [2016], that propose different approaches to avoid a constant mean inside the interrogation bin in order to improve the resolution of turbulent statistics. However, for the sake of simplicity, a standard ensemble averaging algorithm is employed by both Schneiders et al. [2018] and Jux et al. [2018]. In the work of the former, an indication on the amount of discrete particle velocity measurements N_I achievable inside a single bin is given:

$$N_I = l_B^3 \, C \, N_t, \tag{3.2}$$

where l_B is the linear size of the interrogation bin, C is the instantaneous concentration of the tracers and N_t is the number of measurement time-instants.

The discussion of time-averaged velocity estimation with CVV would not be complete without a mention to the related uncertainty, dynamic spatial range (DSR) and dynamic velocity range (DVR) [Adrian, 1997]. Jux et al. [2018] indicate that uncertainty of the time-averaged velocity $\epsilon_{\overline{u}}$ is dependent on the standard deviation of the velocity σ_u, the coverage factor k_c and the number of velocity measurements within the interrogation

[1] This is estimated dividing the average concentration of 1 particle/cm^3 obtained during each recording by the duration of the recording.
[2] The average inter-particle distance is proportional to the cubic root of the inverse of the particle concentration.

volume:

$$\epsilon_{\overline{u}} = \frac{k_c \sigma_u}{\sqrt{N_I}}, \tag{3.3}$$

where such uncertainty includes a component coming from the turbulence intensity of the flow and another component given by the uncertainty of the instantaneous velocity estimation. It should be mentioned that the number of discrete velocity measurements N_I used for the estimation of the uncertainty must refer to uncorrelated velocity measurements. As a consequence, equation (3.2) can be used for the calculation of N_I in the uncorrelated sense only if the number of measurement time-instants N_t is equal to the number of uncorrelated measurement time-instants. According to Jux et al. [2018] the need for a compromise between measurement accuracy and spatial resolution of CVV emerges from (3.3).

The DSR and the DVR are the ratio between the largest and the smallest resolvable measurement scales and the ratio between the highest value of measured velocity and the smallest resolvable variation, respectively. For time-averaged CVV measurements they are defined as [Schneiders et al., 2018]:

$$\overline{DSR} = \frac{L_x}{l_B} \tag{3.4}$$

$$\overline{DVR} = \sqrt{N_I}\left(\frac{\Delta x_{max}}{\sigma_u \Delta t}\right), \tag{3.5}$$

where L_x is the typical dimension of the measurement domain, Δx_{max} is the maximum particle displacement affordable by the particle tracking algorithm and Δt is the time separation between two frames. $\overline{DSR}$ and $\overline{DVR}$ are estimated to be in the order of 50 and 100, respectively. Both values are indicated to be larger with respect to $\overline{DSR}$ and $\overline{DVR}$ obtained in previous tomographic PIV experiments [3].

The technique of ensemble averaging can be used to obtain phase-averaged flow fields as well, as shown by Martínez Gallar et al. [2019]. In such study, the authors investigate the near wake of a flapping-wing MAV by means of Robotic Volumetric PIV. Given the periodic nature of the flow field generated by the flapping wing mechanism, the velocity is evaluated by means of a phase-averaging procedure, where the Lagrangian particles tracks are combined with the information about the flapping cycle of the wing. In that way, the ensemble average is carried out separately for each phase. The sampling instants of the tracked particles are compared with a signal representing the periodic flow and after selecting the desired phase of the cycle, the polynomial fit used by the STB algorithm to obtain the particle tracks is recomputed. Following that, a time interpolation is carried out in order to retrieve the position and velocity information at the chosen phase. Once all the available tracks have been interpolated, the ensemble averaging for the specific phase can be performed. The operation has to be repeated for each desired phase of the periodic phenomenon.

3.1.4. Robotic manipulation

Robotic Volumetric PIV results from the combination of CVV and robotics [Jux et al., 2018]. Given the compactness of a CVV probe, this can be mounted on a collaborative robotic arm in such a way to control the probe's position and orientation. With this kind of robotic handling, it is possible to adopt a measurement strategy that employs the partitioning of a large measurement volume into a number of local smaller volumes (see Figure 3.3). In this way, Lagrangian tracks can be obtained in each of this sub-volumes and, thanks to the data provided by the robotic arm, those can be transformed from each of their local reference frame to a global reference frame. Subsequently, ensemble averaging can be performed over the entire measurement volume, yielding a time-averaged or phase-averaged flow field according to the experiment being carried out. It should be noticed that the employment of the volume partitioning approach with together with the phase average of the Lagrangian tracks implies the assumption of a periodicity in the flow being measured. In fact, only this assumption allows to measure separately different regions of the total volume and then to recombine the results together finding the matching phases of the periodic phenomenon.

Representative results obtained by Jux et al. [2018] and by Martínez Gallar et al. [2019] by means of robotic manipulation of the CVV probe are shown in Figure 3.4 and 3.5, respectively.

[3] The comparison concerns only time-averaged velocity fields.

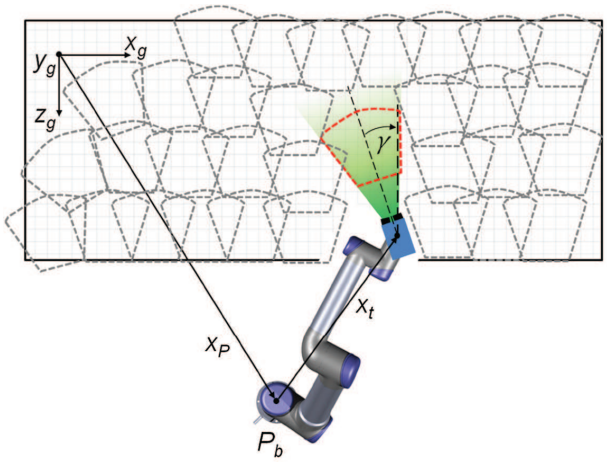

(a) Global reference frame with arbitrary region of interest. Potential measurement volumes outlined to illustrate concept of domain partitioning.

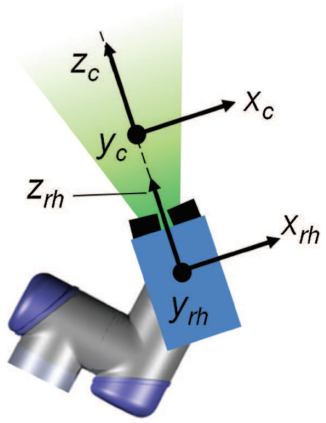

(b) Robot hand holding the CVV with indication of the local reference frames.

Figure 3.3: Illustration of the concept of measurement volume partitioning by means of robotic manipulation of the CVV probe. Reproduced from Jux et al. [2018].

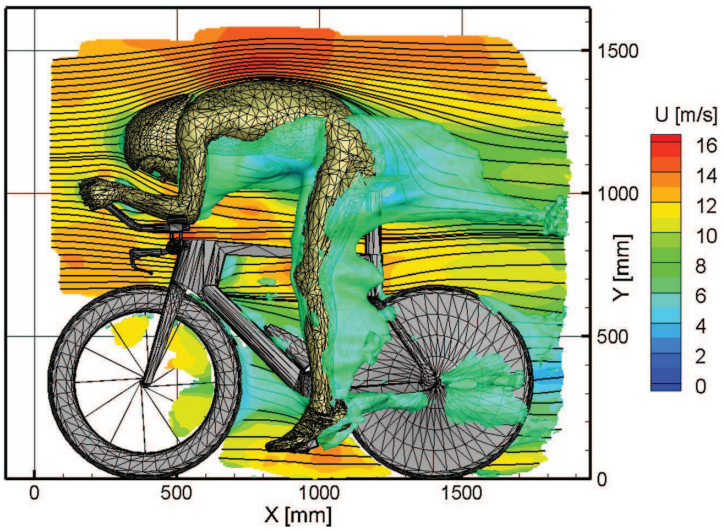

Figure 3.4: Time-averaged velocity field around the cyclist studied by Jux et al. [2018] for $u_\infty = 14 m/s$ $\left(Re = 5.5 \cdot 10^5\right)$, visualized by a contour plane of streamwise velocity u in the centre plane including surface streamlines, together with an iso-surface of $u = 7$ m/s. Reproduced from Jux et al. [2018].

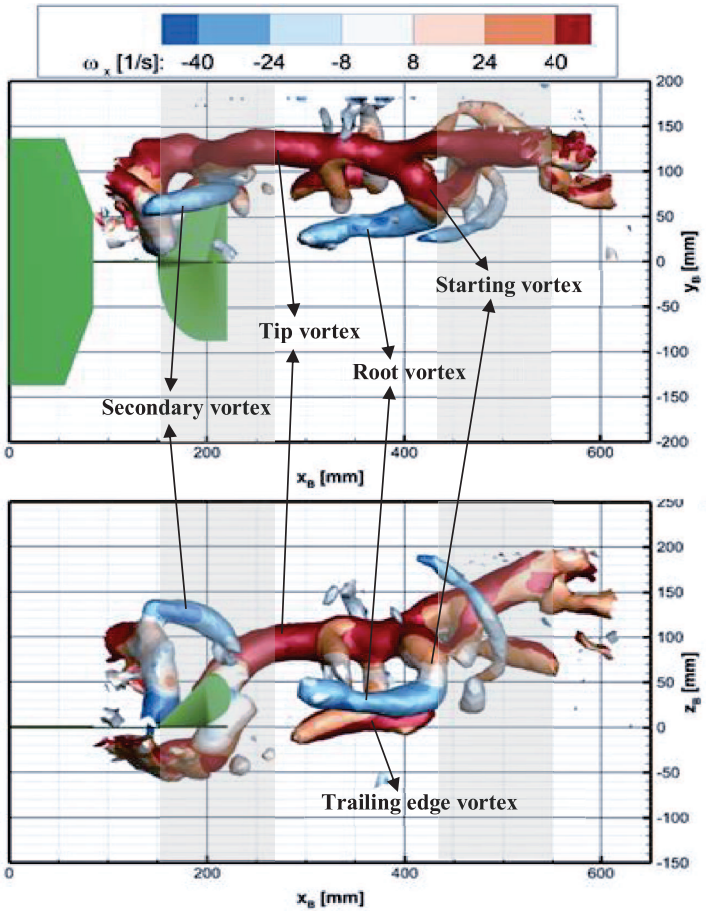

Figure 3.5: Top and side view of phase-averaged wake structures behind the MAV studied by Martínez Gallar et al. [2019], visualized by iso-surfaces of $Q = 600$ and coloured by streamwise vorticity ω_x. Reproduced from Martínez Gallar et al. [2019].

3.2. Research objective

The main research question of the present master thesis project can be formulated considering the background on aeroelastic experiments given in the introduction, the literature review performed on FSI experiments where PIV is combined with some sort of structural measurement and the explanation of the principles of the Robotic Volumetric PIV technique. As far as aeroelastic experiments are concerned, it was highlighted as modern wind-tunnel models are heavily instrumented in their inside, thus hampering the requirement of structural non-intrusiveness. Furthermore, aerodynamic characterization is often limited to force balance and pressure sensors, with almost no utilization of quantitative flow visualization techniques such as PIV. In the few cases where PIV is combined with structural measurements for FSI experiments, evaluation of volumetric data for unsteady flows over a large scale is missing. At the same time Robotic Volumetric PIV has shown an unprecedented potential for aerodynamic measurements over large scales. Furthermore, being a technique based on Lagrangian particle tracking, Robotic Volumetric PIV can be reasonably proposed for the tracking of markers belonging to a moving surface. This in turn can lead to the measurement of the displacements of a structure undergoing a dynamic deformation. Finally, the robotic manipulation of the measurement probe allows to evaluate the phase-averaged structural response of the test object over a large scale. As a consequence, the main research question reads:

How feasible is the use of Robotic Volumetric PIV for large-scale experimental aeroelastic investigations, where both an unsteady flow field and dynamic structural displacements are simultaneously measured?

In order to unambiguously answer this question, different measurable aspects have to be considered, leading to a number of sub-questions. Firstly, in Chapter 2 it was shown as the simultaneous measurement of flow and structure has a key role in the deep understanding of the physics underlying the FSI phenomenon studied. In order to obtain this kind of simultaneous measurement, the Robotic Volumetric PIV system has to acquire images including flow and structure tracers at the same time. As a consequence, in the image-processing phase, it is necessary to separate flow from structure. As it will be explained in Chapter 5, time filters will be used to achieve such separation. The first set of sub-questions is then formulated as it follows.

- *How is it possible to separate flow and structure by means of time-based filters using the images acquired by Robotic Volumetric PIV?*
- *Are there any possible pitfalls within this approach?*

Once flow and structure have been separated, the real evaluation of the measurement can be carried out. While Robotic Volumetric PIV has already been used for time-averaged and phase-averaged flow measurement over large scales, the same does not hold for structural measurement. As a consequence, the instantaneous displacements measured by the Robotic Volumetric PIV system have to be validated comparing the results with a reference measurement system. This leads to another sub-question.

- *What are the systematic and random errors of the instantaneous structural displacements measured by the Robotic Volumetric PIV system with respect to a reference measurement system?*

Following that, the suitability of the phase average approach has to be assessed. Structural measurements of each marker should show similar results in every cycle. In fact, a large scatter in the measured displacements would question the validity of the phase average approach. Furthermore, the Robotic Volumetric PIV system allows the measurement of multiple markers at the same time and it is necessary to demonstrate that the resulting phase-averaged displacements have a physical coherence. Besides this, also the scatter in the flow results has to be assessed in order to assess the suitability of the phase average approach for non-separated regions (where turbulence dominates the random errors). The related sub-questions are formulated below.

- *What is the average standard deviation of the structural displacements of a single marker across the average cycle?*
- *What is the mean and the standard deviation of the distance of multiple markers with respect to a physics-based model during the average cycle?*
- *What is the range of standard deviation of the phase-averaged velocity field?*

The last step for the assessment of the main research question consists in the recombination of flow and structural information in order to obtain a complete overview of the FSI phenomenon. For a meaningful recombination of the information, the resolved flow domain should not penetrate the structure surface. In order to assess how much this is achieved, a penetration probability will be defined and calculated across the average cycle. Finally the description of phase-averaged flow and structure will be combined together in order to study the interaction between the plate and the continuous gust. The last set of sub-questions is then proposed as it follows.

- *What is the probability of finding flow particles penetrating into the measured structure during the average cycle?*
- *Considering the flow particles penetrating into the structure, how much do they penetrate it?*
- *To what extent is it possible to combine flow and structural measurements and to achieve a coherent description of the FSI phenomenon?*

The main research question and its related sub-questions are answered by means of an experimental investigation. In such investigation an unsteady flow is generated in a wind-tunnel environment, with the aim of producing an interaction with a flexible structure that can undergo a dynamic deformation. Robotic Volumetric PIV is then used to evaluate the phase-averaged flow field and structural deformation of the entire test object. In this way, this master thesis will show the unprecedented feasibility of the combination between volumetric quantitative flow visualization and structural measurement for a large-scale aeroelastic experiment.

4

Experimental Setup and Procedures

A wind-tunnel investigation is carried out in order to answer the main research question and the related sub-questions. For the attainment of an unsteady flow field in the wind-tunnel environment, a gust generator is used. A measurable dynamic structural response to the time-varying flow is ensured by choosing a flexible aluminium plate as the test object. The near flow field over one side of the plate and its structural displacements are then measured by means of a Robotic Volumetric PIV system. Validation of the structural measurements is performed by means of another instrument typically used for vibration measurements, which is called Scanning Vibrometer. A detailed explanation of the experimental setup used for the wind-tunnel investigation is given in this Chapter, together with the procedures employed for the data acquisition.

Contents

4.1. Wind-tunnel

The facility used for the experimental investigation is the Open Jet Facility (OJF) of the TU Delft [1]. This is a closed-loop, open test section wind-tunnel with an octagonal outlet section of 2.85×2.85 m^2. The open test section is constituted by a room 13 meters wide and 8 meters high. The fan that drives the flow is powered by a 500 kW electric engine that allows to achieve a maximum speed of 35 m/s in the test section. The wind-tunnel is also equipped with several wire meshes, that reduce velocity deviations and turbulence in the free stream, and with a 350 kW radiator system used to keep the temperature of the flow constant. A schematic of the facility is shown in Figure 4.1. The contraction ratio is 3:1 and the turbulence intensity is reported to be lower than 0.5% at 1 m from the tunnel nozzle [Lignarolo, 2016].

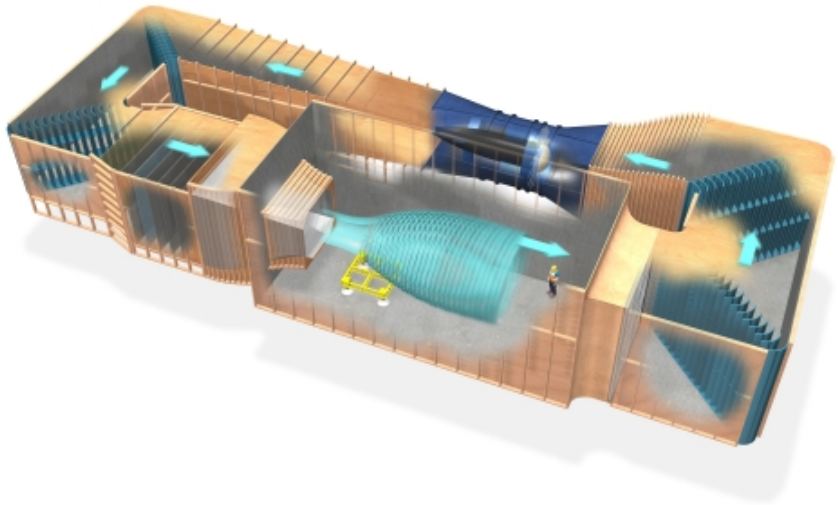

Figure 4.1: Schematic of the Open Jet Facility of the TU Delft. Reproduced from `https://www.tudelft.nl/lr/organisatie/afdelingen/aerodynamics-wind-energy-flight-performance-and-propulsion/facilities/low-speed-wind-tunnels/open-jet-facility/`, accessed: 30/11/2019.

4.2. Gust generator

The gust generator is a device developed by the Aerospace Structures and Computational Mechanics Section of TU Delft's Aerospace Faculty for the generation of gusts in the test section of the OJF. Its design and characterization is reported by Lancelot et al. [2017b] and Lancelot et al. [2017a]. Here the main features are mentioned for the sake of completeness.

The gust generator is installed in front of the outlet section of the wind-tunnel and it is composed of an aluminium frame, two active wings called gust vanes and a system for actuation and control. The function of the aluminium frame is to support the gust vanes and the actuators, so for this reason it is fixed to the ground. The gust vanes are two wings mounted vertically in the frame. They are made from foam with an internal aluminium spar acting as support structure. The span of the gust vanes is 2.88 m, which allows to cover the full height of the outlet section of the tunnel. The airfoil of the wings is a NACA 0014 and the chord has a length of 0.3 m. The spacing between the two gust vanes is 0.7 m. When the gust generator is operated, the gust vanes are deflected in order to generate a transverse velocity component with respect to the free-stream. The actuation and control system is needed to impose a deterministic motion to the gust vanes in order to obtain the desired gust profile in the flow. The system is controlled by means of a gust generator interface implemented in the *National Instrument* LABVIEW environment. An image showing the gust generator in operation is given in Figure 4.2.

[1] `https://www.tudelft.nl/lr/organisatie/afdelingen/aerodynamics-wind-energy-flight-performance-and-propulsion/facilities/low-speed-wind-tunnels/open-jet-facility/`, accessed: 30/11/2019.

Figure 4.2: Gust generator inside the OJF producing a sinusoidal gust field in the flow (visualization by means of smoke). Reproduced from Lancelot et al. [2017b].

4.3. Test object

The requirement for the test object is to show relatively large displacements in response to the gust field produced by the gust generator. Such structural displacements have to occur within the maximum wind-tunnel speed allowed by the limitations of the Robotic Volumetric PIV system employed for the measurements, as it will be explained in Section 4.4. As a consequence the test object has to be a very flexible structure. The ideal choice for a wind-tunnel investigation would be a flexible wing, however the realization of such wind-tunnel model cannot be achieved within the time frame of this master thesis. For this reason the choice falls on a simpler object and a thin rectangular aluminium plate made of 7075 aluminium alloy is picked. The plate is obtained cutting an 7075 aluminium alloy sheet with a cutting machine at the Delft Aerospace Structure and Materials Laboratory (DASML). This type of aluminium has a density of 2810 kg/m^3 and a Young modulus of 71.7 GPa. The span of the obtained plate is 1217.5 mm, while the chord and the thickness are 170.0 mm and 2.5 mm respectively. All the free edges of the plate are milled with a radius of 1 mm.

The idea behind the application of Robotic Volumetric PIV to the measurement of structural displacements is the use of small circular markers on the surface of the tested structure. In fact such markers are supposed to be imaged and tracked within a three-dimensional volume in an analogous way as it is done for flow particles. For this purpose, the plate is first painted black, in order to minimize undesired laser light reflections in the PIV cameras, and subsequently circular markers are applied with a grey paint. The application of the markers is achieved attaching a laser cut cardboard mask with circular holes to the surface of the plate and spraying the paint with a *Belton® spectRAL Lack Spray RAL 7001* can. The painted markers have a diameter of 1.5 ± 0.2 mm [2]. The circular shape is selected in order to mimic the shape of the flow particles in the acquired images, allowing in this way to use the same processing algorithms. The colour and the size of the markers are chosen according to preliminary tests that demonstrate a good trade-off between marker detectability at large distance from the measurement probe and pixel saturation avoidance with markers close to the probe.

The markers are applied on both sides of the plate in order to provide a reference when simultaneous measurements with the Robotic Volumetric PIV system and the Scanning Vibrometer are carried out, as it is explained in Section 4.6. The arrangement of the markers consists in 34 rows of 5 markers with uniform

[2] The mask manufacturer (`https://www.laserbeest.nl/laserbeest-in-english/`, accessed: 02/12/2019) claims that the lines cut by the laser can be at most 0.2 mm wide.

spacing of 35 mm.

In the wind-tunnel, the aluminium plate is clamped vertically on a support table by two L-shaped flanges, to simulate a clamped boundary condition. An illustration of the clamp mechanism and of the markers' arrangement is given in Figure 4.3. The combination of a high aspect ratio (7.16) with a very small thickness relative to the other dimensions guarantees a large flexibility of the plate. In fact, the first eigenfrequency of the presented configuration is approximately 1.6 Hz. The plate is tested at wind-tunnel speeds of 11 and 12 m/s and the expected maximum tip displacement among the different measurement cases is estimated to be 11 cm (9% of the span) [3].

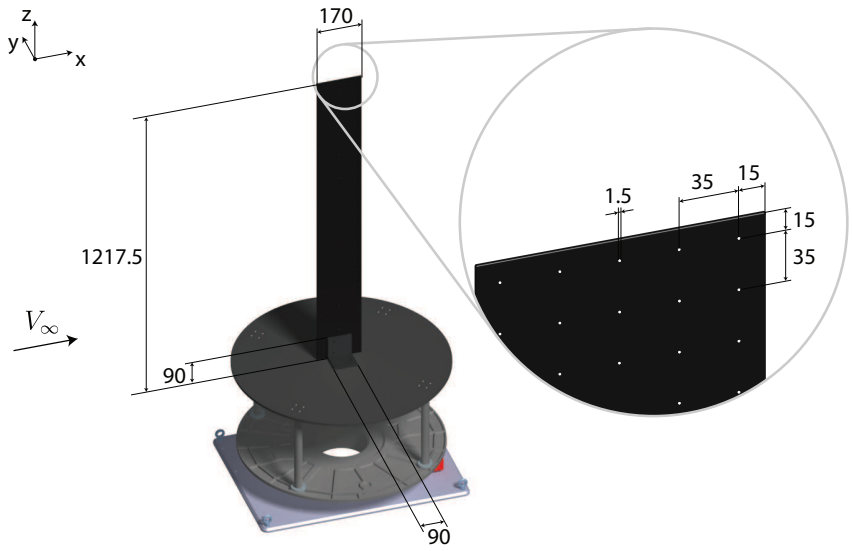

Figure 4.3: Model of the aluminium plate clamped to the support table and zoom-in of the plate's tip with markers; all dimensions in millimetres

4.4. Robotic Volumetric PIV system

4.4.1. CVV probe

The Robotic Volumetric PIV system used in the present experimental investigation employs a *LaVision MiniShaker Aero* CVV probe. The probe is equipped with four *MiniShaker 2M* cameras, which are lightweight CMOS cameras. The full frame of each camera contains and 1984×1264 pixels, with a corresponding acquisition frequency of 121 Hz. This can be increased by reducing the active frame. The probe provides an oval shaped housing to all cameras and the optical fibre that delivers the coaxial illumination, as it can be observed in Figure 4.4. The light source is provided by a *Quantronix Darwin-Duo* Nd-YLF laser, having a light wavelength $\lambda = 527$ nm and a pulse energy of 2×25 mJ at 1 kHz. A 20 mm converging spherical lens is used to focus the light beam generated by the laser head onto the free end of the optical fibre housed in the CVV probe.

A summary of the technical specification of the imaging system is given in Table 4.1. As it can be observed from the table, the active sensor is cropped with respect to the full frame in order to achieve an acquisition frequency of 821 Hz. The reason for this is twofold. Firstly, the conical illumination of the volume from the optical fibre exit of the probe is not wide enough to illuminate a large FOV at measurable distances from the probe. Furthermore, a high acquisition frequency is desired for a robust application of the STB algorithm. In fact, there is a limitation on the maximum spatial shift Δx_{max} of a flow particle from one frame to the other that has to be smaller than the average inter-particle distance $\overline{l_p}$:

$$\Delta x_{max} < \overline{l_p}. \tag{4.1}$$

The maximum measurable velocity U_{max} given a certain acquisition frequency f can be calculated as:

$$U_{max} = \frac{\Delta x_{max}}{\Delta t} = \Delta x_{max} f = \overline{l_p} f, \tag{4.2}$$

[3] The eigenfrequency and tip displacement estimations are based on numerical simulations carried out in the software MSC NASTRAN.

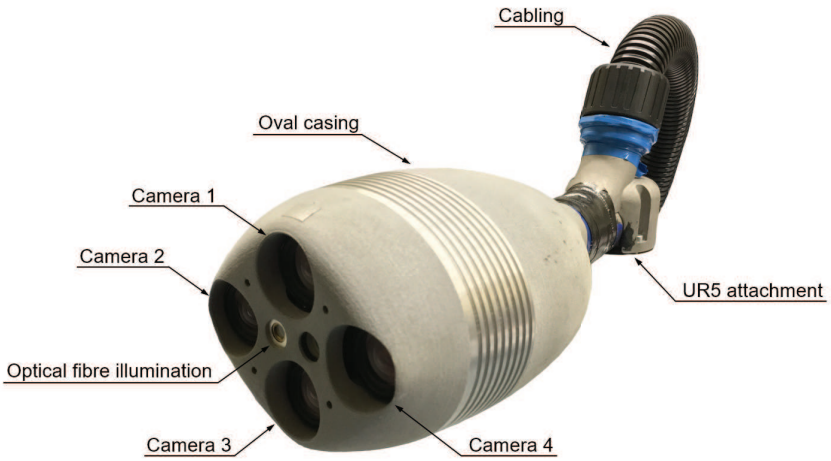

Figure 4.4: Illustration of the *LaVision MiniShaker Aero* CVV probe. Reproduced from Ordóñez [2018].

resulting in $V_{max} \approx 15.5$ m/s for $f = 821$ Hz and $\overline{l_p} \approx 1.88$ cm (the average inter-particle distance estimated for the experiment of Jux et al. [2018]). However, this velocity value is only indicative, because the real maximum velocity that can be measured is dependent on the local particle concentration and thus on the local inter-particle distance. Nonetheless choosing an acquisition frequency of 821 Hz gives a certain margin of conservativeness for the application of STB at the wind-tunnel velocities used in the present experiment.

Table 4.1: Optics and imaging specifications of the CVV probe used in the experiment.

Optics	
Focal length [mm]	4
Numerical aperture	11
Imaging	
Horizontal tomographic aperture (at $z_0 = 400$ mm) [deg] [4]	8
Vertical tomographic aperture (at $z_0 = 400$ mm) [deg]	4
Active sensor size [pix × pix]	640 × 475
Pixel pitch [μm]	4.8
Magnification (at $z_0 = 400$ mm)	0.01
Bit depth	10
Acquisition frequency [Hz]	821.7

The measurement volume available with the present CVV probe is reported by Ordóñez [2018] to be approximately of 16 L. The shape of the volume can be approximated by the truncated pyramid shown in Figure 4.5.

4.4.2. Seeding system

The seeding of HFSB in the flow is provided by a seeding rake developed by the Aerodynamic Section of TU Delft's Aerospace Faculty. This rake is composed by ten wings with 20 nozzles each, resulting in an overall seeded cross-section of 0.5×0.95 m^2 (see Figure 4.6). The generation of HFSB takes place in the nozzles where air, helium and soap are supplied and mixed. The seeding rake is placed in the settling chamber of the wind-tunnel in order to increase the particle concentration in the test section and to minimize the turbulence intensity generated by the rake itself. Considering this seeding configuration, a theoretical particle concentration can be estimated following the reasoning of Caridi et al. [2016]. For this calculation the malfunctioning of a certain number of nozzles has to be taken into account. In previous experiments the percentage of nozzles

[4] z_0 is meant as the distance from the probe along the imaging direction.

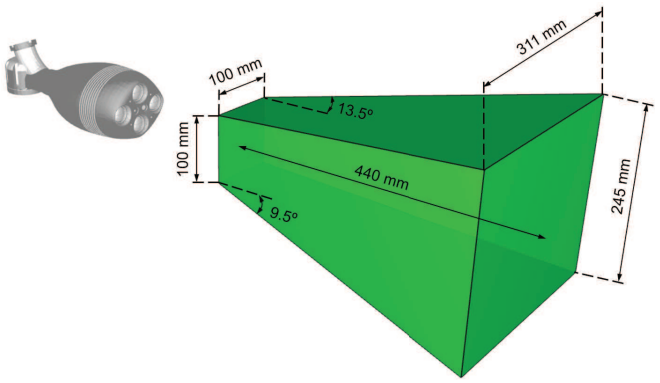

Figure 4.5: Illustration of the approximated measurement volume available with the *LaVision MiniShaker Aero* CVV probe. Reproduced from Ordóñez [2018].

not working was estimated to range from 12.5 to 25% [Ordóñez, 2018]. However, these figures are considered optimistic for the present experiment, since the used seeding rake is a prototype and a certain amount of deterioration is expected after every experiment. The percentage of not working nozzles is then conservatively assumed to be 37.5 [5]. Considering a nominal production rate of each nozzle $\dot{N} = 10^4$ bubbles/s [Faleiros et al., 2019] and a wind-tunnel speed $V_\infty = 12$ m/s, the bubble concentration is estimated as it follows:

$$C = \frac{\dot{N} n_{nozzles} r_{working}}{\frac{A_{rake}}{\rho} V_\infty} = \frac{10^4 \,\text{bubbles/s} \cdot 20 \cdot 10 \cdot (1 - 0.375)}{\frac{0.5\,\text{m} \cdot 0.95\,\text{m}}{3} 12\,\text{m/s}} \approx 0.66\,\text{bubbles/cm}^3, \tag{4.3}$$

where $n_{nozzles}$ is the total number of nozzles, $r_{working}$ is the fraction of working nozzles, A_{rake} is the area seeded by the rake in the settling chamber and ρ is the wind-tunnel contraction. However, the experimental concentration, estimated by means of the average number of particles found by the STB algorithm for different acquisitions, is much smaller than the theoretical value, amounting to 0.03 bubbles/cm^3.

A *LaVision* digital Fluid Supply Unit (FSU) is used to control the HFSB production of the seeding rake (see Figure 4.7). Such device allows to regulate the mass flow of air, helium and soap adjusting the pressure of each fluid. The average values used for the present experiment are 1.8, 2.0 and 2.0 bar, respectively.

4.4.3. Robotic arm

The CVV probe is mounted on a *Universal Robots - UR5* robotic arm. This is a collaborative robotic arm with six rotating joints, which provide the same number of degrees of freedom. An illustration of the joint system of the *UR5* is shown in Figure 4.8. The CVV probe is fixed to the tool flange of the robotic arm and in this way it can be displaced in the three-dimensional space of the wind-tunnel analogously to what is demonstrated by Jux et al. [2018]. The robotic arm manufacturer reports the position repeatibility of the tool flange to be ±0.1 mm [6]. The displacement of the probe in space is limited by the maximum reach of the robotic arm, which amounts to a radius of 850 mm around its base, as it can be observed in Figure 4.9.

4.4.4. Acquisition Computer

The Robotic Volumetric PIV system is completed by an acquisition computer providing the *LaVision* software DaVis 10.0.5 controlling both the PIV acquisition and the robotic manipulation. The latter is possible thanks to the integration of the robot simulation software RoboDK into DaVis 10.0.5. RoboDK provides an environment where CAD models of the different items forming the experimental setup (wind-tunnel, support platforms and beams, test object, etc.) can be combined with the robotic arm and its movements. This offers the possibility of working with a virtual experimental setup before setting up the real experiment in the wind-tunnel, allowing in this way a preliminary assessment of the desired measurements. An illustration of this concept is given in Figure 4.10, where the overall virtual setup is shown.

[5] This is obtained multiplying 25% by a guessed deterioration factor of 1.5.

[6] `https://www.universal-robots.com/media/1514597/101081_199901_ur5_technical_details_web_a4_art03_rls_eng.pdf`, accessed: 03/12/2019.

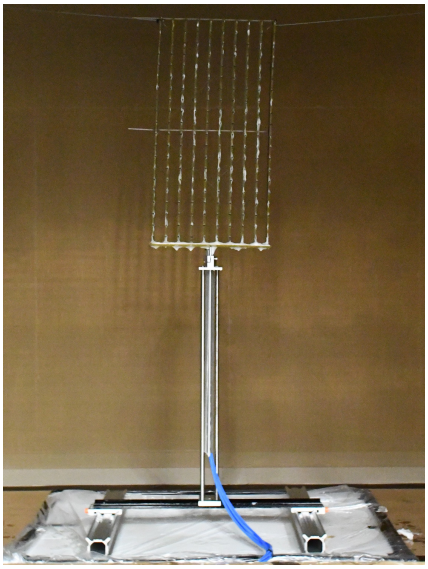

Figure 4.6: Seeding rake in the settling chamber of the OJF.

Figure 4.7: *LaVision* Fluid Supply Unit. Reproduced from `https://www.lavision.de/en/applications/fluid-mechanics/piv-system-components/seeding-devices/` (accesed: 03/12/2019).

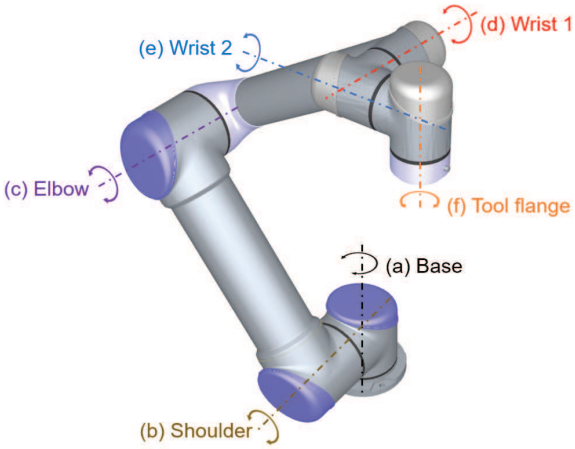

Figure 4.8: Illustration of the joint system of the *Universal Robot - UR5* robotic arm. Reproduced from Ordóñez [2018].

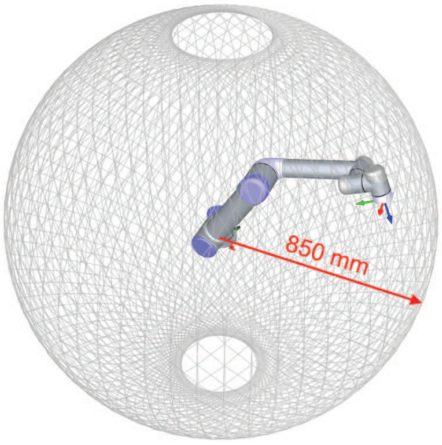

Figure 4.9: Illustration of the three-dimensional reach of the *Universal Robot - UR5* robotic arm. Reproduced from Ordóñez [2018].

One challenge that emerges when switching from the virtual experimental setup of RoboDK to the real experimental setup of the wind-tunnel is the estimation of the real distances among the objects. This is considered to be an important problem to tackle for two reasons. Firstly, the more accurate the placement of the virtual objects is with respect to reality, the closer the real measurement regions will be to their expected location in relation to the test object. This is believed to be especially useful in case of a moving object, as for the present investigation. Secondly, the integration of RoboDK with DaVis 10.0.5 permits to obtain STB tracks in one of the reference frames used in the virtual experimental setup. At this purpose it is convenient to choose a classical wind-tunnel reference frame with the origin located in the centre of the floor of the wind-tunnel outlet section, having the x-axis aligned with the flow and the z-axis going upward (see Figure 4.10).

For the present experiment the described challenge is tackled by means of the *OptiTrack* system present in the OJF. This system is composed by 12 *Flex 13* cameras placed on the ceiling of the wind-tunnel and by the optical motion capture software Motive. Placing some infrared responsive markers on the surfaces of the

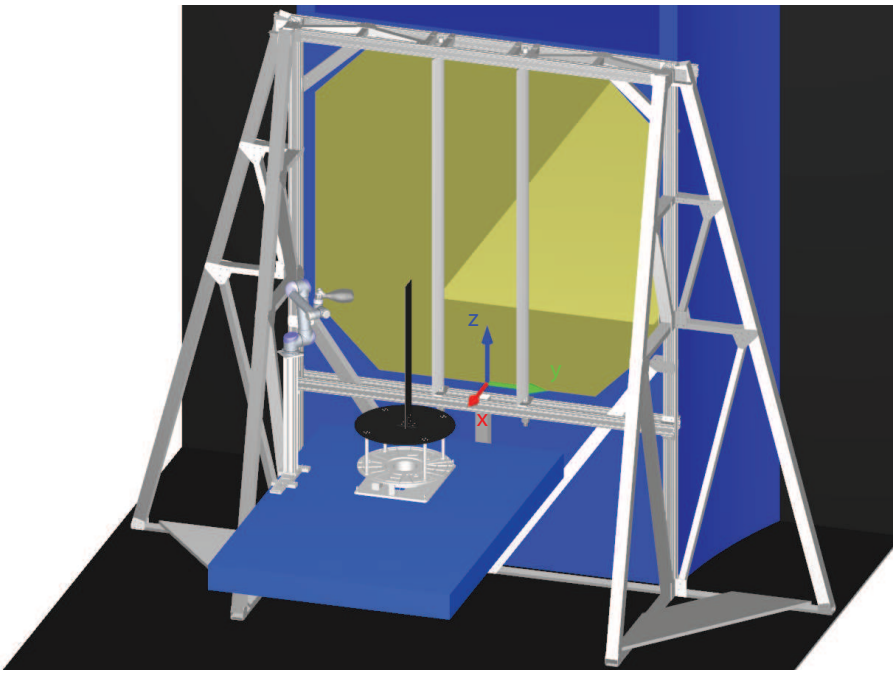

Figure 4.10: Illustration of the virtual experimental setup in RoboDk together with the reference frame used for PIV acquisitions.

various elements of the setup, it is possible to determine their relative position and input this information in the RoboDK model. More details on this procedure are given in Appendix **??**.

Finally, DaVis 10.0.5 is employed for all image acquisitions, image pre-processing and STB processing operations during and after the experiment. A summary of the specification of the acquisition computer used during the experimental campaign is given in Table 4.2.

Table 4.2: Specifications of the acquisition computer used in the experiment.

Operative system	Windows 7 professional
Processor	(2 x) Intel(R) Xeon(R) CPU E5-2650 v3 @ 2.30 GHz
RAM memory	64 GB
Local disk	SSD 850 PRO 512 GB
Storage raid	AVAGO SMC3108 SCSI 4 TB disk

4.5. Scanning Vibrometer

The Scanning Vibrometer (SV) used employed for the experiment is the *Polytec PSV-500 Scanning Vibrometer*[7]. This is a laser Doppler vibrometer used for full-field non-contact vibration measurements. It can determine the vibration velocity at a selected point by means of the Doppler effect, sensing the frequency shift of back scattered light from a moving surface. Displacement and acceleration can also be obtained by means of integration and differentiation in time, respectively. The resolution of the measured velocity is at worst 14 μm/s. The SV is placed on the opposite side of the model with respect to the Robotic Volumetric PIV system. In this way the vibrometer laser can point at the plate surface that is not illuminated by the PIV laser, so that light source contamination is avoided. A complete overview of the experimental setup in the wind-tunnel is given in Figure 4.11. The previously described reference frame used for the PIV measurements is also shown in the figure.

[7]The system used is a *PSV-500-B* with a *PSV-I-550 Scanning Head Xtra*. Technical specifications available at `https://www.polytec.com/fileadmin/d/Vibrometrie/OM_DS_PSV-500-1D_E_42445.pdf` (accessed: 03/12/2019).

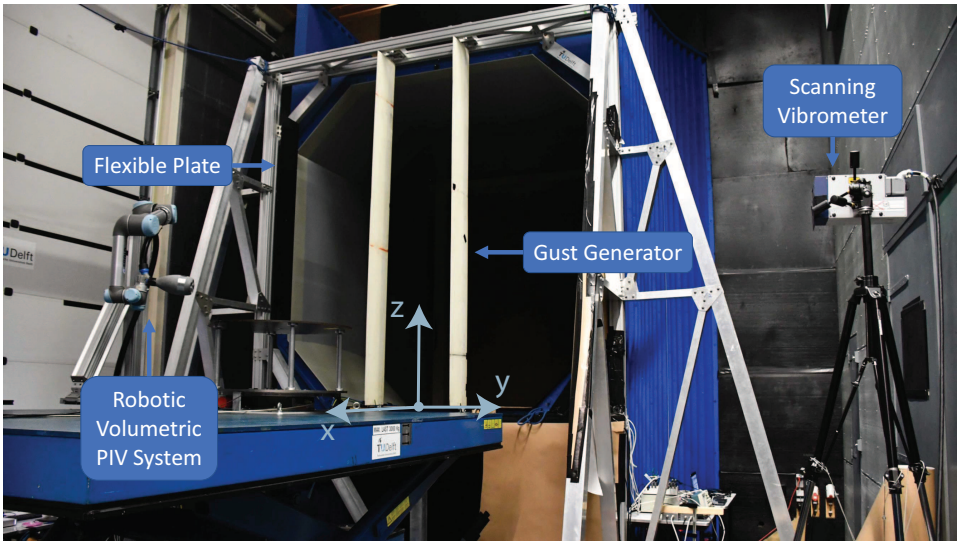

Figure 4.11: Illustration of the experimental setup together with the reference frame used for PIV measurements.

4.6. Data acquisition procedures

The Robotic Volumetric PIV and the SV systems are synchronized between themselves and with the gust generator. The synchronization is obtained with a trigger signal sent from the gust generator controller to both the measurement systems. Additionally, electric signals from the gust generator and the two measurement systems are acquired by means of a *National Instrument* acquisition station controlled by a purpose-developed interface in the LABVIEW environment. These signals include the measured angle of the gust vanes and the acquisition signals from the Robotic Volumetric PIV and the SV systems. As it will be explained later, such operation is needed for the phase reconstruction of the investigated periodic phenomenon.

The FSI phenomenon studied in the present wind-tunnel experiment consists in the response of the aluminium plate to a continuous gust excitation. Therefore, the gust vanes are actuated in a sinusoidal fashion in order to generate a periodic sine gust. An example of the measured gust vanes angle as a function of time during one acquisition is shown in Figure 4.12.

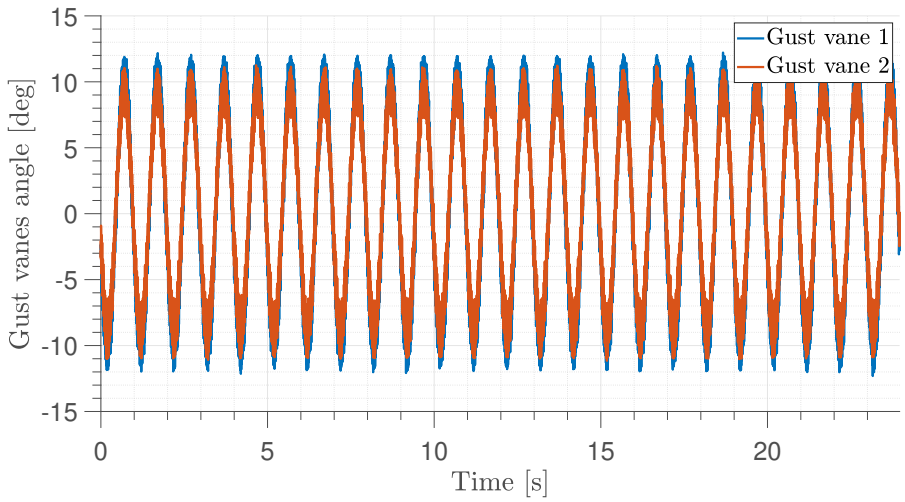

Figure 4.12: Time history of the gust vanes angle during one acquisition of the PIV-HFSB set.

Three different sets of measurement are carried out during the experiment. The first set consists of simultaneous Robotic Volumetric PIV and SV acquisition, without HFSB seeding. This offers a clean validation case for the structural measurements of the Robotic Volumetric PIV system. During the second set of measurements, the HSFB generator is switched on. In this way, the capability of the Robotic Volumetric PIV system to deliver valid structural measurement in the presence of flow tracers can be assessed. The third set

of measurements involves the use of the Robotic Volumetric PIV system for the measurement of the FSI phenomenon over the entire span of the plate. Besides the mentioned measurement sets, additional acquisitions are performed with the PIV system in order to measure the static position of the markers in wind-tunnel off conditions and for the two wind-tunnel speeds tested.

The physical and acquisition parameters of each set of measurements are shown in Table 4.3. The PIV acquisition frequency is reduced when no HFSB are used in order to store a smaller amount of data. This is justified by the fact that the plate is supposed to respond with the same frequency as that of the gust (0.9 Hz), which is very small with respect to the acquisition frequency and it entails a lower frequency requirement for the tracking of structural markers with STB. Furthermore, a smaller gust amplitude is employed when the Robotic Volumetric PIV system is used simultaneously with the SV. This is done with the aim of providing an experimental condition where the SV can be regarded as ground truth, since for large displacements of the plate the point measured by the SV experiences a substantial motion over the plate surface and it cannot be considered fixed. For the real investigation of the FSI phenomenon a large gust amplitude is desired for a clear observation of the dynamic behaviour of both flow and structure. Finally, 3 PIV volumes are acquired for the PIV-SV and the PIV-SV-HFSB set, while 14 PIV volumes are acquired for the PIV-HFSB set. In fact, only few markers are considered to validate the structural measurement of the Robotic Volumetric PIV system, as it will be shown in Section 6.1. The position of the acquired PIV volumes is shown in Figure 4.13.

Table 4.3: Physical and acquisition parameters of the studied measurement cases.

	PIV-SV	PIV-SV-HFSB	PIV-HFSB
Physical parameters			
Wind-tunnel speed [m/s]	11	11	12
Gust reduced frequency	0.044	0.044	0.045
Gust vanes deflection [deg]	5	5	10
Acquisition parameters			
PIV acquisition frequency [Hz]	200	821.7	821.7
SV acquisition frequency [Hz]	1000	1000	
# gust cycles per acquisition	20	20	20
PIV images per acquisition	4400	18076	16433
# PIV volumes	3	3	14
# acquisition loops per PIV volume	1	1	8
SV samples per acquisition	2200	2200	
# SV points	9	6	

Each session of data acquisition is performed in loops of data recording separated by a certain amount of saving time. For each session, the gust generator is started and the measurement systems are kept on hold until the transient has died out. The PIV and SV acquisition of the first loop is started by means of a trigger signal sent by the gust generator controller. About 5 seconds before that, the recording of the electric signals is started manually. Once the first loop has been acquired, the gust generator stops and the measurement systems save the acquired data. From the second loop onwards the described operations are automatized and repeated for the desired number of loops.

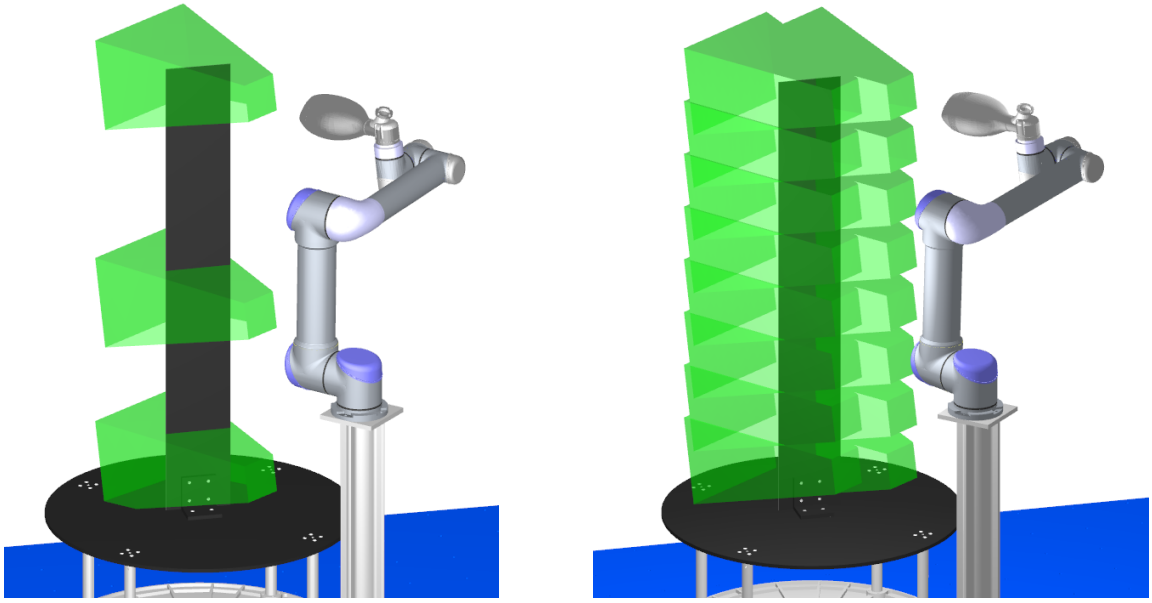

(a) PIV volumes acquired for the PIV-SV and PIV-SV-HFSB sets.

(b) PIV volumes acquired for the PIV-HFSB set.

Figure 4.13: Illustration of the PIV volumes acquired during the experiment.

5

Data Analysis and Reduction Techniques

The experimental data gathered during the experimental campaign consists in a large amount of images acquired with the Robotic Volumetric PIV system, in a set of text files generated by the Scanning Vibrometer and in another set of text files generated by the *National Instrument* acquisition station. In order to answer the research question, these sets of data have to be properly analysed. The techniques employed for such purpose are explained in this chapter.

The analysis of the PIV datasets is discussed in Section 5.1. Most of the datasets are acquired imaging simultaneously both the flow tracers and the structural markers. Thus the first challenge that emerges is the one of separating flow and structure, which is tackled in Section 5.1.1. Once separated set of images are obtained, image pre-processing operations are applied to prepare the images for the real processing. This happens with the application of the STB algorithm, which finds the particles' track for both HFSB and structural markers. Finally, the obtained tracks are post-processed in order to obtain phase-averaged flow field and structural displacements. These operations are described in Section 5.1.2 and 5.1.3, respectively for the flow and the structure images. Finally, the analysis of SV data is discussed in Section 5.2.

Contents

5.1. PIV data analysis

5.1.1. Flow and structure image separation

The PIV images acquired with the active HFSB generator contain both flow and structure tracers. As a consequence, the first challenge in the measurement of the FSI phenomenon is to obtain separate sets of images for flow and structure. This problem is tackled by making the hypothesis that, on average, structural markers move much slower with respect to flow particles. With this assumption, it is possible to use image preprocessing operations based on time-series to separate flow from structure. For the elimination of structural markers the temporal high pass filter proposed by Sciacchitano and Scarano [2014] is used. This filter is based on the decomposition of the pixel intensity signal in the frequency domain, where the low-frequencies, associated with reflections from steady and slow-moving surfaces, are filtered out. A kernel of 7 images is used for the application of the temporal high pass filter. The time minimum filter available in DaVis 10.0.5 [LaVision, 2018a] is employed to obtain image sets with only structural markers. This filter retains the minimum intensity for each pixel over a certain number of consecutive images. Since structural markers occupy the same pixels for a larger number of images with respect to flow tracers, the latter can be eliminated by taking the minimum over a small enough number of images. A size of 3 images is selected as kernel of the filter. An example of the separated flow and structure images is shown in Figure 5.1.

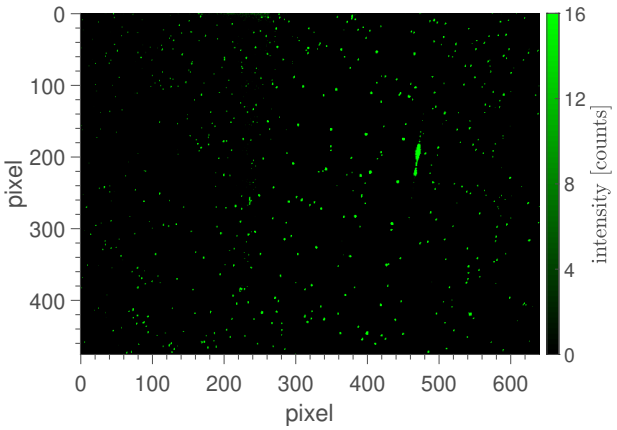

(a) Raw image.

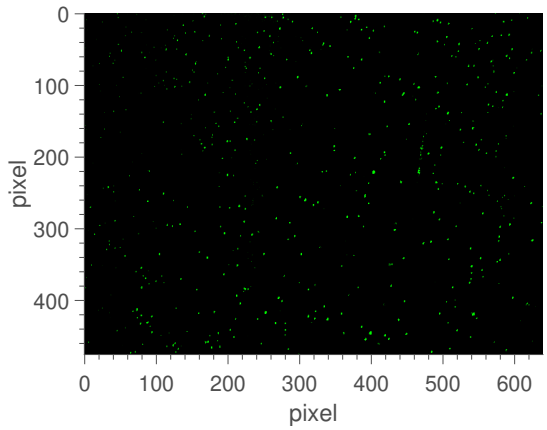

(b) Flow image.

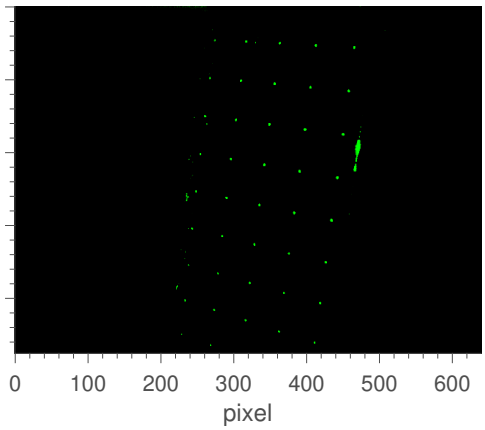

(c) Structure image.

Figure 5.1: Raw image and pre-processed images with separated flow tracers and structural markers.

A qualitative analysis of the images obtained with the described operations and the combined flow and structural results shown in Chapter 6 reveal a successful separation of flow particles and structural markers. However, it should be noticed that the use of the time minimum filter has a potential pitfall in case of the presence of a region of separated flow. In fact, slow-moving flow particles in such region may appear in the images resulting from the application of the time minimum filter, potentially compromising the measurement of structural markers. An alternative ideal filter avoiding this problem could consist in the dual of the

temporal high pass filter proposed by Sciacchitano and Scarano [2014], that is to say a temporal low pass filter filtering out the high-frequencies associated with the pixel intensity of the flow particles. Nevertheless this solution would rely on a clear frequency separation between the pixel intensity signal of the structural markers and of the flow particles, which in turn would imply the presence of a steady or slow-moving object. For surfaces moving at a comparable velocity with respect to the flow particles, a possible solution may be the use of markers with a non-circular shape as to produce an anisotropic distribution of pixel intensity in the image (e.g. cross-shaped markers). In this way spatial filters may be sued to separate the structural markers from flow particles without relying on assumptions on their temporal behaviour.

However, given the results obtained with the use of the temporal high pass filter and the time minimum filter, the investigation of alternative filters for the separation of structure and flow images is considered out of the scope of this thesis. All the images containing both structure and flow tracers are processed with the mentioned technique and using the mentioned parameters. For images including only one kind of tracers no filter is applied and the raw images are processed directly with the operations described in the following chapters.

5.1.2. Flow processing

Image pre-processing

Once separate flow and structure images are obtained, a further set of image pre-processing operations is applied, with the aim of achieving nicely shaped particle images with homogeneous intensities and zero background [LaVision, 2018b]. These operations consist in a subtraction of sliding minimum and in a local normalization of the pixel intensity. The parameters used for the pre-processing of flow images are summarized in Table 5.1. The main effect obtained in the pre-processed images is the intensity increase of particles at the edges of the FOV, while not much improvement is achieved in terms of background given the already good background intensity level of the starting images.

Table 5.1: Parameters used for pre-processing of flow images.

Sliding minimum subtraction	
Kernel [pix]	11
Local average normalization	
Kernel [pix]	50
Local average computation	For each image separately
Normalization to first frame	Yes

Patricle tracking

The operation of particle tracking on the pre-processed images is carried out by means of the STB algorithm. For its application, the calculation of a volume self-calibration [Wieneke, 2008] and of an optical transfer function (OTF) [Schanz et al., 2012] is recommended. To perform these operations robustly, a dataset including pre-processed flow images from different acquisitions is created. This allows to considerate a large spectrum of imaged particles and consequently to obtain solid results in terms of volume self-calibration and OTF. The parameters used for the application of STB algorithm are summarized in Table 5.2. Thanks to the integration of RoboDK into Davis 10.0.05, the positional and velocity data of the calculated tracks are obtained directly in the wind-tunnel reference frame (see Figure 4.10).

Track post-processing

Once a Lagrangian description of the flow is obtained, a phase-average approach is employed to convert the information into an Eulerian description on a structured grid. For this purpose, the cycles and the phases among the different PIV acquisitions have to be identified first and subsequently the ensemble average of the tracks' velocity information has to be carried out for each phase.

As far as the identification of cycles and phases is concerned, the following strategy is employed. For every PIV recording, a least square regression is used to fit a sine wave to the two signals acquired in LabVIEW corresponding to the gust vanes' angle:

$$\alpha_{gv}(t) = a\sin(bt + c) + d \tag{5.1}$$

Table 5.2: STB parameters used to process flow images.

General	
X interval [mm]	$[-250.153, 399.805]$
Y interval [mm]	$[-250.089, 249.957]$
Z interval [mm]	$[50.055, 700.013]$
Threshold for 2D particle detection [counts]	8
Allowed triangulation error [vox]	1
Shaking	
Outer loop iterations	4
Inner loop iterations	4
Particle position shaking [vox]	0.10
Remove particles closer than [vox]	1.00
Remove particles less intense than fraction of average intensity	0.10
Shaking	
Make OTF smaller	1
Increase in particle intensity for residuum computation	1
OTF radius for residuum computation	Automatic
Tracking	
Minimum track length	4
X velocity limit [vox]	-20.51 ± 66.91
Y velocity limit [vox]	-2.29 ± 1.61
Z velocity limit [vox]	11.95 ± 27.63
Max absolute change in particle shift [vox]	1.00
Max relative change in particle shift [%]	20.00
Median filter	Off

where t is the time variable and a, b, c and d are the coefficients of the regression. A reference sine wave is calculated based on the results of the regression and it has the following form:

$$f_{ref}(t) = \sin(bt + c) = \sin\left(\omega_{ref} t + \varphi_{ref}\right). \tag{5.2}$$

The reference cycle period is then defined as $T_{ref} = 2\pi/\omega_{ref}$ and it is considered as the reference period of the periodic FSI phenomenon studied. The identification of the cycles within a single PIV acquisition is completed by defining the starting point in time of the first cycle with respect to the instant of the first PIV image. This is done calculating the time instant that satisfies the following condition:

$$\max(t) \mid \sin\left(\omega_{ref} t + \varphi_{ref}\right) = 0 \quad \text{with} \quad t < t_{PIV}, \tag{5.3}$$

where t_{PIV} is the instant of the first PIV image in the LABVIEW dataset. This means that the first cycle is defined to start at the closest 2π phase of the reference signal preceding the start of the PIV recording. The cycles are then separated by the reference period T_{ref} and the end of the last cycle is set after the time instant corresponding to the last PIV image. A graphical representation of the cycles identification is given in Figure 5.2. The calculated reference period results on average less than 0.1% different with respect to the nominal gust period set with the gust generator controller.

Once the cycles have been defined, the identification of the phases of each cycle follows directly by dividing the first cycle into the desired number of phases. The time instants associated with each phase are found by adding a multiple of T_{ref} to the time instants corresponding to the same phase of the first cycle. An illustration of this is given in Figure 5.3.

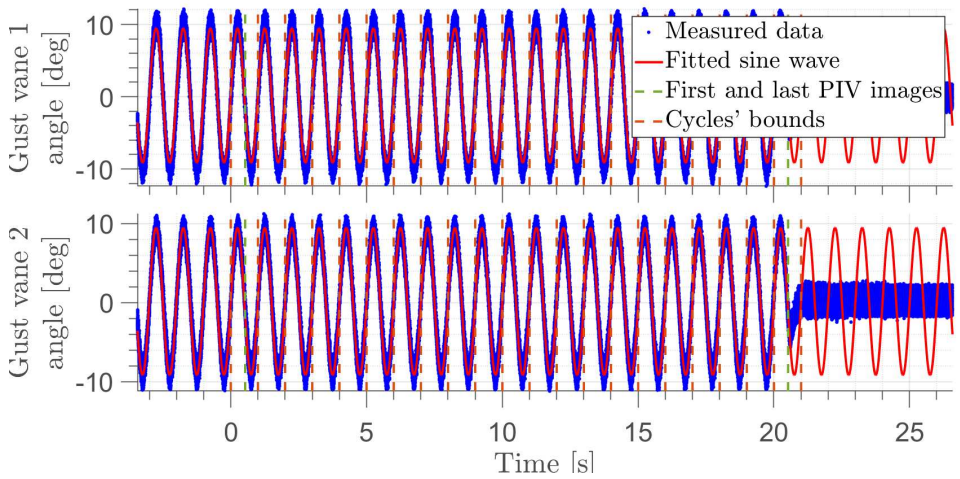

Figure 5.2: Illustration of the cycles' identification within one acquisition. The regression of the sine wave is carried out considering the interval between the first and last PIV images. Time $t = 0$ s is set at the beginning of the first cycle considered for phase-averaging.

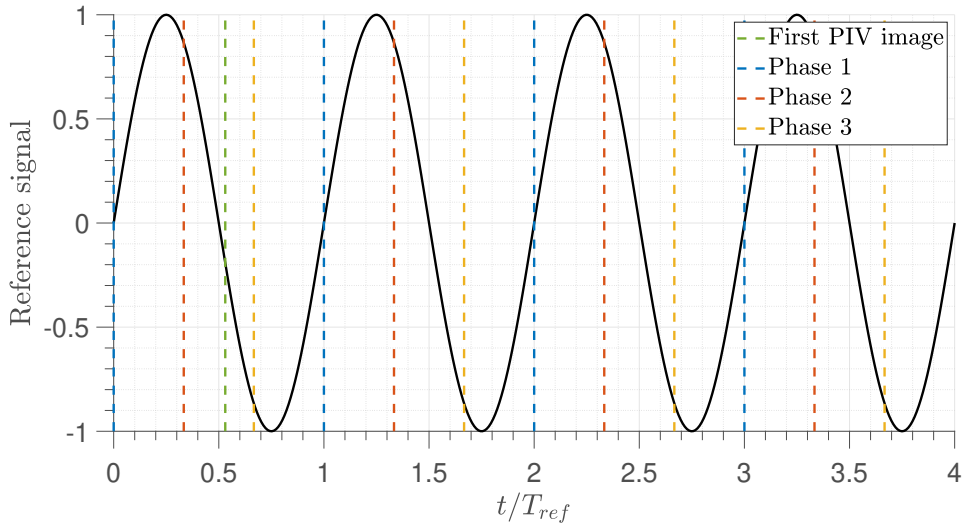

Figure 5.3: Illustration of the phases' identification within the first half of one acquisition. Time $t = 0$ s is set at the beginning of the first cycle considered for phase-averaging.

The identification of cycles and phases is performed for all PIV acquisitions and with the completion of this step the ensemble averaging of the tracks velocity information can be carried out. For each recording, the temporal information of the particles is corrected with the time offset given by the difference between the first PIV instant and the starting instant of the first cycle of the reference signal. Subsequently, the temporal information of each recording is collapsed into one cycle and it is made non-dimensional by dividing the time instants with the reference period T_{ref}. This non-dimensionalization allows to have a common temporal reference frame for particles belonging to different PIV acquisitions. At this point, a structured cartesian grid is generated based on the volume spanned by the entire set of particles, with each point of the grid representing the centroid of an interrogation bin. For each phase a subset of particles is selected such that it falls within a certain non-dimensional time window centred on the non-dimensional time instant corresponding to the phase. Following this, the particles falling inside each interrogation bin are found and the ensemble average is carried out.

The linear size of the bins forming the structured grid is relatable to the desired uncertainty level of the mean velocity. In fact, considering equation (3.3), the minimum number of uncorrelated measurement sam-

ples $N_{I,min}$ needed to obtain an uncertainty $\epsilon_{\overline{u}}$ with coverage factor k_c and a standard deviation σ_u is:

$$N_{I,min} = \left(\frac{k_c \sigma_u}{\epsilon_{\overline{u}}} \right)^2, \tag{5.4}$$

In turn, the linear size of the bin l_B follows from equation (3.2):

$$l_B = \sqrt[3]{\frac{N_{I,min}}{C\,N_t}}, \tag{5.5}$$

where C is the instantaneous concentration of the tracers and N_t is the number of measurement time-instants.

For the ensemble average inside each interrogation bin different methods are considered here besides the simple average computation used by Jux et al. [2018], also referred to as top-hat filter. Agüera et al. [2016] propose two advanced spatial averaging methods: the Gaussian filter and the polynomial fit. The former consists in a weighted average of the velocity where the weights are given by an Gaussian function:

$$\overline{u_i} = \frac{1}{\sum_{n=1}^{N_p} g_n} \sum_{n=1}^{N_p} g_n \cdot u_{i,n}, \tag{5.6}$$

where $\overline{u_i}$ is the averaged i component of the velocity, N_p is the number of particles inside the interrogation bin, $u_{i,n}$ is the i component of the velocity of the n-th particle and g_n is the weighting factor, which is defined as:

$$g_n = \exp\left(-\frac{||x_n||^2}{l_B^2} \right), \tag{5.7}$$

where $||x_n||$ is the Euclidean distance of the n-th particle from the bin centroid. The standard deviation of $\overline{u_i}$ is also calculated with the same weighting:

$$\sigma_{u_i} = \sqrt{\frac{1}{\frac{N_p - 1}{N_p} \sum_{n=1}^{N_p} g_n} \sum_{n=1}^{N_p} g_n \left(u_{i,n} - \overline{u_i} \right)^2}. \tag{5.8}$$

The polynomial fit consists in modelling the velocity distribution inside the interrogation bin with a polynomial function. Two functions are considered here: a first order and a second order polynomial. For the latter, the velocity components are expressed in the following form:

$$u_i\left(\Delta x, \Delta y, \Delta z\right) = a_0 + a_1 \Delta x + a_2 \Delta y + a_3 \Delta z + a_4 \Delta x^2 + a_5 \Delta x \Delta y + a_6 \Delta y^2 + a_7 \Delta x \Delta z + a_8 \Delta y \Delta z + a_9 \Delta z^2, \tag{5.9}$$

where $\left[\Delta x, \Delta y, \Delta z\right]$ is the distance vector from the centroid of the interrogation bin. The first order polynomial function can be easily obtained removing the higher order terms. The coefficients $a_0, a_1, \ldots, a_9$ are unknown and have to be calculated finding the least-square solution of a system of equations assembled using the positional and velocity information of the particles (for more details see Agüera et al. [2016]). In this way, the found polynomial function is the one that best fits the particle data within the interrogation bin in a least-square sense. The mean velocity in the interrogation bin is taken as the velocity at the bin centroid:

$$\overline{u_i} = u_i\left(0, 0, 0\right), \tag{5.10}$$

while the standard deviation is calculated taking into consideration the velocity variation predicted by (5.9):

$$\sigma_{u_i} = \sqrt{\frac{1}{N_p - 1} \sum_{n=1}^{N_p} \left(u_{i,n} - u_i\left(\Delta x_n, \Delta y_n, \Delta z_n\right) \right)^2}, \tag{5.11}$$

where $\left[\Delta x_n, \Delta y_n, \Delta z_n\right]$ is the distance vector of the n-th particle from the bin centroid. A graphical illustration of the top-hat filter (simple average), the Gaussian filter and the polynomial fit is given in Figure 5.4 for a one-dimensional case.

For phase-averaged flow fields, the methods proposed by Agüera et al. [2016] can be extended to the temporal dimension, becoming in this way spatio-temporal ensemble averaging methods. Analogously to

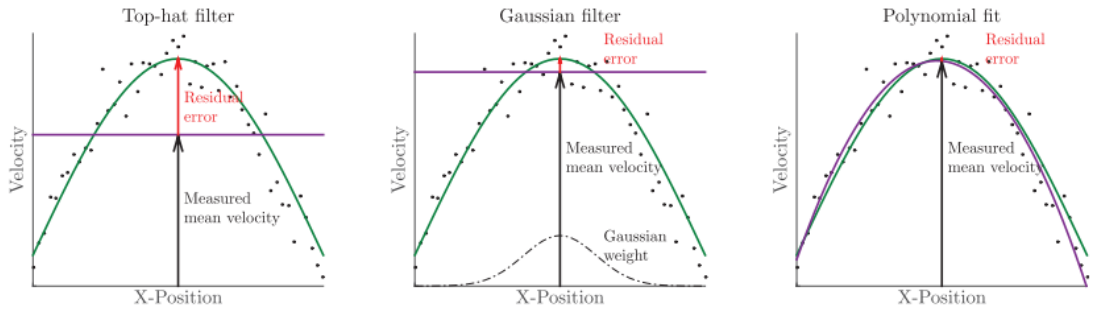

Figure 5.4: Illustration of the unresolved velocity gradients within an interrogation bin. Particle velocities are represented with black dots, exact mean velocity field by a green curve and filtered mean velocity by a purple curve. Reproduced from Agüera et al. [2016].

the spatial bin with a linear size l_B, a temporal bin with size t_B has to be defined. This temporal bin consists in a time window centred on each considered phase that is used to include the temporal information of all particles belonging to such time window in the execution of the ensemble average. Since all operations are performed using non-dimensional time, the size of the temporal bin is given as t_B/T_{ref}. The idea behind the extension of the methods proposed by Agüera et al. [2016] is to use the temporal information of the particles adding a time-dependent component to the weights of the Gaussian filter (see (5.7)) and to the polynomial function describing the velocity variation inside the interrogation bin (see (5.9)). With such addition, the weights of the Gaussian filter are expressed as:

$$g_n = \exp\left(-\left(\frac{||x_n||^2}{l_B^2} + \frac{\left(\Delta t/T_{ref}\right)^2}{\left(t_B/T_{ref}\right)^2}\right)\right) \tag{5.12}$$

and the quadratic distribution of the velocity becomes:

$$\begin{aligned} u_i\left(\Delta x,\Delta y,\Delta z,\Delta t/T_{ref}\right) = {} & a_0 + a_1\Delta x + a_2\Delta y + a_3\Delta z + a_4\Delta x^2 + a_5\Delta x\Delta y + a_6\Delta y^2 + a_7\Delta x\Delta z + a_8\Delta y\Delta z + a_9\Delta z^2 + \\ & + a_{10}\Delta t/T_{ref} + a_{11}\Delta x\Delta t/T_{ref} + a_{12}\Delta y\Delta t/T_{ref} + a_{13}\Delta z\Delta t/T_{ref} + a_{14}\left(\Delta t/T_{ref}\right)^2, \end{aligned} \tag{5.13}$$

where $\Delta t/T_{ref}$ is the non-dimensional time separation from the considered phase of the cycle. Also in this case, the linear distribution of the velocity can be easily obtained removing the higher order terms. Similarly to the spatial quadratic distribution, the mean velocity in the interrogation bin is taken as the velocity at the bin spatio-temporal centroid:

$$\overline{u_i} = u_i\left(0,0,0,0\right), \tag{5.14}$$

and the standard deviation is calculated taking into account also the temporal variation of the predicted velocity:

$$\sigma_{u_i} = \sqrt{\frac{1}{N_p-1}\sum_{n=1}^{N_p}\left(u_{i,n} - u_i\left(\Delta x_n,\Delta y_n,\Delta z_n,\Delta t_n/T_{ref}\right)\right)^2}, \tag{5.15}$$

where $\Delta t_n/T_{ref}$ is the non-dimensional separation time from the considered phase.

Once an Eulerian description of the flow is obtained finding the mean velocity in each bin for each phase, the uncertainty of such mean velocity can be assessed. The expression for the uncertainty of the mean velocity was given with equation (3.3) and it is repeated here for convenience:

$$\epsilon_{\overline{u}} = \frac{k_c\sigma_u}{\sqrt{N_I}}. \tag{5.16}$$

However, for the present study the calculation of N_I by means of (3.2) is not considered to return a reliable value representing the number of uncorrelated velocity measurement. In fact, the number of measurement time-instants N_t is not guaranteed to correspond to the number of uncorrelated measurement time-instants. This is motivated by the fact that the PIV acquisition frequency is much higher to the frequency corresponding to the gust periods used during the experiment, which can be considered as the integral time-scale of the flow.

Furthermore, for spatio-temporal ensemble averaging the use of a temporal bin size larger than the image separation time allows more particles belonging to the same track to participate to the averaging process. These particles are strongly correlated in time and consequently they should not be considered separately for the calculation of N_I.

For this reason, the uncertainty of the mean velocity is calculated in a different way:

$$\epsilon_{\overline{u}} = \frac{\sigma_u}{\sqrt{N_{unc}}}, \tag{5.17}$$

where N_{unc} is a conservative estimate of the number of uncorrelated velocity measurements and where a $k_c = 1$ has been selected. N_{unc} is obtained dividing the observation time T_{obs} with the integral time-scale of the flow, which here is taken to correspond to the gust period:

$$N_{unc} = \frac{T_{obs}}{T_{gust}}. \tag{5.18}$$

The observation time is in turn given by the acquisition time of a PIV volume T_{acq} multiplied by the number of acquisitions of the same volume n_{acq}:

$$T_{obs} = T_{acq} n_{acq}. \tag{5.19}$$

Considering the PIV-HFSB measurement set (see Table 4.3) and a minimum number of 6 acquisitions for each PIV volume, the number of uncorrelated velocity measurements is estimated to be approximately 120.

In conclusion, the processing of the flow images is summarized in Figure 5.5.

5.1.3. Structure processing

Image pre-processing

The assessment of the plate's structural response relies on the possibility to measure the markers' displacement by means of the Lagrangian particle tracking algorithm STB. For this purpose, the separated structure images are pre-processed using the same parameters shown for the flow images in Table 5.1. An example of the result of such image pre-processing is shown in Figure 5.6. The main effect is to reduce the intensity of undesired edge reflections.

Patricle tracking

Also for the application of STB to the structure images a volume self-calibration and an OTF are needed. Since markers look similar to flow tracers in the pre-processed images, the same results obtained with flow images may be used for structure processing. However, a specific dataset including marker images from different acquisitions is created to obtain both the volume self-calibration and the OTF because this procedure is observed to provide significantly better results. The STB parameters used for the processing of structure images are summarized in Table 5.3. As it can be observed, in this case the application of the STB algorithm is performed via the use of 8 iterations for both outer and inner loop and by a 0.05 vox shaking. This is done to compensate the significant instantaneous particle positional error of the CVV probe along the imaging direction (in the order of 1 mm, as mentioned in Section 3.1.1). The consequent high computational cost is affordable given that the number of tracks in a structure dataset is several order of magnitude lower than the one in a flow dataset. Also in this case the positional data of the calculated tracks are obtained directly in the wind-tunnel reference frame.

Track post-processing

The STB processing results in several tracks for each marker. In fact, the tracking of a marker with a single STB track for the entire acquisition is never achieved. This can be mainly ascribed to the positional uncertainty of the tracked marker, which may result in accelerations that violate the limits imposed by the employed parameters. In order to describe the instantaneous displacement over the entire acquisition time, an algorithm is developed to join the tracks associated with the same marker. The flow chart of such algorithm is given in Figure 5.7. In brief, the algorithm advances one time step at a time and for each marker it calculates a predicted trajectory fitting a quadratic function to the known coordinates of the marker within a certain time interval. This predicted trajectory is used to evaluate the coordinates at the time instants of the new tracks belonging to the time step being analysed. Subsequently, the average and the standard deviation of the distances between the real and the predicted particle position is evaluated for each new track. The track with an average distance plus one standard deviation smaller than a certain search radius is added to the analysed marker.

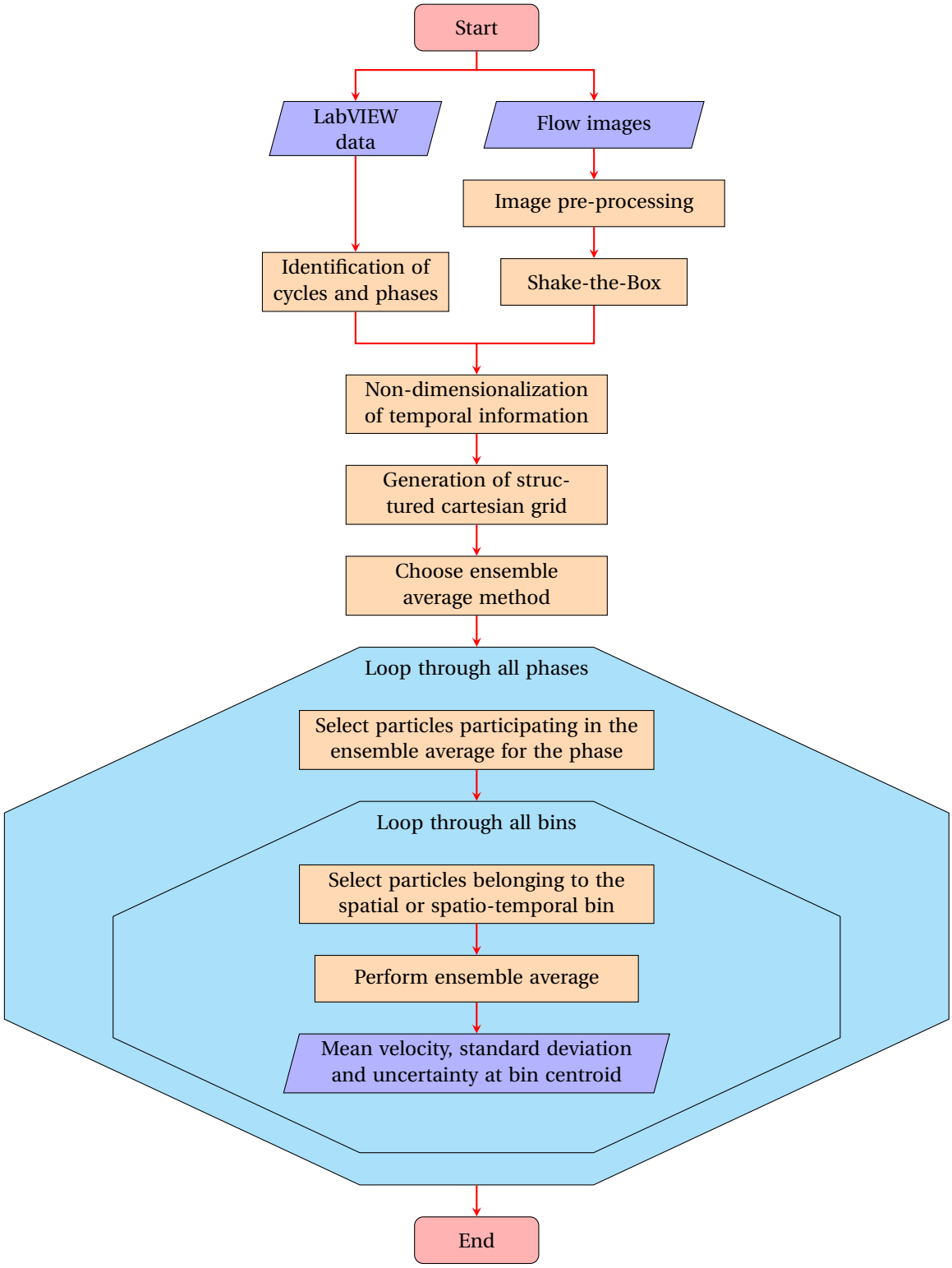

Figure 5.5: Flow chart of the processing strategy employed for the flow images.

If more than one track satisfies such criterion, the track with the smallest average distance is assigned to the marker, while if no track satisfies the criterion the algorithm moves on to the next marker. Once all markers are analysed, the algorithm progresses to the next time step.

Two parameters have to be defined in order to run the algorithm. One is the time interval interval used for the regression of the quadratic trajectory of the marker, Δt_{fit}. This time interval also acts as a maximum

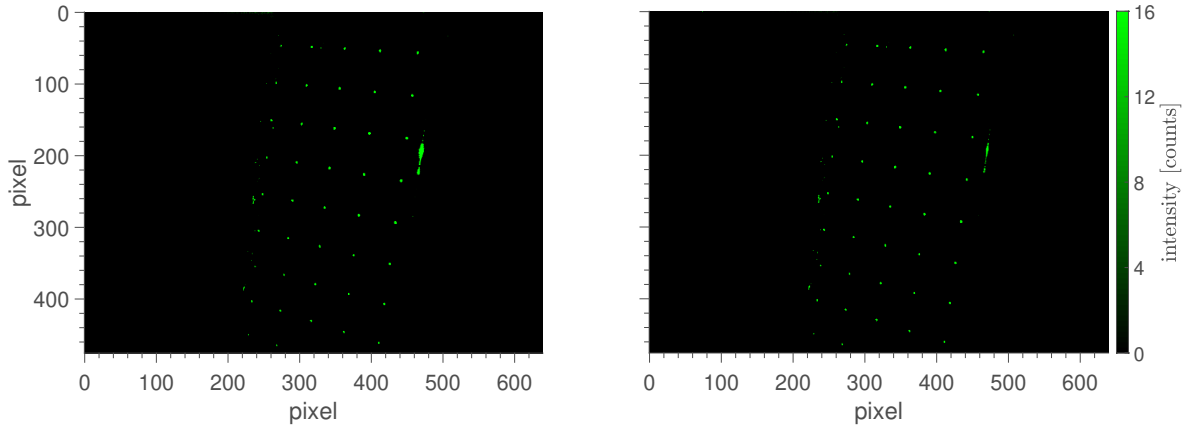

(a) Time minimum filter result

(b) Image pre-processing result.

Figure 5.6: Illustration of structure image pre-processing.

separation time allowed between an existing marker and a potential new track to be added. Based on some tests, a value of 1/4 of the nominal gust period is used throughout all processing operations. The other parameter is the previously mentioned search radius r_s. Its value is varied from time to time according to the need of relaxing or restricting the criterion to add new tracks to existing markers. However, the most used value amounts to half the distance between two markers, that is to say 17.5 mm.

For the calculation of the phase-averaged displacement of the markers, a strategy similar to the polynomial fit method described for the ensemble average of flow particles is employed. First, the cycles and the phases of the different PIV acquisitions are identified in the same way as explained for flow tracks post-processing. Subsequently, the temporal information of the particles forming the tracked markers is collapsed into one cycle and non-dimensionalised in an analogous way as for the flow particles. At this point, a preliminary phase average of the displacements takes place for each marker separately. This is done operating a sliding regression of a second order polynomial over the phases of the cycle. It should be noticed that the regression is applied in the non-dimensional time obtained from the previous operation, thus making use of the positional information of multiple physical gust cycles. The employed polynomial functions read:

$$\begin{cases} x = a_0 + a_1\, t/T_{ref} + a_2 \left(t/T_{ref}\right)^2 \\ y = b_0 + b_1\, t/T_{ref} + b_2 \left(t/T_{ref}\right)^2 \\ z = c_0 + c_1\, t/T_{ref} + c_2 \left(t/T_{ref}\right)^2, \end{cases} \tag{5.20}$$

where (x, y, z) are the marker's coordinates at the phase t/T_{ref} and a_i, b_i, c_i are the coefficients found by the regression. A non-dimensional time kernel of 1/4 is used because of the good performance compared to other time kernel shown in Section 6.1.

Once the preliminary phase average is completed, it is necessary to identify corresponding markers among different acquisitions. This is done by considering phase-averaged markers having a mean relative distance along the cycle smaller than the search radius r_s. The non-phase-averaged information of such markers is merged and a final phase average takes place employing the same technique mentioned earlier. The standard deviation of the phase-averaged coordinates is calculated comparing the real position of the particles taking part to the regression with the predicted position of the polynomial function:

$$\begin{cases} \sigma_x = \sqrt{\dfrac{1}{N_p - 1} \sum_{n=1}^{N_p} \left(x_n - x\left(t_n/T_{ref}\right)\right)^2} \\ \sigma_y = \sqrt{\dfrac{1}{N_p - 1} \sum_{n=1}^{N_p} \left(y_n - y\left(t_n/T_{ref}\right)\right)^2} \\ \sigma_z = \sqrt{\dfrac{1}{N_p - 1} \sum_{n=1}^{N_p} \left(z_n - z\left(t_n/T_{ref}\right)\right)^2}, \end{cases} \tag{5.21}$$

where N_p is the number of particles participating to the regression, (x_n, y_n, z_n) are the coordinates of the n-

Table 5.3: STB parameters used to process structure images.

General	
X interval [mm]	[−199.847, 200.089]
Y interval [mm]	[−250.089, 249.957]
Z interval [mm]	[100.110, 449.991]
Threshold for 2D particle detection [counts]	16
Allowed triangulation error [vox]	1.50
Shaking	
Outer loop iterations	8
Inner loop iterations	8
Particle position shaking [vox]	0.05
Remove particles closer than [vox]	17.50
Remove particles less intense than fraction of average intensity	0.10
Particle image shape and intensity	
Make OTF smaller	0.50
Increase in particle intensity for residuum computation	2.00
OTF radius for residuum computation	Automatic
Tracking	
Minimum track length	4
X velocity limit [vox]	±4.75
Y velocity limit [vox]	±1.13
Z velocity limit [vox]	±6.36
Max absolute change in particle shift [vox]	2.00
Max relative change in particle shift [%]	20.00
Median filter	Off

th particle and t_n / T_{ref} is its corresponding non-dimensional time. Furthermore, the employed polynomials offer the possibility to easily obtain the structural velocities and accelerations by means of time derivation of (5.20).

The processing operations of the structure images are summarized in Figure 5.8. The Eulerian description of the flow and the Lagrangian description of the structure are already mapped to a common global reference system, since the results of STB processing are obtained in the wind-tunnel reference frame. For the visualization of the FSI phenomenon, both flow and structure phase-averaged results are manipulated in order to obtain a suitable format for the software TECPLOT. The volumetric flow data is transformed in so-called *cubes*, while a triangulation is performed with the position of the markers and so-called *finite element surfaces* are generated.

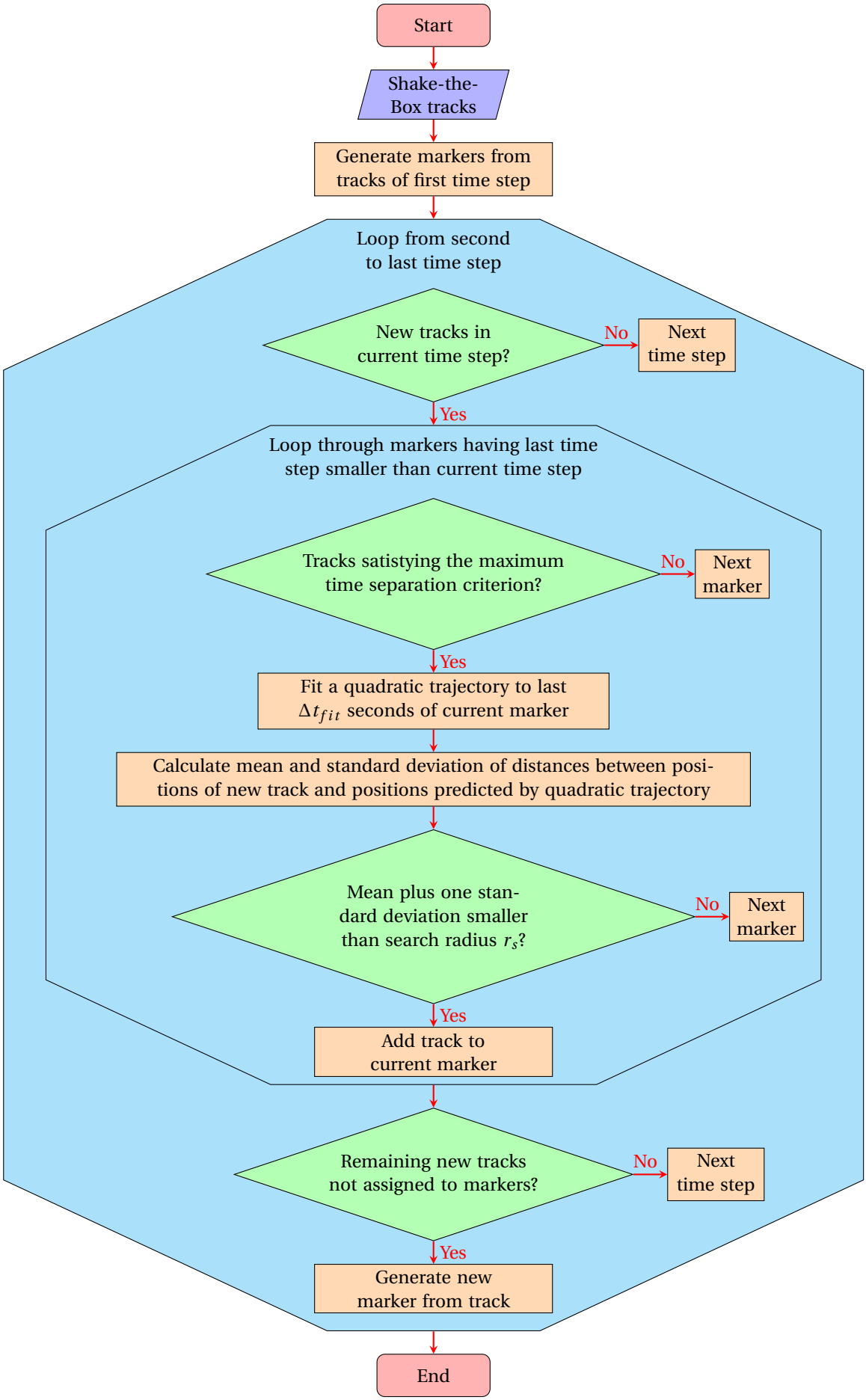

Figure 5.7: Flow chart of the algorithm employed to assemble structural markers joining the tracks obtained from STB.

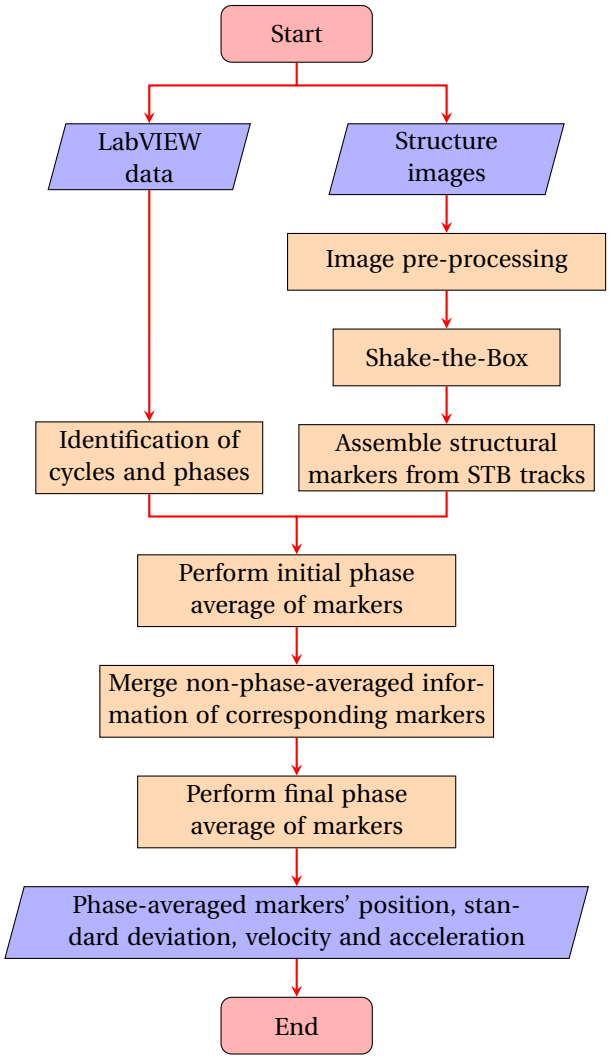

Figure 5.8: Flow chart of the processing strategy employed for the separated structure images.

5.2. Scanning Vibrometer data analysis

The SV data consists in a set of files each containing the time history of the out-of-plane displacement of a single point of the plate. For the comparison with the instantaneous displacement measured by the PIV system it is necessary to account for a potential time offset with respect to the initial PIV recording time, since the two systems acquire data at different frequencies. Such time offset is smaller than 10^{-3} s and an exemplifying illustration is given in Figure 5.9. For each recording the time offset is identified and corrected for.

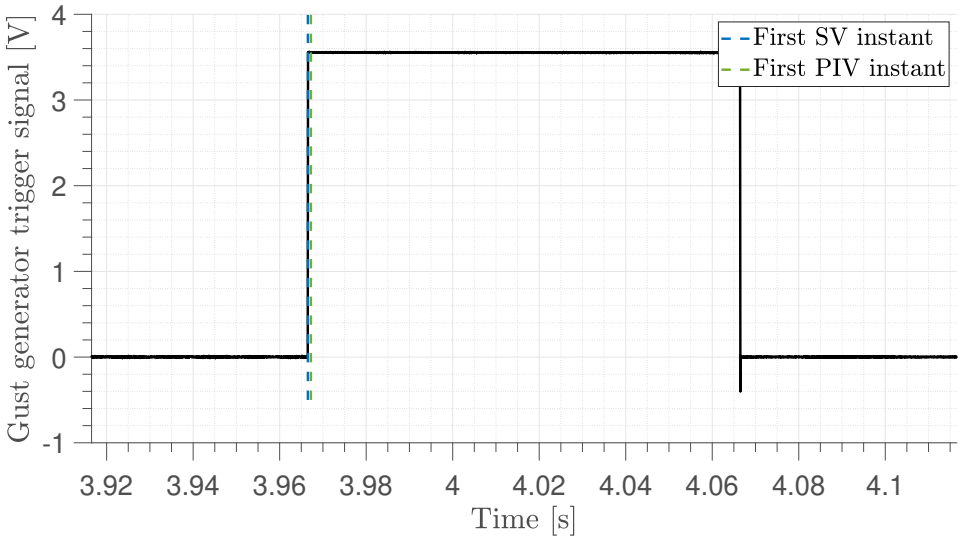

Figure 5.9: Illustration of the offset between the instants of first SV and PIV acquisitions.

The phase average of SV displacements is carried out by identifying the cycles and the phases within each acquisition in an analogous way as described for the PIV data. Also the collapse of the temporal information into one cycle and its non-dimensionalization is achieved similarly. Finally, the phase-averaged displacements are calculated using the same polynomial regression as explained for the PIV data.

6

Results

In this chapter, the results obtained analysing the experimental data as described in Chapter 5 are presented. These results provide the basis to answer the research questions formulated in Section 3.2. First, a validation of the instantaneous structural measurements performed with the Robotic Volumetric PIV system is carried out in Section 6.1. Later, in Section 6.2 the validity of the phase-average approach employed for both structure and flow is discussed. Another important aspect of the research questions is the consistency between flow and structure, which is assessed in Section 6.3. Finally, a visualization of the FSI phenomenon is given in Section 6.4, together with a quantitative analysis of its dynamics.

Contents

6.1. Validation of instantaneous structural measurements

The validation of the instantaneous structural measurements is initially carried out on the displacements obtained from the PIV-SV measurement set (see Table 4.3). Three markers along the span of the plate are selected and measured one at a time by the synchronized Robotic Volumetric PIV and SV systems. All markers are located at the centre of the chord and their position along the span is indicated in Figure 6.1.

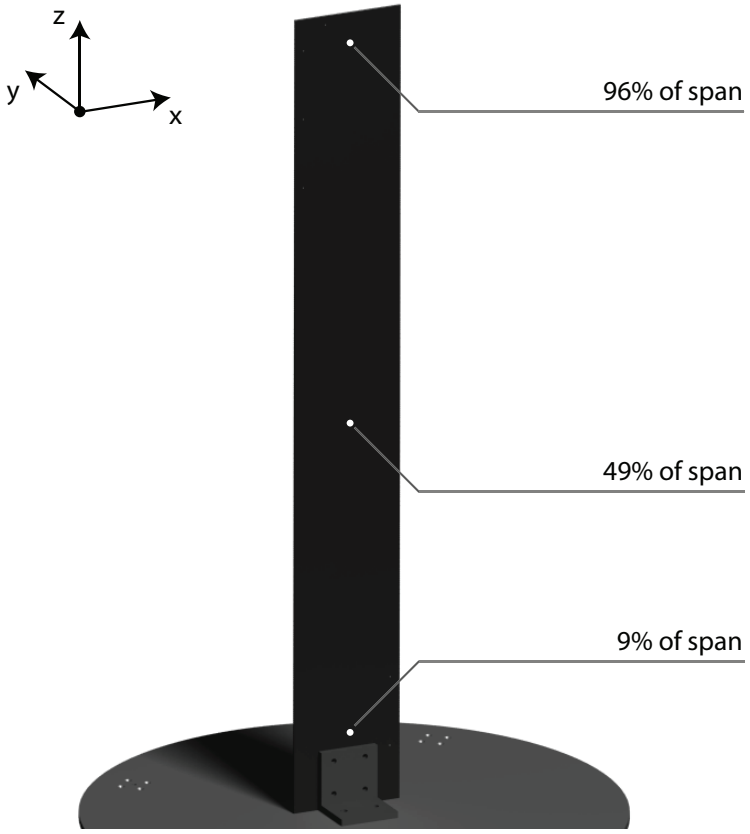

Figure 6.1: Position of the markers selected for the validation of the instantaneous structural measurements. Markers not to scale.

Midspan marker

The first marker considered for the validation, is the one located halfway along the span, more precisely at 49% of the span. Figure 6.2 shows the comparison between the instantaneous displacements measured by the Robotic Volumetric PIV and the SV systems. The displacement shown in the plot is the one along the y-axis of the PIV reference frame (see Figure 4.10 and 4.11), corresponding to the out-of-plane displacement measured by the SV. The analysed displacement is relative to the the first detected position of the marker. The reference measurement (SV) exhibits a sinusoidal evolution with an amplitude around 30 mm and a frequency approximately equal to the actuation frequency of the gust generator, that is to say 0.9 Hz. This frequency is expected because the sinusoidal gust field acts as an harmonic forcing on the plate and as a consequence the resulting response of the plate has the same frequency as the excitation. Obviously, this is true for all the markers analysed in this section.

The bias error $\epsilon_{b,\Delta y}$ and the random error $\epsilon_{r,\Delta y}$ of the PIV measurement with respect to the SV measurement are respectively calculated as the mean and the standard deviation of the difference between the PIV and the SV curves. For the calculation of such difference the SV data is linearly interpolated to the PIV time instants. The values resulting from 20 gust cycles are $\epsilon_{b,\Delta y} \approx -0.092$ mm and $\epsilon_{r,\Delta y} \approx 0.383$ mm, respectively corresponding to the 0.3% and the 1.3% of the average displacement amplitude.

The PIV results shown in Figure 6.2 are raw results, meaning that they are obtained from the particle positions returned by the STB algorithm. As explained in Section 3.1.1, the particles' velocity is estimated fitting a polynomial of second or higher order to the particles' trajectory, realizing in this way the concept

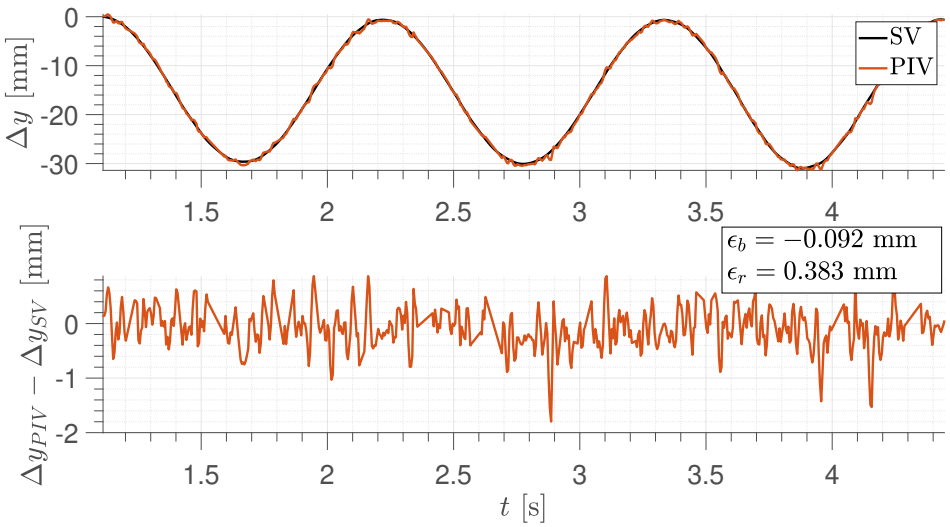

Figure 6.2: Time history of the instantaneous displacement measured by Robotic Volumetric PIV and SV for the midspan marker (top) and of the related error (bottom). Only results from 3 gust cycles are shown.

of track regularization. The same technique can be applied here to regularize the positional information, assessing in this way whether a reduction of the displacement errors of the PIV measurement is possible. For such purpose, a sliding least square regression is applied to the raw PIV displacements. Different time kernels are investigated, together with two polynomial orders, second and third.

A comparison among the results of some selected combinations of time kernels and polynomial orders is shown in Figure 6.3. It can be observed how the curves resulting from the use of a second order polynomial and a kernel of $1/8$ of the nominal gust period T_{gust}, from the use of a third order polynomial and a kernel of $T_{gust}/4$ and from the use of a second order polynomial and a kernel of $T_{gust}/4$ of the gust period lie on top of each other and on top of the SV curve. This means that there is no substantial difference in using a third or second order polynomial for the regression and in using $1/8$ or $1/4$ of gust period as kernel. Also the curve resulting from the use of a second order polynomial and a kernel of $T_{gust}/2$ is almost completely on top of the other curves, indicating that even employing such a large time kernel no significant modulation of the measured signal can be noticed. This however changes when considering a kernel of 1 gust period, with the resulting curve presenting a substantial modulation with respect to the reference measurement.

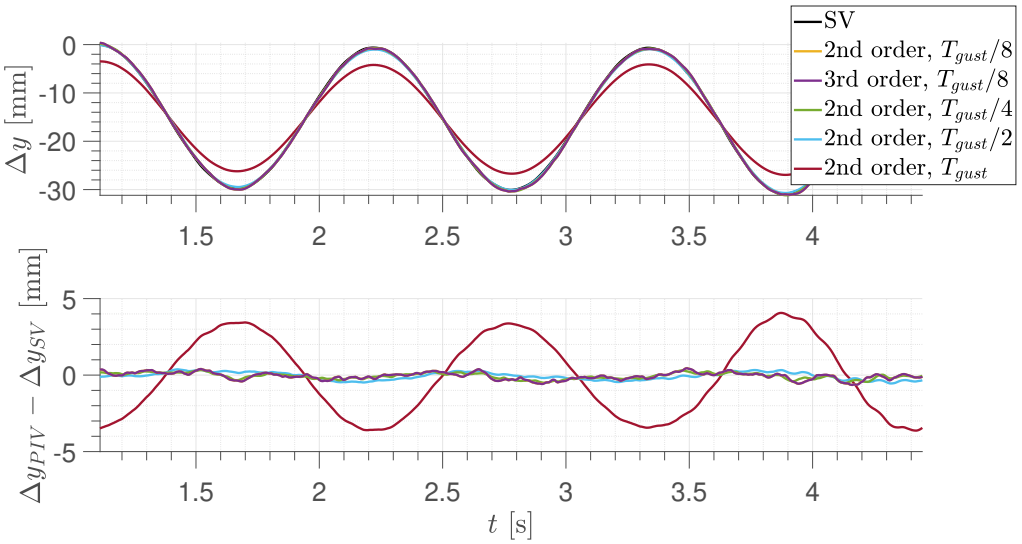

Figure 6.3: Time history of the instantaneous displacement obtained with different least square regressions on Robotic Volumetric PIV data for the midspan marker. Comparison with SV measurement (top) and related error (bottom). Only results from 3 gust cycles are shown.

The results in terms of bias and random errors are summarized in Table 6.1 [1]. Up to a kernel of 1/4 of the gust period, the bias error increases slightly while the random error decreases substantially [2]. For a kernel of $T_{gust}/2$ also for the bias error a reduction is observed, even if small, while for a kernel of 1 gust period both bias error and random error see a strong increase. However, the best performance in terms of random error is obtained with a second order polynomial and a kernel of 1/4 of the gust period, resulting in $\epsilon_{b,\Delta y} \approx -0.096$ mm and $\epsilon_{r,\Delta y} \approx 0.201$ mm, respectively 0.3% and 0.7% of the average displacement amplitude.

Table 6.1: Results of polynomial least square regression on raw PIV measurement.

	2nd order				3rd order			
Temporal kernel	ϵ_b [mm]	Δ_{ϵ_b} [%]	ϵ_r [mm]	Δ_{ϵ_r} [%]	ϵ_b [mm]	Δ_{ϵ_b} [%]	ϵ_r [mm]	Δ_{ϵ_r} [%]
$T_{gust}/8$	-0.096	+5.0	0.248	-35.2	-0.096	+5.0	0.249	-35.0
$T_{gust}/4$	-0.096	+4.4	0.201	-47.4	-0.096	+4.3	0.205	-46.5
$T_{gust}/2$	-0.091	-0.9	0.214	-44.0	-0.091	-1.1	0.225	-41.4
T_{gust}	-0.123	+34.1	2.522	+558.8	-0.123	+34.6	2.524	+559.2

Since inertia forces depend on accelerations, it is important to evaluate the related measurement performance of the Robotic Volumetric PIV system. First, the instantaneous velocity of the marker is calculated from the displacement data of both systems employing a sliding least square regression. Based on the previous results, a second order polynomial and a kernel of 1/4 of the gust period are used. The polynomial is derived in time and the velocity is evaluated at the desired time instant. The comparison between Robotic Volumetric PIV and SV results is shown in Figure 6.4, together with their difference. Both curves appear smooth and the one of PIV is in very good agreement with the one of SV. The resulting bias and random errors are respectively $\epsilon_{b,\dot{y}} \approx -0.014$ mm/s^2 and $\epsilon_{r,\dot{y}} \approx 1.179$ mm/s^2, corresponding to 0.008% and 0.7% of the velocity amplitude (approximately 180 mm/s).

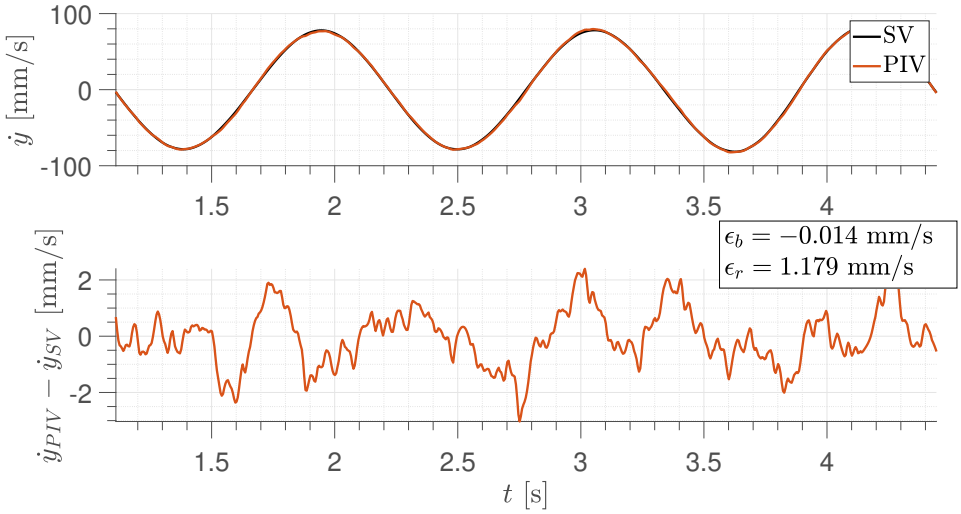

Figure 6.4: Time history of the instantaneous velocity measured obtained from Robotic Volumetric PIV and SV measurements for the midspan marker (top) and of the related error (bottom). Only results from 3 gust cycles are shown.

For the calculation of the accelerations, the polynomials obtained with the sliding least regression are derived twice in time. The accelerations calculated from Robotic Volumetric PIV and SV measurements are

[1] All bias and random errors obtained from least square regression curves are calculated excluding the initial and final part of the signal, so that both mean and standard deviation are not affected by the side effects of the regression. The exclusion intervals at both the start and the end of the signal are equal to half regression kernel.

[2] The percentage difference of the errors is calculated as $\left(\epsilon_{polyfit} - \epsilon_{raw}\right)/\epsilon_{raw} \cdot 100$. In this way when the absolute value of the initial quantity increases, a positive percentage difference is obtained, as in the case of the bias error for a time kernel of $T_{gust}/8$, $T_{gust}/4$ and T_{gust}.

compared in Figure 6.5. It can be noticed how in this case the PIV curve appears noisier with respect to what was obtained for the velocity. The bias error results to be 0.169 mm/s^2, corresponding to 0.02% of the acceleration amplitude (approximately 1100 mm/s^2), and the random error amounts to 28.807 mm/s^2, that is to say 2.6% of the acceleration amplitude.

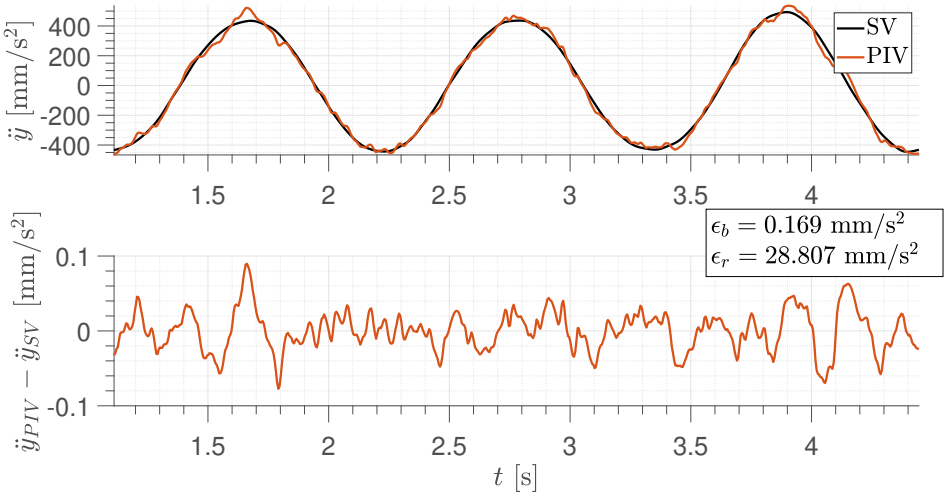

Figure 6.5: Time history of the instantaneous acceleration obtained from Robotic Volumetric PIV and SV measurements for the midspan marker (top) and of the related error (bottom). Only results from 3 gust cycles are shown.

Tip marker

For the evaluation of displacements, velocities and accelerations of the remaining markers, a sliding second order polynomial regression with a time kernel of 1/4 of the gust period is used, based on the results of the midspan marker. As far as the tip marker is concerned, the comparison between PIV and SV displacements, velocities and accelerations is shown in Figures 6.6, 6.7 and 6.8, respectively. The displacement of the tip marker exhibits a larger amplitude with respect to the midspan marker, approximately equal to 90 mm. The bias and random error of the displacements amount to 0.144 mm and 0.721 mm, respectively, thus resulting larger than what obtained for the midspan marker. The increase in random error can be ascribed to the larger uncertainty in the particle position caused in turn by the larger displacement of the tip marker and thus by a smaller tomographic angle when the marker is relatively far from the CVV probe. However, when the average amplitude of the displacement is considered, the bias and random errors amount to 0.2% and 0.8%. The larger random error of the displacements with respect to the midspan marker translates into a larger random error of velocities and accelerations as well. Once again though, when the average amplitude of velocity and acceleration is considered, the respective random errors amount to 0.8% and 2.5%, thus resulting small in relative terms. The bias errors instead are not substantially larger in absolute value with respect to the bias errors obtained for the midspan marker.

Root marker

The displacements, velocities and accelerations resulting from the marker at the root are shown in Figures 6.9, 6.10 and 6.11, respectively. The displacements measured by the SV exhibit an amplitude of approximately 0.85 mm, thus more than one order of magnitude lower of both the midspan and the tip markers. From the plots it is evident how the curves calculated from the PIV measurement are very noisy and fail to reproduce the signals measured by the SV. The reason for this can be found in the displacement plot, where it can be observed from the SV curve that the amplitude of the signal is less than 1 mm. As mentioned in Section 3.1.1, a typical particle positional error that can be expected for a CVV system along the imaging direction is in the order of 1 mm. Given the position of the CVV probe used for the present investigation, a large part of the plate motion is indeed along the imaging direction. As a consequence the PIV measurement cannot resolve the motion of the root marker, being the displacement amplitude in the same order of the particle positional uncertainty.

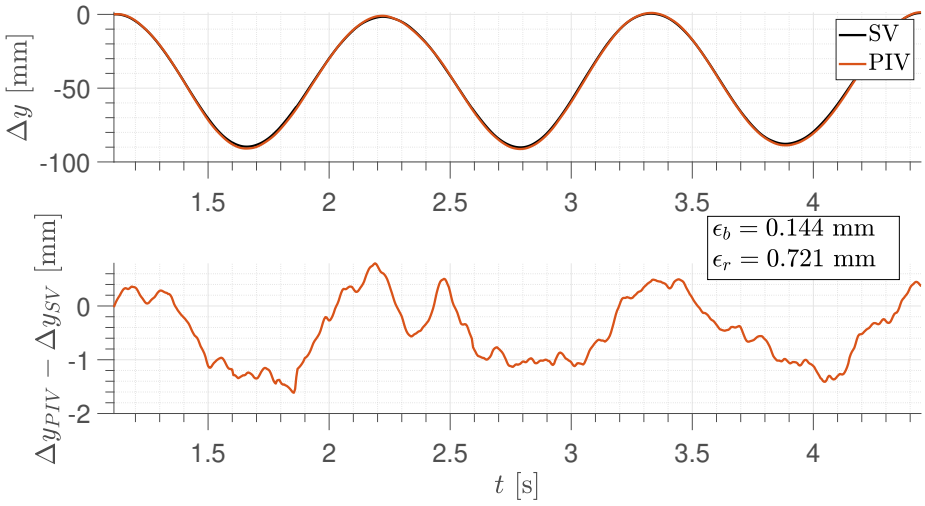

Figure 6.6: Time history of the instantaneous displacement obtained from Robotic Volumetric PIV and SV measurements for the tip marker (top) and of the related error (bottom). Only results from 3 gust cycles are shown.

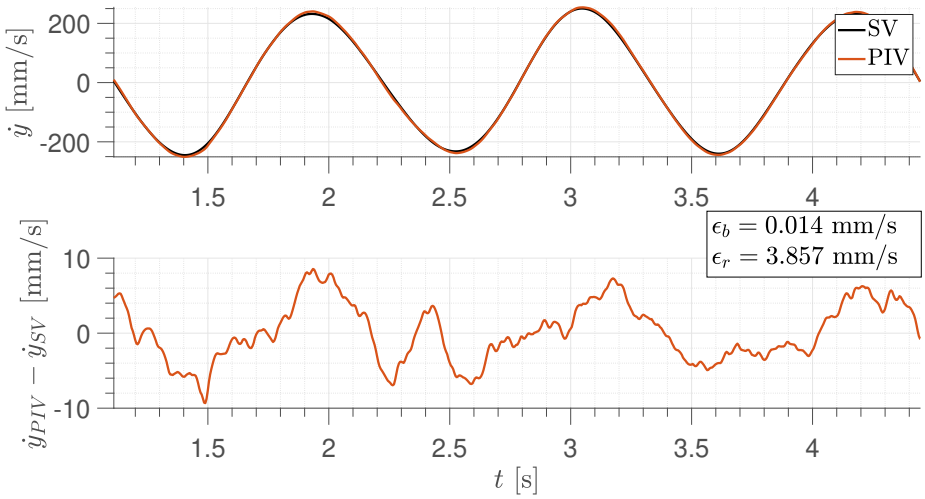

Figure 6.7: Time history of the instantaneous velocity obtained from Robotic Volumetric PIV and SV measurements for the tip marker (top) and of the related error (bottom). Only results from 3 gust cycles are shown.

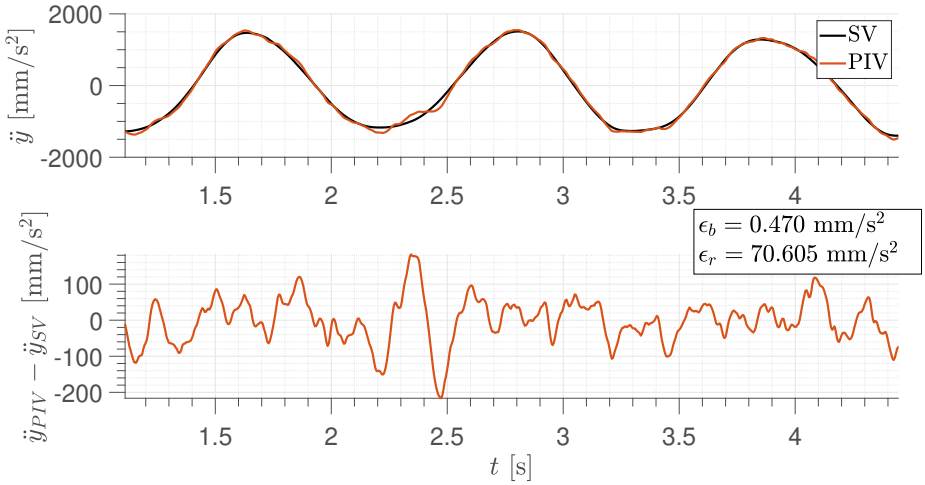

Figure 6.8: Time history of the instantaneous acceleration obtained from Robotic Volumetric PIV and SV measurements for the tip marker (top) and of the related error (bottom). Only results from 3 gust cycles are shown.

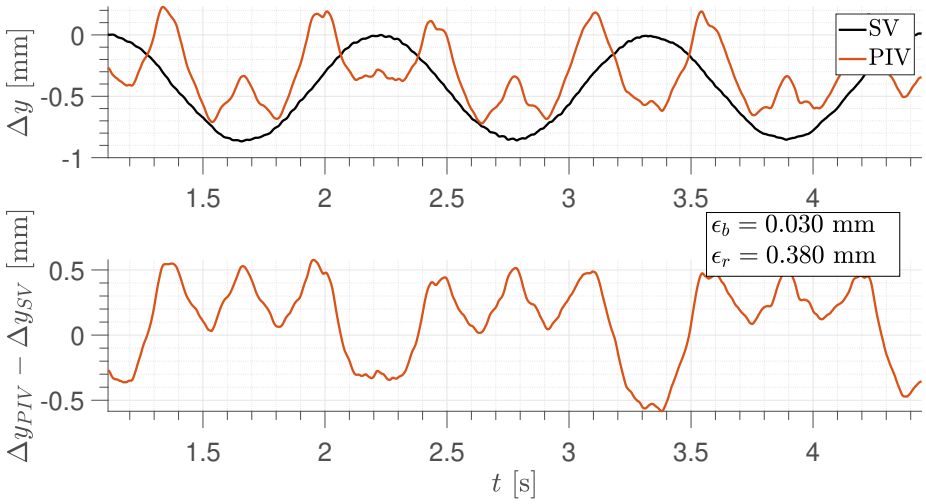

Figure 6.9: Time history of the instantaneous displacement obtained from Robotic Volumetric PIV and SV measurements for the root marker (top) and of the related error (bottom). Only results from 3 gust cycles are shown.

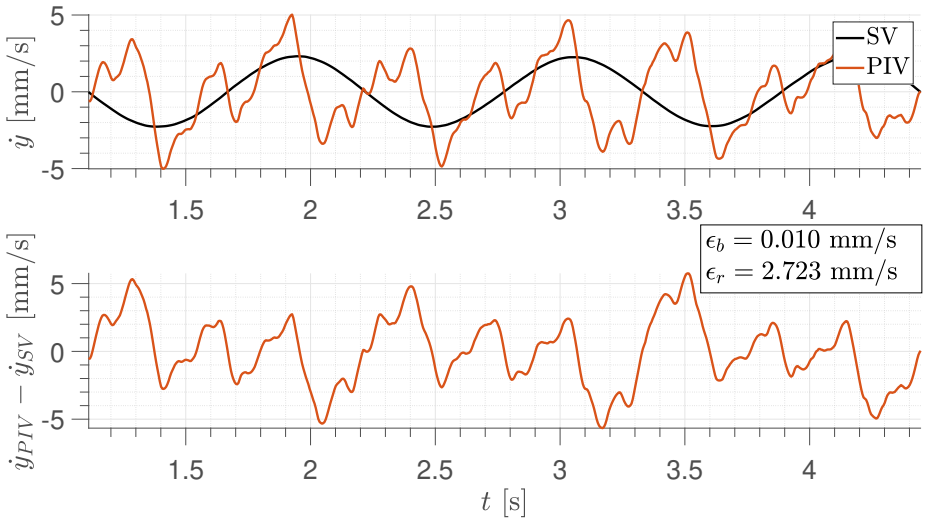

Figure 6.10: Time history of the instantaneous velocity obtained from Robotic Volumetric PIV and SV measurements for the root marker (top) and of the related error (bottom). Only results from 3 gust cycles are shown.

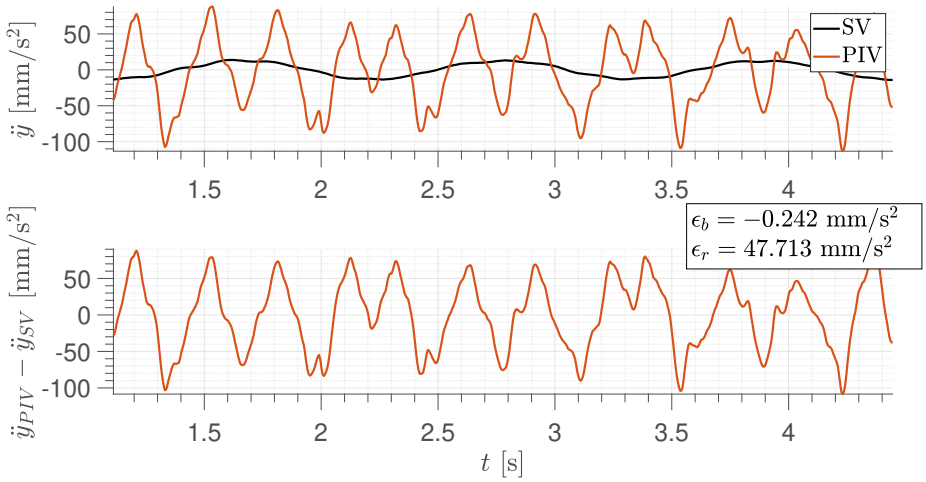

Figure 6.11: Time history of the instantaneous acceleration obtained from Robotic Volumetric PIV and SV measurements for the root marker (top) and of the related error (bottom). Only results from 3 gust cycles are shown.

6.2. Phase-average approach

As mentioned in Section 5.1, a phase-average approach is used to join structure and flow results of different measurement cones. As far as the structural displacements are concerned, the phase-average approach is firstly assessed for a single marker and then for a set of markers belonging to two different measurement cones. Regarding the flow, several ensemble averaging methods are evaluated, analysing for each the standard deviation of the velocity together with the related uncertainty.

6.2.1. Structural displacements

Single marker

The step following the validation of instantaneous displacements of a single marker concerns the assessment of its phase-averaged displacements. For this aim, the scatter in the structural displacements from one cycle to the other is evaluated here. Three different kinds of measurement are compared: SV without HFSB, PIV without HFSB and PIV with HFSB. The midspan marker previously considered in Section 6.1 is used here to obtain the phase-averaged displacements over 20 cycles. The results are shown in Figure 6.12, where the scatter among the different cycles is indicated by means of error bars representing one standard deviation of the displacements for each phase.

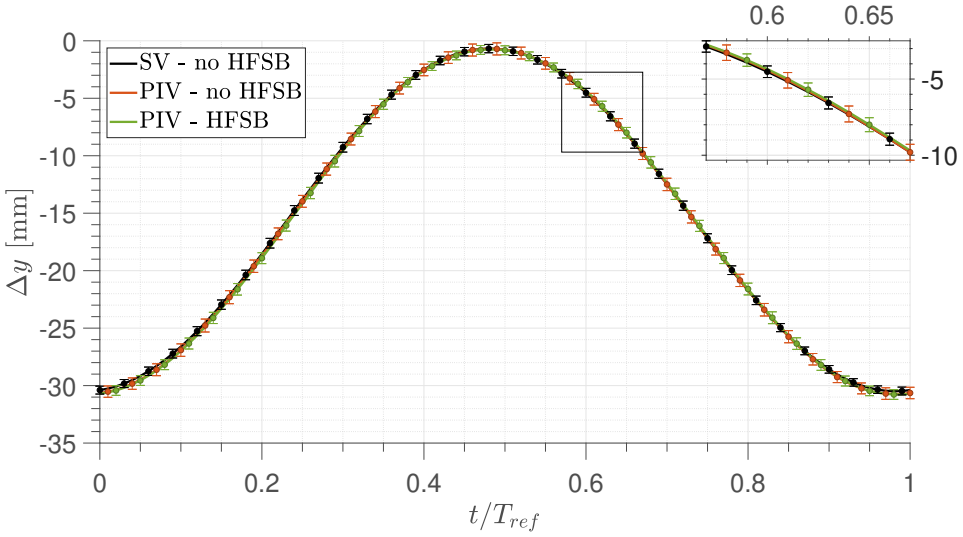

Figure 6.12: Phase-averaged structural displacements of the central midspan marker. The error bars represent one standard deviation.

The mean and maximum standard deviation over the average cycle are summarized in Table 6.2, together with the bias and random error of the PIV curves with respect to the SV curve. It can be noticed that the smallest value for both mean and maximum standard deviation is obtained from the SV measurement, amounting respectively to 1.3% and 1.4% of the displacement amplitude (approximately 30 mm). This can be explained considering that the standard deviation of each phase results from the contribution of two components: the scatter from one gust to the other and the random error of the measurement system. In fact, if the random error related to the SV system is considered negligible, because of the high measurement resolution reported by the manufacturer, then the standard deviation resulting from the SV measurement can be mainly attributed to the scatter among the gusts generated in the different cycles. The larger standard deviation obtained for the PIV-no HFSB and the PIV-HFSB includes a non-negligible contribution given by the random error of the Robotic Volumetric PIV system. Furthermore, considering the comparable values of the mean and maximum standard deviation of the measurements with and without HFSB, it can be inferred that the introduction of flow particles does not compromise the structural measurement performed with the Robotic Volumetric PIV system. Finally, both the bias and random error of the phase-averaged PIV curves are comparable with the values obtained in Section 6.1.

The phase-averaged velocities and acceleration of the midspan marker are also evaluated and the results are shown in Figure 6.13 and 6.14, respectively. Similarly to what was observed for the instantaneous comparison, the PIV velocity curves appear smooth and in very good agreement with the SV curve, while the PIV acceleration curves contain a noticeable noise. The bias and random errors with respect to the phase-averaged

Table 6.2: Mean and maximum standard deviation of the phase-averaged displacements of the midspan marker, together with bias and random error of the PIV curves with respect to the SV curve.

Measurement	$\overline{\sigma_{\Delta y}}$ [mm]	$\sigma_{\Delta y,max}$ [mm]	$\epsilon_{b,\Delta y}$ [mm]	$\epsilon_{r,\Delta y}$ [mm]
SV-no HFSB	0.379	0.427	-	-
PIV-no HFSB	0.518	0.575	-0.103	0.122
PIV-HFSB	0.450	0.524	-0.128	0.201

SV curve are summarized in Table 6.3, where it can be observed that in most of the cases the obtained values are comparable with the ones of Section 6.1 (except for the bias error of the PIV-no HFSB acceleration, which here results one order of magnitude larger, but still amounting only to 0.4% of the acceleration amplitude).

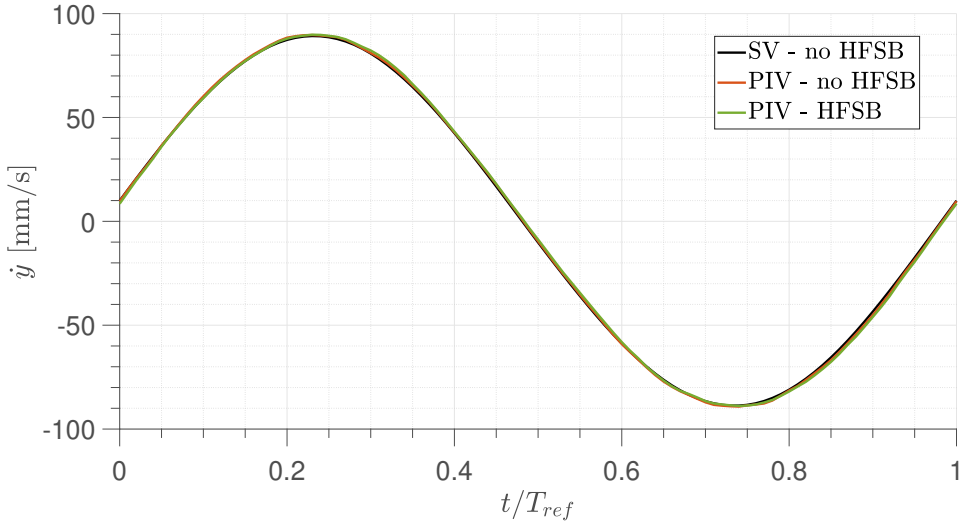

Figure 6.13: Phase-averaged structural velocities of the central midspan marker.

Table 6.3: Bias and random error of the phase-averaged PIV velocities and accelerations with respect to the phase-averaged SV curves for the midspan marker.

Measurement	$\epsilon_{b,\dot{y}}$ [mm/s]	$\epsilon_{r,\dot{y}}$ [mm/s]	$\epsilon_{b,\ddot{y}}$ [mm/s^2]	$\epsilon_{r,\ddot{y}}$ [mm/s^2]
PIV-no HFSB	-0.005	0.734	4.905	15.714
PIV-HFSB	-0.015	1.252	0.037	18.203

Multiple markers

Once the validity of the phase-averaged displacements of a single marker has been verified, the results related to multiple markers can be assessed. In fact, the structural measurement of the entire flexible plate relies on tracking multiple markers at the same time within a single acquisition and on joining together the results of different acquisitions. For this reason it is important to evaluate the physical consistency among markers belonging to the same and to different PIV volumes. This consistency is assessed comparing the position of the phase-averaged markers with a physical model fitted to the same phase-averaged markers.

The employed model has a time-dependent component describing the temporal evolution during the average cycle and a spatial component describing the deformation shape of the flexible plate in the three-dimensional space. The temporal component consists in a sine wave, while the spatial part is formed by a weighted sum of the first three natural vibration shape, corresponding to the first and second bending mode and to the first torsional mode of the plate. The evolution of the structural coordinates during the average

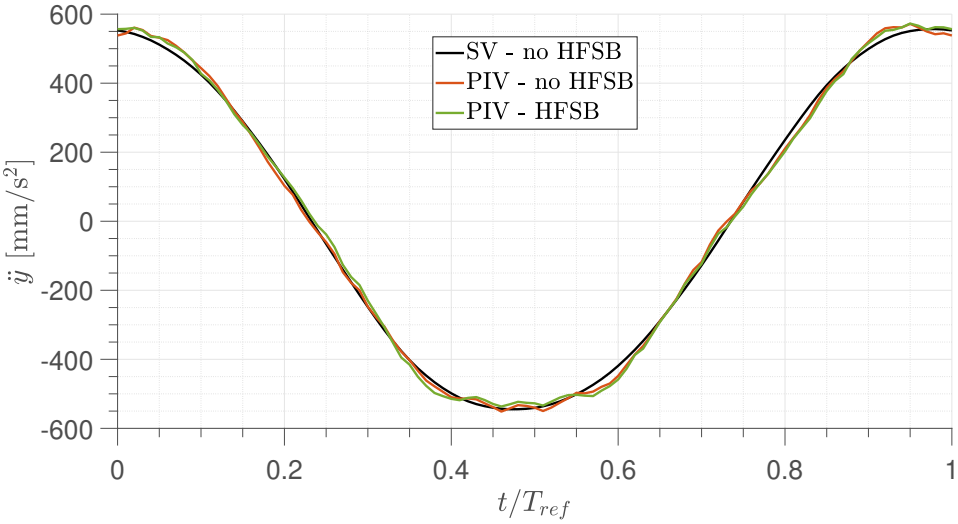

Figure 6.14: Phase-averaged structural accelerations of the central midspan marker.

cycle is described as it follows:

$$\begin{cases} x_i = \sin\left(2\pi t/T + \varphi\right)\left(A\Delta x_{e_1,i} + B\Delta x_{e_2,i} + C\Delta x_{e_3,i}\right) + x_{s,i} \\ y_i = \sin\left(2\pi t/T + \varphi\right)\left(A\Delta y_{e_1,i} + B\Delta y_{e_2,i} + C\Delta y_{e_3,i}\right) + y_{s,i} \\ z_i = \sin\left(2\pi t/T + \varphi\right)\left(A\Delta z_{e_1,i} + B\Delta z_{e_2,i} + C\Delta z_{e_3,i}\right) + z_{s,i}, \end{cases} \tag{6.1}$$

where $[x_i, y_i, z_i]$ are the coordinates of the i-th point of the model at the non-dimensional time t/T of the average cycle, $[\Delta x_{e_j,i}, \Delta y_{e_j,i}, \Delta z_{e_j,i}]$ is the displacement vector corresponding to the j-th vibration mode of the plate at the i-th point and $[x_{s,i}, y_{s,i}, z_{s,i}]$ are the coordinates of the i-th point in the static condition. A, B and C are the weights of the different vibration modes and φ is the phase of the sine wave used in the physical model.

A least square regression is performed on the phase-averaged coordinates of the markers to find the parameters A, B, C and φ. The following steps are employed for such aim. A structural model of the plate is generated with the commercial software MSC NASTRAN using CQUAD4 shell elements. The coordinates of the model's points in the static conditions $[x_{s,i}, y_{s,i}, z_{s,i}]$ are found by means of a three-dimensional translation and rotation of the NASTRAN structural nodes. The translation and rotation vectors are found by means of an optimization that minimizes the summation of the squared distance between the markers of the entire plate and the surface obtained from the triangulation of the NASTRAN structural nodes. For this operation the markers measured with a static inflow velocity of 11 m/s (no gust) are considered. The distance of each marker from the NASTRAN surface is calculated by means of the MATLAB function `point2trimesh` [3]. The displacement vector corresponding to the each vibration mode of the plate for each point of the model $[\Delta x_{e_j,i}, \Delta y_{e_j,i}, \Delta z_{e_j,i}]$ is found running a modal analysis of the NASTRAN model (SOL 103). The parameters A, B, C and φ are found minimizing the the summation of the squared distance between the measured markers and the surface obtained by the triangulation of the points obtained with equation (6.1). Two PIV volumes belonging to the PIV-SV measurement set are used for this assessment, that is to say the ones including the midspan and the tip marker analysed in Section 6.1. An illustration of the measured markers and of the surface resulting from the regression of the physical model is given in Figure 6.15.

Once the parameters A, B, C and φ are found, it is possible to evaluate the mean distance of the markers from the surface given by the physical model during the average cycle. The results of this assessment are shown in Figure 6.16, where also the standard deviation of the markers' distance is displayed. The sign convention of the markers' distance of from the fitted surface is consistent with the orientation of the y axis of the measurement reference frame (a positive distance indicates a marker "behind" the fitted surface observed in Figure 6.15 and a negative distance indicates a marker "in front" of such fitted surface). The plot is provided as

[3] `https://uk.mathworks.com/matlabcentral/fileexchange/52882-point2trimesh-distance-between-point-and-triangulated-surface`.

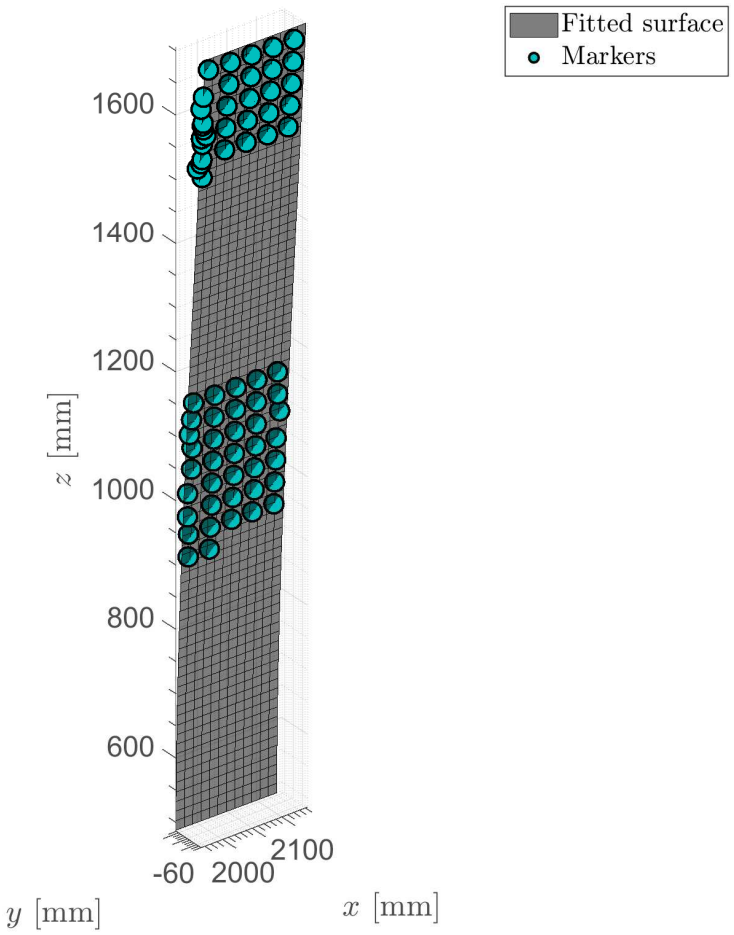

Figure 6.15: Phase-averaged markers and fitted surface for $t/T_{ref} = 0$.

well with an upper x-axis, showing the tip displacement of the plate at the different non-dimensional time instants of the average cycle. The phase-averaged tip displacement is calculated taking the difference between the mean phase-averaged y position of the top 5 markers and the mean y position of the same markers in their static condition (wind-tunnel speed of 11 m/s with no gust). The resulting displacement is shown in Figure 6.17, where the largest positive value indicates the furthest position of the plate's tip from the CVV probe and the largest negative value indicates the closest position to the probe.

Regarding the midspan markers, the curves of both mean distance and standard deviation appear relatively flat during the average cycle. As far as the tip markers are concerned, the curves show more variation during the average cycle, however the mean and standard deviation values are in absolute value of the same order of magnitude with respect to the ones of the midspan markers. On average, the midspan markers have a distance of 2.1 ± 1.2 mm from the fitted surface, while the tip markers have a distance of -1.3 ± 1.7 mm. This means that the midspan markers are on average behind the fitted surface and the tip markers are in front of it, when looking from the perspective of Figure 6.15. Furthermore, the evolution of the mean distance curves does not show an evident correlation with the tip displacement and thus with the distance of the markers from the CVV probe, thus implying that the larger positional uncertainty at larger distances does not compromise the structural consistency of the tracked markers. In conclusion, considering the largest mean distance of the two groups of markers in absolute value, it can be stated that the measured markers appear to be consistent with the first three vibration modes of the plate within at worst 2.4 mm, corresponding to 2.5% of the tip displacement amplitude.

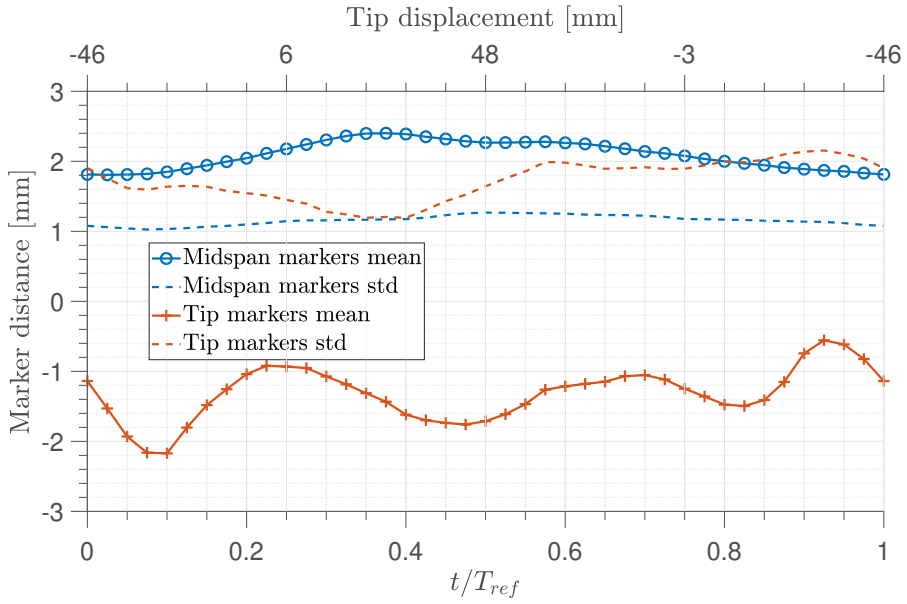

Figure 6.16: Mean and standard deviation of markers' distance from fitted surface during the averaged cycle.

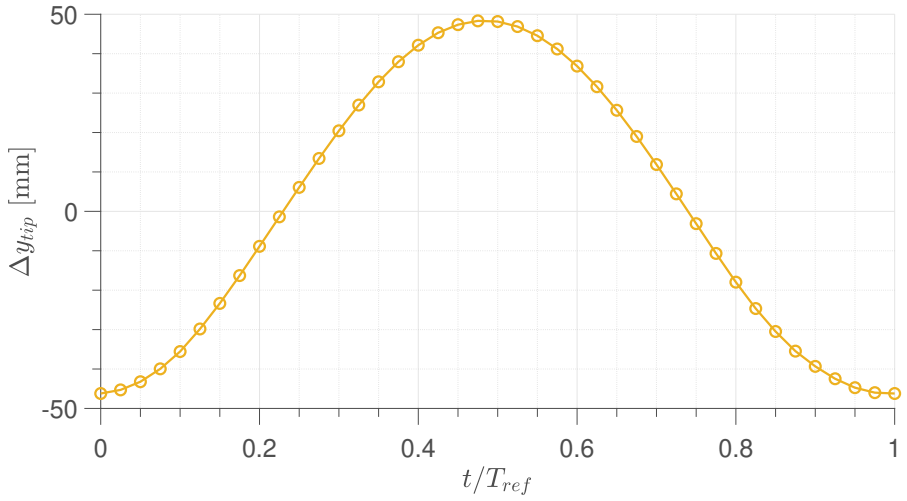

Figure 6.17: Phase-averaged tip displacement for the PIV-SV measurement set.

6.2.2. Flow field

The different techniques discussed in Section 5.1.2 to convert the Lagrangian tracks to an Eulerian description with a phase-average approach are compared here with a discussion of the resulting velocity standard deviation and of the related uncertainty. At first the different ensemble averaging methods are compared using a baseline linear bin size and employing a fixed non-dimensional time window. Afterwards the effect of the spatial bin variation is assessed and finally also the use of the temporal information within temporal bins of different size is discussed. All comparisons are performed considering flow data from the PIV-HFSB measurement set at the phase $t/T_{ref} = 0$ and lying on a plane cutting the plate at its half span, that is to say at $z = 1.096$ m.

A linear bin size of $l_B = 42.5$ mm (1/4 of the plate's chord) is selected to compare the effect of the different ensemble averaging methods employed. Such size is chosen because it is considered a good compromise between spatial resolution and data availability, as it will be discussed later. No temporal information is considered for the present comparison, with the spatial average being carried out considering for each phase an averaging non-dimensional time window of 1/821 (given the nominal gust period of $T_{gust} = 1$ s and the acquisition frequency of 821.7 Hz, this approximately corresponds to one pulse separation time). The minimum number of particles for each valid bin is set to 20 for this analysis, so that the quadratic polynomial fit

can rely on a number of points that is at least double the amount of the number of coefficients to be found.

Figure 6.18 shows the contour of the streamwise velocity component obtained using a top-hat filter, a gaussian filter, a linear polynomial fit and a quadratic polynomial fit. It is possible to recognize the plate position as it prevents the measurement of the flow field on the far side from the CVV probe. Two points of interest can be observed in all the obtained flow fields: a region of accelerated flow towards the plate's leading edge and a region of decelerated flow in the wake of the plate. Not much difference can be observed among the different methods as far as the former is concerned, whereas in the wake it is evident that the quadratic polynomial fit predicts a larger velocity deficit. However, the quadratic polynomial fit is also observed to provide more noisy results, as small unphysical accelerations and decelerations can be detected along some of the streamlines.

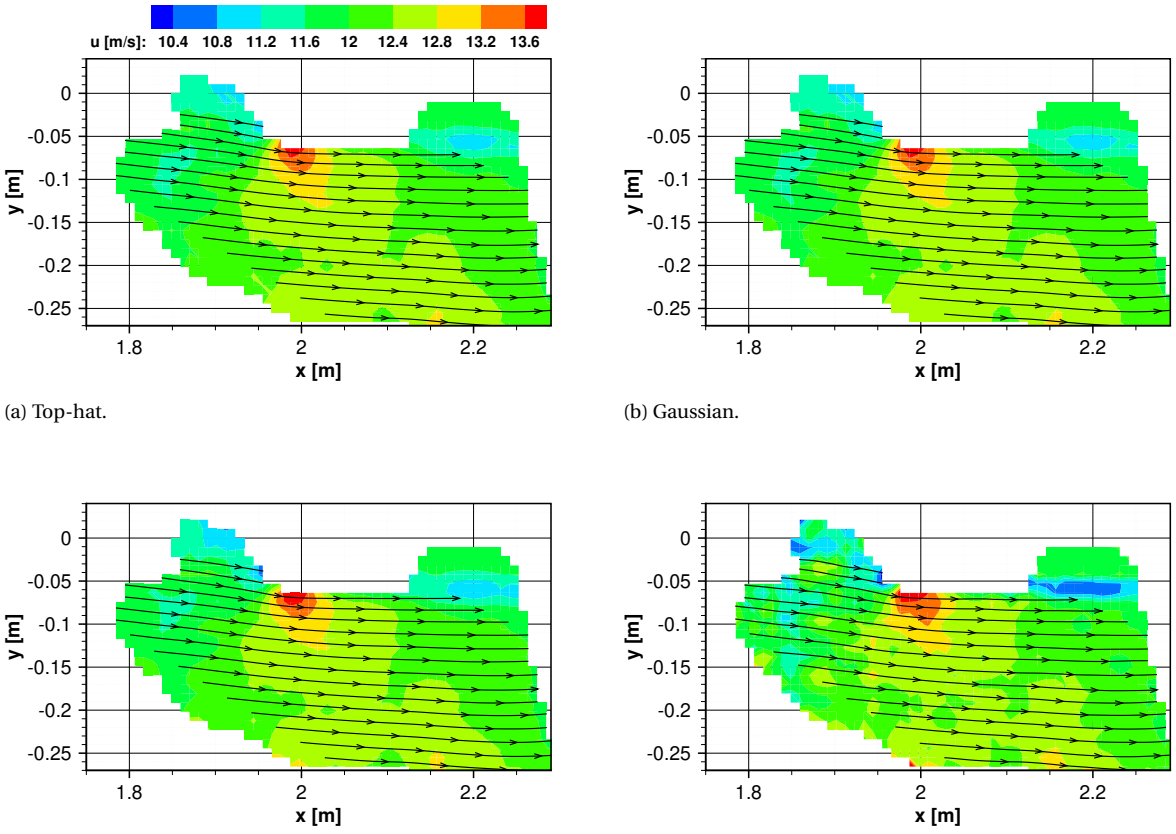

(a) Top-hat.

(b) Gaussian.

(c) Linear.

(d) Quadratic.

Figure 6.18: Comparison of streamwise velocity contour for different ensemble averaging methods, using a linear bin size of l_B = 42.5 mm and an averaging non-dimensional time window of 1/821. Slice cut at 50% of the plate's span.

The contour of the standard deviation of the streamwise velocity is shown in Figure 6.19. For all flow fields the regions with the highest values of standard deviation correspond to the leading edge of the plate, the wake and a part of the flow field upstream of the plate. The relatively large standard deviation in these regions may result from two components: a physical fluctuation of the flow velocity within one gust period or from one gust to the other and the uncertainty of the measurement system. Among other factors, the latter is also influenced by the number of particles used for the ensemble average. In fact, assuming a gaussian distribution of the measured velocity samples in a point in space, a relatively small number of particles results in a relatively large weight of velocity samples distant from the mean value, consequently driving up the standard deviation with respect to a situation with a larger number of available particles. For this reason, the number of particles found in the considered slice is inspected in Figure 6.20, where it can be observed that indeed all the indicated regions have a relatively small number of particles with respect to other parts of the flow field. However, it can be noticed that close to the leading edge of the plate and in the upstream region of the flow field less than 90 particles are available for the ensemble average, while for a portion of the wake up to 120 particles are found. Considering as well that the wake region is likely characterized by a turbulent

flow, the observations on the distribution of the number of particles suggest that the large standard deviation of the upstream region and of the accelerated flow region has to be mainly ascribed to the uncertainty of the measurement system, while the standard deviation in the wake is more influenced by a physical component.

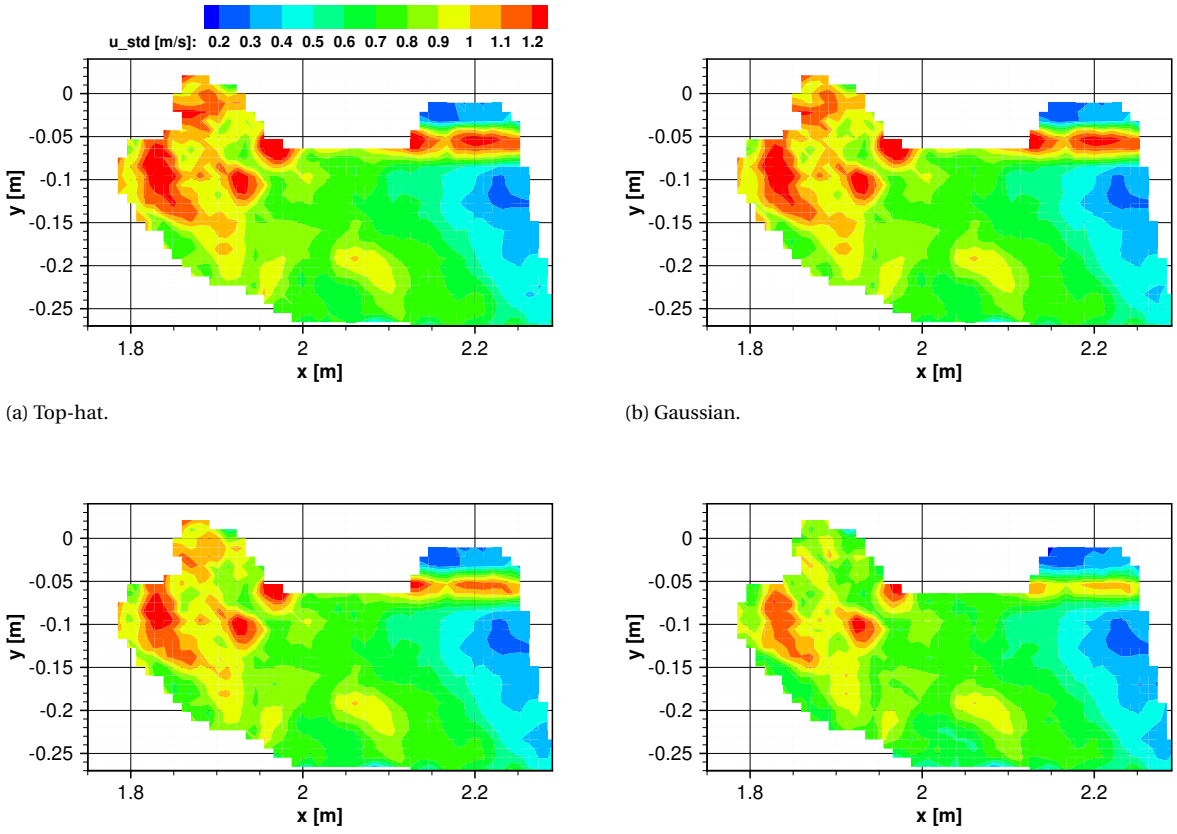

(a) Top-hat.

(b) Gaussian.

(c) Linear.

(d) Quadratic.

Figure 6.19: Comparison of streamwise velocity standard deviation contour for different ensemble averaging methods, using a linear bin size of $l_B = 42.5$ mm and an averaging non-dimensional time window of 1/821. Slice cut at 50% of the plate's span.

Another observation that can be made from Figure 6.19 is that the level of standard deviation is reduced using a polynomial fit and increasing the order of the polynomial. This however has to be carefully interpreted. In fact, the polynomial fit models the velocity distribution inside an interrogation bin finding the best match with the particle data. As a consequence there should be no surprise that the standard deviation resulting from a polynomial fit is lower compared to the result of a top-hat or a gaussian filter, but at the same time this should not be taken as an indication of a more accurate measurement. Besides, using a higher order polynomial for the same particles implies giving more "degrees of freedom" to the fit algorithm to find the best match with the particle data and consequently the calculated standard deviation is reduced even more. In fact, considering Figure 6.18d and 6.19d, it can be noticed that for the case of a quadratic polynomial fit the standard deviation is reduced at the cost of a noisier mean flow field, especially in the upstream region, thus indicating a drawback of the polynomial fit technique.

A better insight on the effect of the ensemble averaging method can be obtained by looking at the velocity profiles along y for fixed x coordinates. Two streamwise velocity profiles are investigated, choosing $x = 1.980$ m and $x = 2.180$ m in order to encompass the accelerated flow region and the wake, respectively. The velocity profiles are plotted in Figure 6.21, where almost no difference can be observed between the top-hat and the gaussian filter, and only a slight difference noticeable for the results of the linear polynomial fit. The quadratic polynomial fit instead shows a substantial difference in the peak acceleration and in the peak deceleration, respectively predicting a larger and a smaller value of velocity with respect to the other methods. This is an expected result as polynomial fit of higher orders are known to improve the resolution of

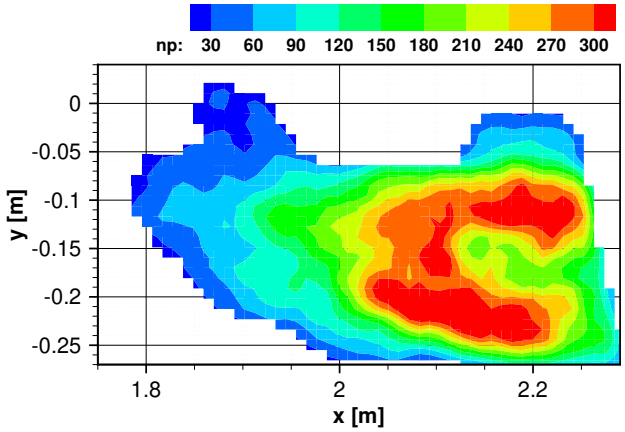

Figure 6.20: Contour of the number of particles found for the ensemble averaging using a linear bin size of $l_B = 42.5$ mm and an averaging non-dimensional time window of 1/821. Slice cut at 50% of the plate's span.

spatial gradients, thus providing a better estimate of the mean velocity within an interrogation bin [Agüera et al., 2016]. This however comes at the cost of a slightly noisier velocity distribution along y, in agreement to what was observed in Figure 6.19. The plots of the velocity profile also show the uncertainty of the phase-averaged velocity by means of error bars, where the uncertainty is calculated according to (3.3) and where N_I is calculated as explained in Section 5.1.2. A summary of the minimum and maximum uncertainty of the phase-averaged velocity along the velocity profiles for different ensemble averaging methods is given in Table 6.4. There it can be observed how the use of higher order polynomial fits reduces both minimum and maximum uncertainty along the velocity profile. The discussion given earlier about the interpretation of the standard deviation values resulting from the use of a polynomial fit applies here as well.

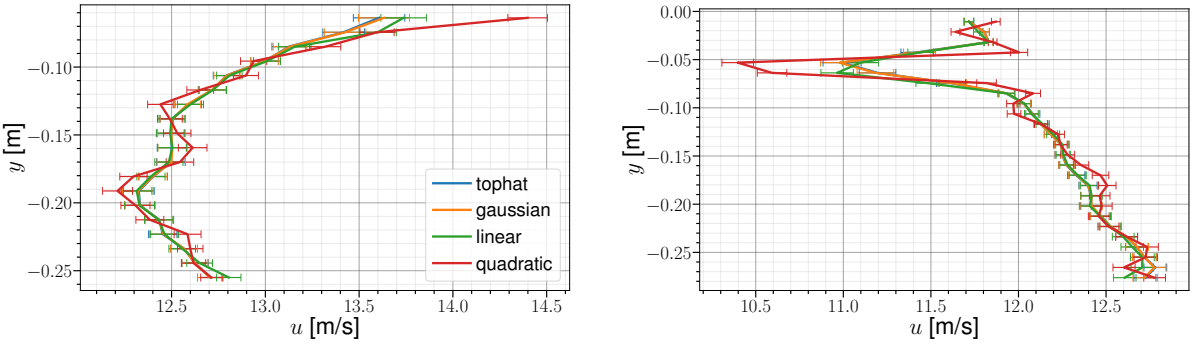

(a) Accelerated flow region ($x = 1.98$ m).

(b) Wake ($x = 2.18$ m).

Figure 6.21: Comparison of streamwise velocity profile along y for different ensemble averaging methods. Error bars represent the uncertainty of the average velocity in each point.

Another perspective on the effect of the ensemble average methods is offered by the evolution of the streamwise velocity during the average cycle at fixed points in space. Similarly to the analysis of the velocity profiles, two points on the considered z plane are chosen, $[x, y] = [1.980, -0.070]$ m and $[x, y] = [2.180, -0.060]$ m, respectively related to the accelerated flow region and to the wake. Also in this case there is no much difference among the different ensemble averaging methods except for the phases where the accelerated and decelerated flow kick in, with the quadratic polynomial fit predicting more extreme velocity peak and trough. Once again, the uncertainty of the phase-averaged velocity is indicated by means of error bars and a summary of the minimum and maximum uncertainty for different ensemble averaging methods is given in Table 6.5. Also in this case, the quadratic polynomial fit achieves lower values of uncertainty with respect to the other methods, resulting however in a less smooth evolution of the velocity in time.

From this section it is possible to conclude that the quadratic polynomial fit is the ensemble average method that gives the best performance in terms of spatial resolution, however at the cost of a noisier mean flow with respect the other ensemble average methods. This is especially true in regions where a relative small

Table 6.4: Minimum and maximum uncertainty of phase-averaged velocity along the velocity profiles encompassing the accelerated flow region and the wake, with a comparison of the different spatial ensemble averaging methods.

	Accelerated flow		Wake	
Method	$\epsilon_{\overline{u},min}$ [m/s]	$\epsilon_{\overline{u},max}$ [m/s]	$\epsilon_{\overline{u},min}$ [m/s]	$\epsilon_{\overline{u},max}$ [m/s]
Top-hat	0.068	0.137	0.027	0.109
Gaussian	0.066	0.136	0.026	0.109
Linear	0.065	0.121	0.026	0.104
Quadratic	0.057	0.105	0.025	0.090

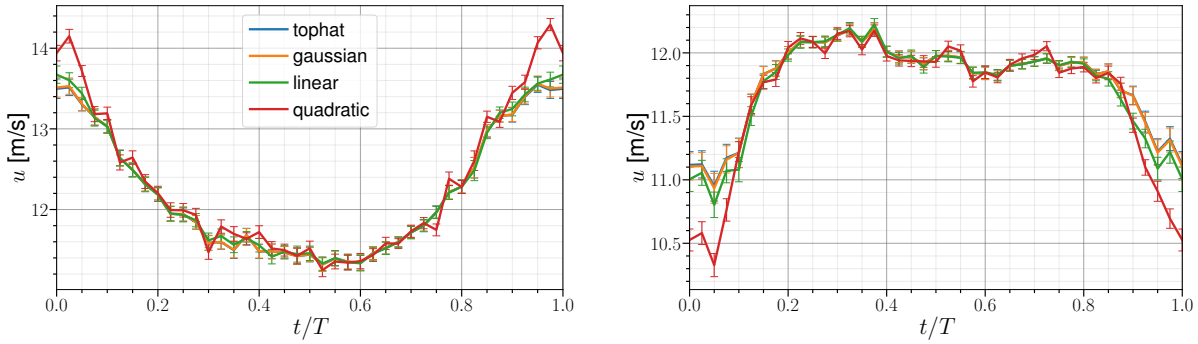

(a) Accelerated flow region ($[x, y]$ = [1.98, −0.07] m).

(b) Wake ($[x, y]$ = [2.18, −0.06] m).

Figure 6.22: Comparison of streamwise velocity during the average cycle for different ensemble averaging methods. Error bars represent the uncertainty of the average velocity at each phase.

Table 6.5: Minimum and maximum uncertainty of phase-averaged velocity during the average cycle for the points in the accelerated flow region and in the wake, with a comparison of the different spatial ensemble averaging methods.

	Accelerated flow		Wake	
Method	$\epsilon_{\overline{u},min}$ [m/s]	$\epsilon_{\overline{u},max}$ [m/s]	$\epsilon_{\overline{u},min}$ [m/s]	$\epsilon_{\overline{u},max}$ [m/s]
Top-hat	0.063	0.127	0.038	0.118
Gaussian	0.063	0.127	0.037	0.118
Linear	0.062	0.125	0.037	0.100
Quadratic	0.061	0.122	0.036	0.092

number of particles is available, making the application of high order polynomial fit rely on the availability of a large number of particles.

Effect of spatial bin variation

The effect of using different spatial bin sizes to phase-average the flow data is investigated considering only the quadratic polynomial fit method, given the better performance in terms of spatial resolution indicated in the previous analysis. Four spatial bin sizes are investigated: 85.0 mm, 28.3 mm, 21.3 mm and 17.0 mm, respectively corresponding to 1/2, 1/6, 1/8 and 1/10 of the plate's chord. Once again, no temporal information is considered, the spatial average is carried out taking for each phase an averaging non-dimensional time window of 1/821 and the minimum number of particles for each valid bin is set to 20.

The resulting contour of the streamwise velocity is shown in Figure 6.23. As expected, it is possible to notice how a larger linear bin size allows to average a bigger portion of the measured volume, given the higher probability of filling the interrogation bins with the required minimum number of particles. However, this happens at the cost of a spatial modulation of the velocity field, given the smaller spatial resolution achieved.

In fact, Figure 6.23a shows smaller velocities within the accelerated flow region and larger velocities within the wake region, compared to the baseline flow field of Figure 6.18d. On the positive side, the flow field observed in Figure 6.23a is smoother with respect to the baseline flow field, as more particles are found in each bin and thus the application of the quadratic polynomial fit results more robust. Nevertheless, the combination of quadratic polynomial fit with a large spatial bin size can lead to poor velocity calculation at the boundaries of the phase-averaged region, due to the extrapolation of particles' velocity data. In fact, in Figure 6.23a it is possible to notice some corners where the velocity achieves dubious large or small values. However, this problem is reduced as soon as a smaller spatial bin size is considered, since the probability and the amount of extrapolation for each bin at the boundary of the averaged region decrease with the linear size of the bin itself.

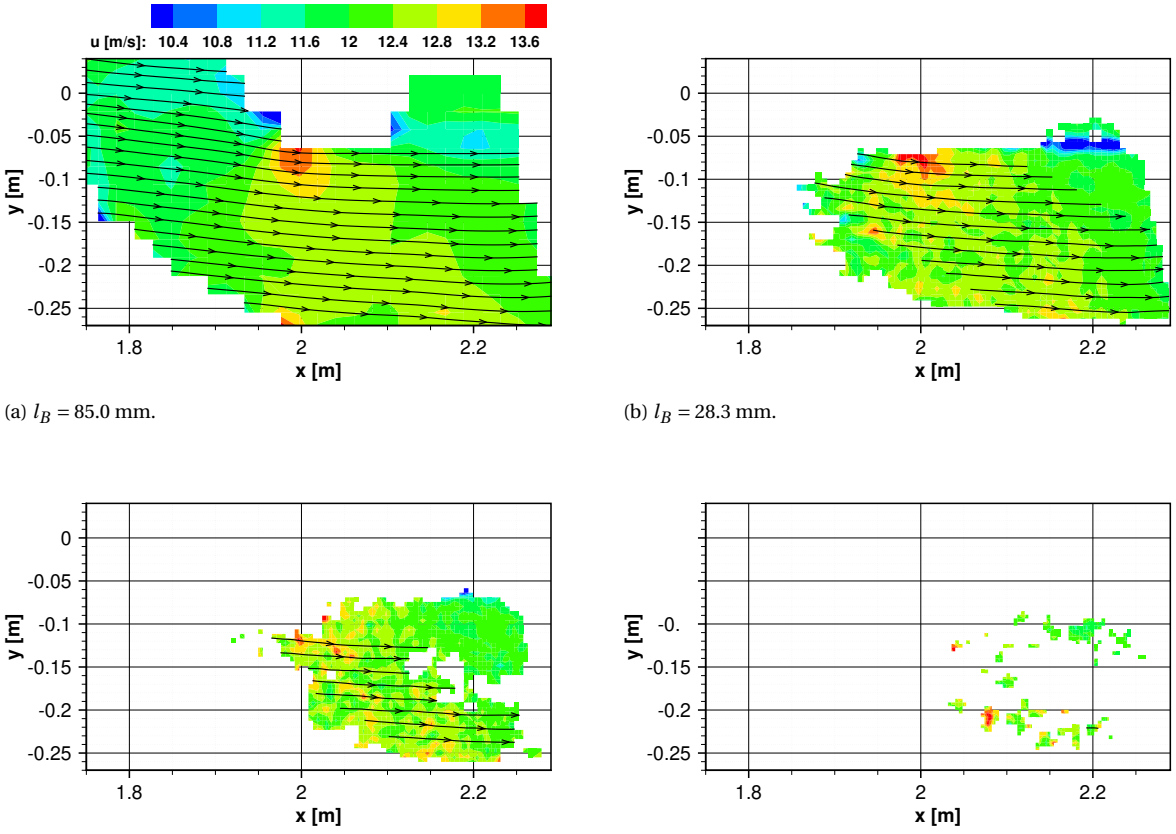

(a) $l_B = 85.0$ mm.

(b) $l_B = 28.3$ mm.

(c) $l_B = 21.3$ mm.

(d) $l_B = 17.0$ mm.

Figure 6.23: Comparison of streamwise velocity contour for different spatial bin sizes, using a quadratic polynomial fit and an averaging time window of 1/821 s. Slice cut at 50% of the plate's span.

The velocity contours resulting from the use of smaller spatial bins confirm that a finer spatial resolution is obtained, however at the cost of noisier mean flow and of a smaller region being averaged, given that less interrogation bins are filled with the required minimum amount of particles. For example, Figure 6.23b shows a larger velocity deficit in the plate's wake for a spatial bin size of 28.3 mm, however with more noise all over the flow field and with less information available with respect to what shown by Figure 6.18d. The amount of available information is further reduced for $l_B = 21.3$ mm and for $l_B = 17.0$ mm only very few bins are successfully filled.

The contours of the standard deviation of the streamwise velocity for the different spatial bin sizes investigated is shown in Figure 6.24. For the bin size larger than the baseline one, it is possible to observe how the plate's leading edge and the region upstream of the plate are still the parts of the flow field with the highest levels of velocity standard deviation. Other regions, including the wake, present a lower standard deviation with respect to what shown by Figure 6.19d. Similarly to what observed for the velocity contours resulting from smaller bin sizes, also the standard deviation contours show an improved spatial resolution in the description of the velocity scatter within the interrogation bins.

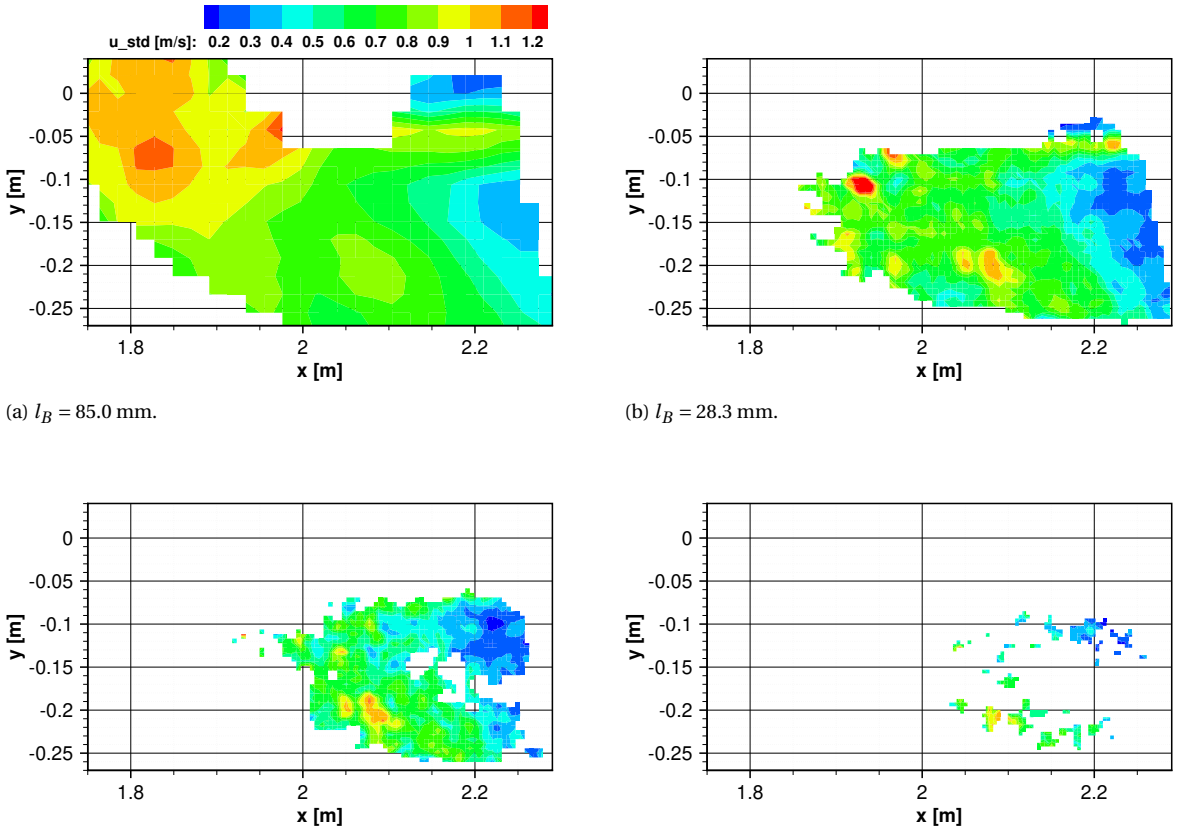

(a) $l_B = 85.0$ mm.

(b) $l_B = 28.3$ mm.

(c) $l_B = 21.3$ mm.

(d) $l_B = 17.0$ mm.

Figure 6.24: Comparison of streamwise velocity standard deviation contour for different spatial bin sizes, using a quadratic polynomial fit and an averaging time window of 1/821 s. Slice cut at 50% of the plate's span.

An investigation on the velocity profile along y is carried out also in this case, for the same x coordinates considered previously. The profiles resulting from the different spatial bin size are shown in Figure 6.25 and are compared to the baseline profile obtained with $l_B = 42.5$ mm. The velocity profile obtained with a larger bin size shows a substantial spatial modulation both in the accelerated flow region and in the wake region, with smaller velocity peak and velocity deficit, respectively. Furthermore, at the other boundary of the velocity profile ($y \approx -0.275$ m) it is possible to observe a velocity peak most probably caused by extrapolation of the particles' velocity data, as explained earlier. As far as smaller bin sizes are concerned, the velocity profiles are available for a smaller y interval and, especially for the accelerated flow region, appear to be noisier with respect to the baseline. Nonetheless, it is possible to notice how for $l_B = 28.3$ mm a finer spatial resolution is obtained in the wake, with a larger velocity deficit being predicted.

Similar observations can be made looking at the evolution of the streamwise velocity during the average cycle at the same fixed points in space previously investigated. The results are presented in Figure 6.26, where a comparison with the baseline bin size of 42.5 mm is given. Once again it is possible to notice how for a larger bin size the peak and trough of the velocity in the accelerated flow region and in the wake, respectively, suffer from a spatial modulation. Furthermore, as the spatial bin size is reduced, the availability of phase-averaged data during the average cycle decreases.

Effect of temporal bin variation

As explained in Section 5.1.2, also temporal information can be included in the binning process. Here the effect of using different temporal bin sizes is investigated, considering the quadratic polynomial fit method. The main objective of the use of temporal information is to increase the spatial resolution, so a spatial bin size of 17.0 mm is used for demonstration purpose. Four different temporal bin sizes are investigated: 1/32, 1/16, 1/4 and 1/2 of the reference cycle period T_{ref}. A non-dimensional time window of 1/800 around each phase is used to mask out empty bins in each analysed phase, in order to avoid the visualization of spurious

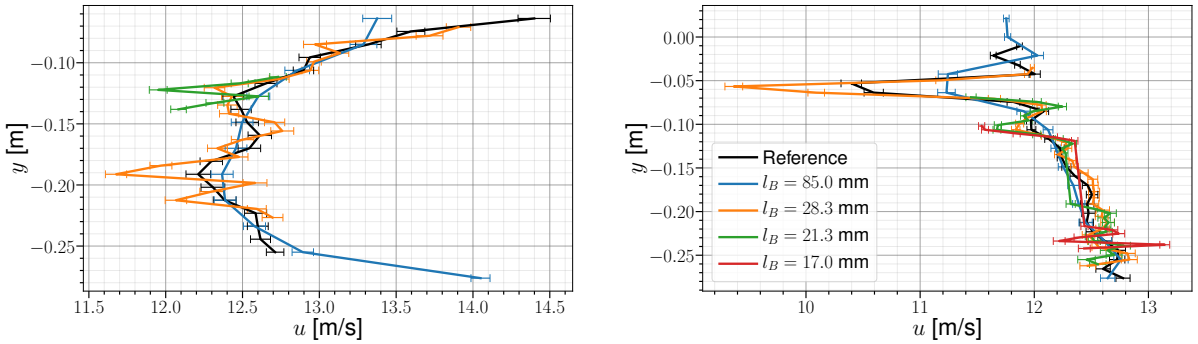

(a) Accelerated flow region (x = 1.98 m).

(b) Wake (x = 2.18 m).

Figure 6.25: Comparison of streamwise velocity profile along y for different spatial bin sizes. Error bars represent the uncertainty of the average velocity in each point. The reference line is given by the quadratic polynomial fit with l_B = 42.5 mm.

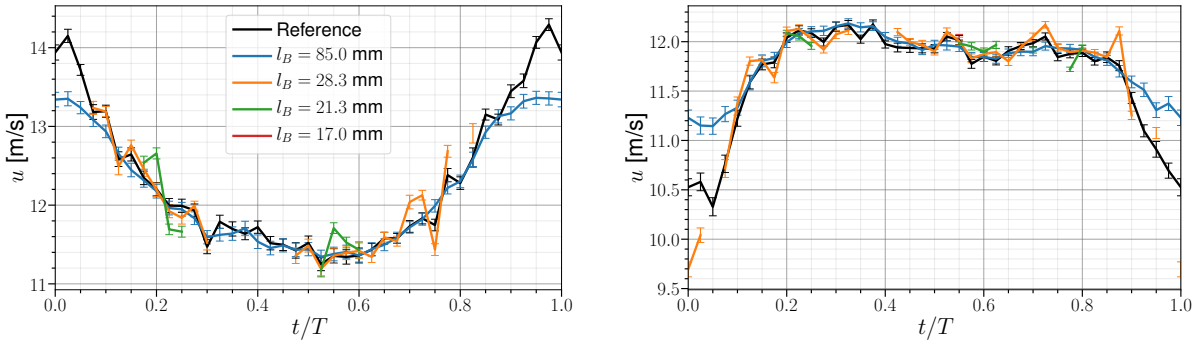

(a) Accelerated flow region ($[x, y]$ = [1.98, −0.07] m).

(b) Wake ($[x, y]$ = [2.18, −0.06] m).

Figure 6.26: Comparison of streamwise velocity during the average cycle for different spatial bin sizes. Error bars represent the uncertainty of the average velocity at each phase. . The reference line is given by the quadratic polynomial fit with l_B = 42.5 mm.

bins. The minimum number of particles for the remaining subset of bins is set to 30, which is double the amount of the coefficients needed for the spatio-temporal quadratic regression.

Figure 6.27 shows the streamwise velocity contours resulting from the different temporal bin size. First and foremost it is possible to observe that in comparison to Figure 6.23d, the use of a 17.0 mm spatial bin size combined with temporal information returns a rather full flow field for the observed slice. This means that the use of temporal information successfully allows to increase the spatial resolution obtainable with the phase-average binning of Lagrangian tracks. However, for the chosen temporal bin sizes it can be noticed how the increase of bin size produces only a marginal addition of successfully phase-averaged bins, probably due to the bin detection criterion. More in general only few changes are noticeable in the magnitude of the streamwise contours from one temporal bin size to the other, except for the wake of the case with t_B/T_{ref} = 1/2 showing a smaller velocity deficit in the wake. At the same time however, it is possible to observe how the use of a smaller temporal bin size produces a noisier mean flow, similarly to what was noticed for the reduction of the spatial bin size in Figure 6.23.

The contours of the standard deviation of the streamwise velocity component are shown in Figure 6.28. Comparing these results with the baseline standard deviation field of Figure 6.19d, it is possible to notice how the highest level of scatter of the phase-averaged velocity are still found in the part upstream of the plate, at the plate's leading edge and in the plate's wake. It can be also observed as outside these regions, the standard deviation level appears to be similar. However, the noticeable changes in standard deviation with respect to the values obtained in Figure 6.19d do not seem to follow a general pattern. As a consequence, no clear conclusion can be drawn on the effect of the use of spatio-temporal ensemble average on the standard deviation.

Also in this case the velocity profile along y is investigated, using the same x coordinates employed in the

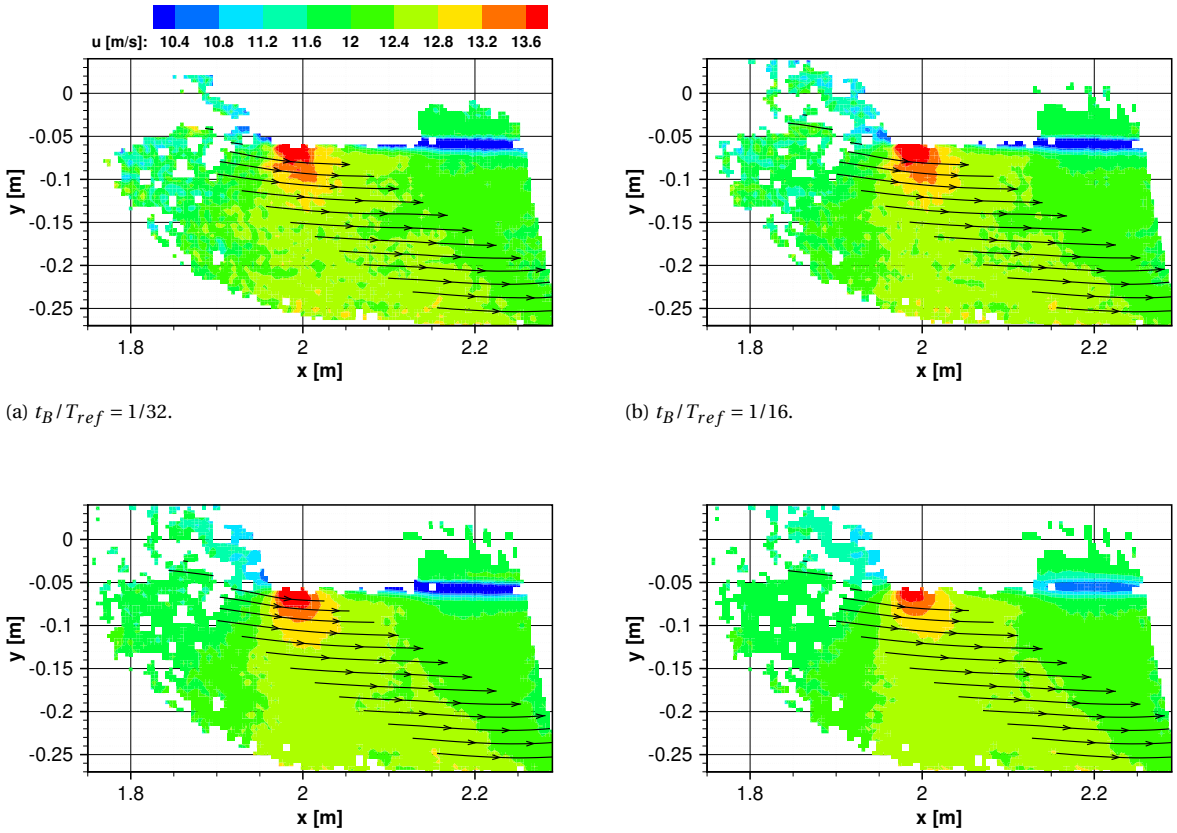

(a) $t_B/T_{ref} = 1/32$.

(b) $t_B/T_{ref} = 1/16$.

(c) $t_B/T_{ref} = 1/4$.

(d) $t_B/T_{ref} = 1/2$.

Figure 6.27: Comparison of streamwise velocity contour for different temporal bin sizes, using a quadratic polynomial fit, a spatial bin size of 17 mm and a bin detection non-dimensional time window of 1/800. Slice cut at 50% of the plate's span.

previous analyses. The resulting profiles are shown in Figure 6.29 and are compared to the baseline profile obtained for $l_B = 42.5$ mm and without any use of temporal information. Both profiles of the accelerated flow region and of the wake show a strong gain in spatial resolution with $t_B/T_{ref} = 1/32$. A smaller gain in both regions is given by the temporal bin size of 1/16 of the cycle period. As the temporal bin size increases to 1/4 and 1/2 of the cycle period a modulation of the profile is observed. While in the wake $t_B/T_{ref} = 1/4$ still gives a better resolution of the velocity deficit in comparison with the baseline profile and $t_B/T_{ref} = 1/2$ results in a comparable resolution, in the accelerated flow region the velocity trend of both profiles is inverted close to the plate surface. Such inversion should not be related to the beginning of the boundary layer of the plate. In fact the spatial resolution achievable with a spatial bin size of 17 mm is unsuitable to capture a boundary layer with a thickness in the order of 2 mm, according to Blasius equation [4]. Rather, the inversion of the velocity profile has to be ascribed to a combination of temporal modulation of the velocity, due to the large time kernel, and to the edge effect of the polynomial fit. Besides the observations on the effects on the spatial resolution of the velocity, it can be noticed how a smaller temporal bin size results in a noisier velocity profile, in agreement to what observed in Figure 6.27.

A summary of the minimum and maximum uncertainty along each velocity profile is given in Table 6.6. As far as the accelerated flow region is concerned, only $t_B/T_{ref} = 1/32$ returns lower minimum and maximum uncertainty, while for the other temporal bin sizes either one or both results larger. In the wake region the maximum uncertainty is always larger than the baseline one, except for $t_B/T_{ref} = 1/2$, while $t_B/T_{ref} = 1/32$ is the only temporal bin size resulting in a lower minimum uncertainty.

The temporal modulation of velocity can also be assessed looking at its evolution during the average cycle.

[4] For laminar boundary layers over a flat plate, the Blasius equation gives the thickness of the boundary layer at a distance x from the leading edge of the plate: $\delta \approx 4.91\sqrt{\nu x/u_\infty}$, where ν is the kinematic viscosity and u_∞ is the free-stream velocity. At a distance x equal to the chord of the plate used in this work, the boundary layer thickness is approximately equal to 2.3 mm.

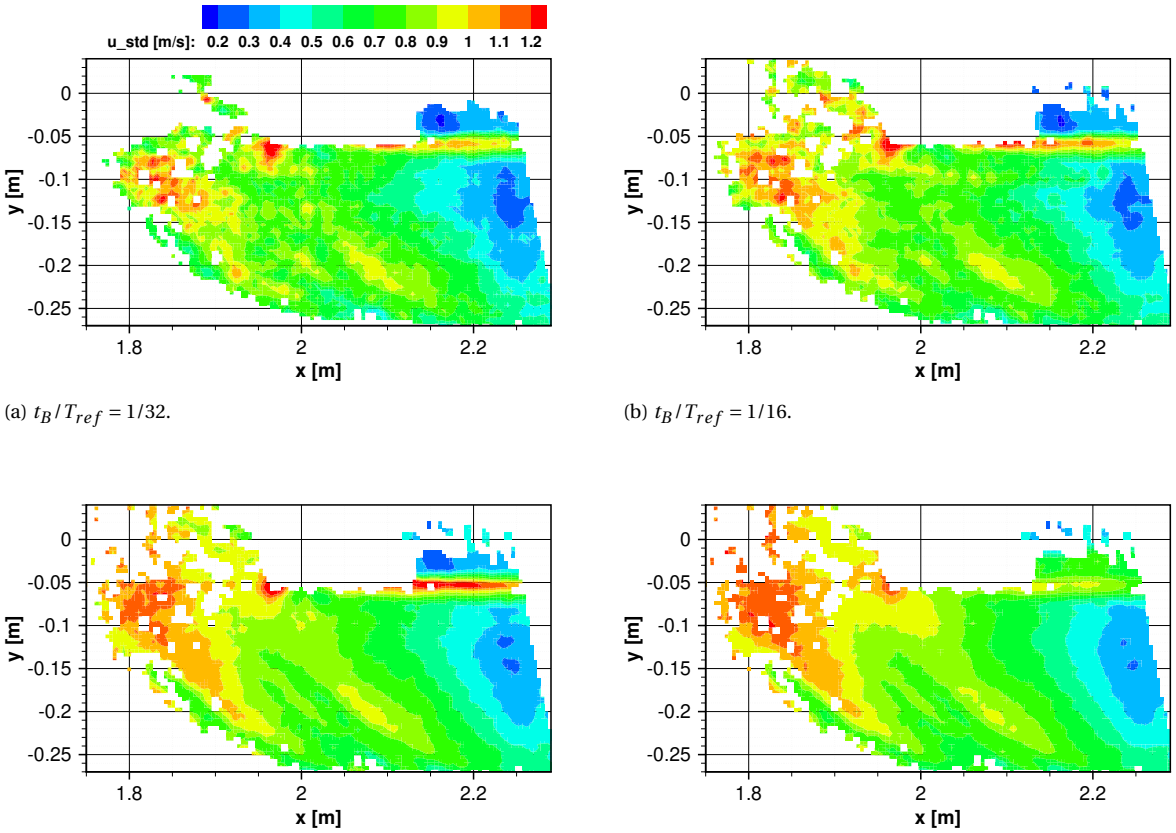

(a) $t_B/T_{ref} = 1/32$.

(b) $t_B/T_{ref} = 1/16$.

(c) $t_B/T_{ref} = 1/4$.

(d) $t_B/T_{ref} = 1/2$.

Figure 6.28: Comparison of streamwise velocity standard deviation contour for different temporal bin sizes, using a quadratic polynomial fit and a spatial bin size of 17 mm and a bin detection time window of 1/821 s. Slice cut at 50% of the plate's span.

Table 6.6: Minimum and maximum uncertainty of phase-averaged velocity along the velocity profiles encompassing the accelerated flow region and the wake, with a comparison of different temporal bin sizes.

	Accelerated flow		Wake	
Temporal bin size t_B/T_{ref}	$\epsilon_{\overline{u},min}$ [m/s]	$\epsilon_{\overline{u},max}$ [m/s]	$\epsilon_{\overline{u},min}$ [m/s]	$\epsilon_{\overline{u},max}$ [m/s]
None (baseline)	0.057	0.105	0.025	0.090
1/32	0.053	0.097	0.020	0.097
1/16	0.057	0.107	0.025	0.098
1/4	0.060	0.110	0.028	0.116
1/2	0.063	0.097	0.042	0.084

The same points of the flow field used for previous analyses are also considered here. The resulting temporal velocity profiles are shown Figure 6.30, where a comparison with the baseline case is given as well. As far as the point in the accelerated flow region is concerned, only a slight difference of the peak velocity is visible among the temporal bins with $t_B/T_{ref} = 1/32$, $t_B/T_{ref} = 1/16$ and $t_B/T_{ref} = 1/4$, while for 1/2 of the cycle period the modulation appears more evident. Regarding the point in the wake, the results are analogous, with the trough velocity increasing as the temporal bin is enlarged and with $t_B/T_{ref} = 1/2$ resulting in a strong modulation of velocity. Nonetheless, in agreement with previous observations, the temporal profiles reveal how a larger temporal bin size results in smoother velocity evolution over time.

Also for this analysis the minimum and maximum uncertainty of the different velocity signals are consid-

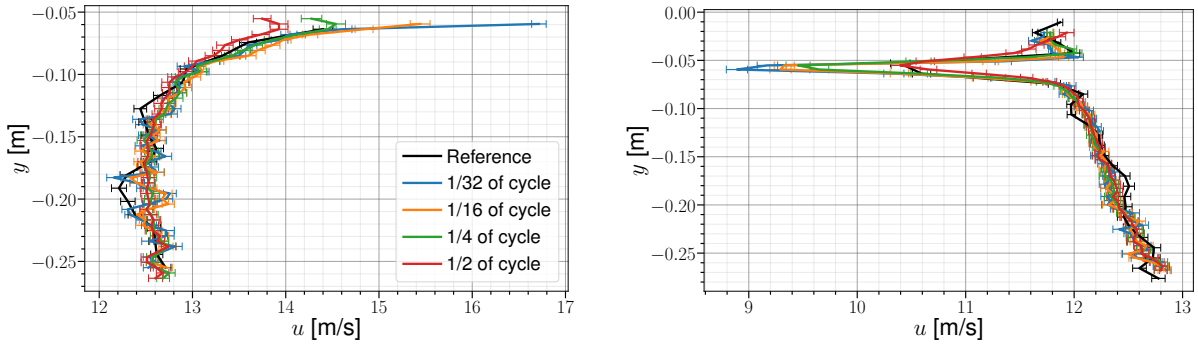

(a) Accelerated flow region ($x = 1.98$ m).

(b) Wake ($x = 2.18$ m).

Figure 6.29: Comparison of streamwise velocity profile along y for different temporal bin sizes. Error bars represent the uncertainty of the average velocity in each point. The reference line is given by the quadratic polynomial fit with $l_B = 42.5$ mm without use of temporal information

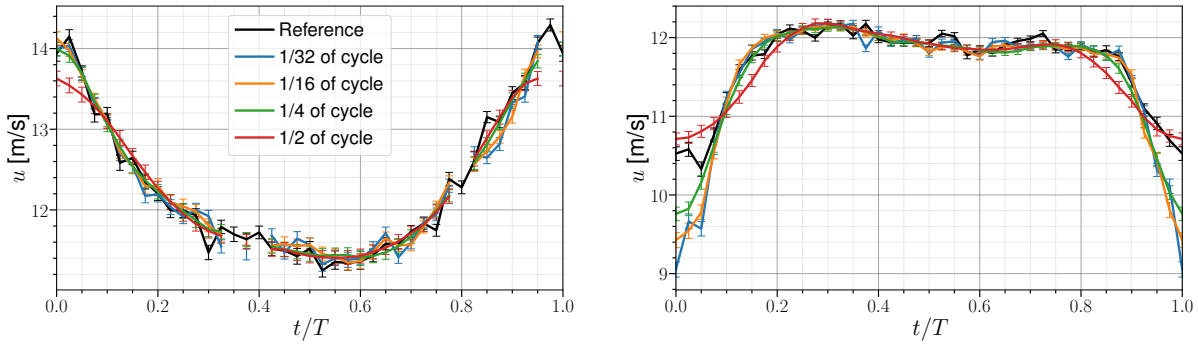

(a) Accelerated flow region ($[x, y] = [1.98, -0.07]$ m).

(b) Wake ($[x, y] = [2.18, -0.06]$ m).

Figure 6.30: Comparison of streamwise velocity during the average cycle for different temporal bin sizes. Error bars represent the uncertainty of the average velocity at each phase. The reference line is given by the quadratic polynomial fit with $l_B = 42.5$ mm without use of temporal information.

ered and reported in Table 6.7. For the point in the accelerated flow region all temporal bin sizes produce a minimum uncertainty larger than the reference value and a maximum uncertainty lower than the reference value. Concerning the point in the wake, the minimum uncertainty is reduced only using $t_B/T_{ref} = 1/32$, while the maximum uncertainty is lowered only for large temporal bins such as $t_B = 1/4$ and $t_B = 1/2$ of the cycle period. Overall, it is recalled how the uncertainty of the mean flow (as well of the standard deviation) derived from ensemble averaging methods employing a polynomial fit should not be considered an absolute indication on the accuracy of the measurements, but rather in relative terms with respect to the assumed polynomial distribution of the velocity.

Table 6.7: Minimum and maximum uncertainty of phase-averaged velocity during the average cycle for the points in the accelerated flow region and in the wake, with a comparison of different temporal bin sizes.

	Accelerated flow		Wake	
Temporal bin size t_B/T_{ref}	$\epsilon_{\overline{u},min}$ [m/s]	$\epsilon_{\overline{u},max}$ [m/s]	$\epsilon_{\overline{u},min}$ [m/s]	$\epsilon_{\overline{u},max}$ [m/s]
None (baseline)	0.061	0.122	0.036	0.092
1/32	0.069	0.095	0.035	0.097
1/16	0.073	0.094	0.037	0.098
1/4	0.081	0.091	0.042	0.087
1/2	0.086	0.092	0.044	0.081

In conclusion, it is evident how in the choice of the temporal bin size a trade-off has to be made among the achievable spatial resolution, the smoothness of the mean velocity and the potential temporal modulation of the measurement.

6.3. Fluid-structure consistency

Once the phase average approach has been assessed for both flow and structure, it is necessary to evaluate the consistency of measurement results between the two. This is achieved finding the ratio of particles that are found beyond the surface constituted by the measured markers. For this aim, the PIV-HFSB measurement set (see Table 4.3) is used, benefiting in this way from the large amount of particles available. Two fluid-structure regions are investigated: one encompassing the half span of the plate and the other encompassing the tip of the plate. As far as the former is concerned, a limited set of flow particles is available for the assessment, due to a combination of a gust generator malfunction and of a problematic behaviour of the processing software.

First, the markers are phase-averaged and for each phase and a surface is constructed triangulating the resulting points. The flow particles within a non-dimensional time window of 1/800 centred on the analysed phase are then considered (same as the detectability time window used for the spatio-temporal phase average), as illustrated for phase $t/T_{ref} = 0$ in Figure 6.31a. From this set of particles, only the ones with an absolute distance from the triangulated surface resulting below a certain threshold are further considered. The threshold is defined as twice the positional uncertainty of the CVV probe along its imaging direction at a distance of 598.53 mm, approximately corresponding to the maximum distance of the plate's tip from the probe itself. According to the discussion of Schneiders et al. [2018], the positional uncertainty at such distance results to be 5.06 mm and thus the threshold is set to 10.12 mm. At this point, using the MATLAB function `point2trimesh` it is possible to distinguish between valid flow particles and particles penetrating the surface obtained from the triangulated markers by looking at the sign of the calculated distance from the surface itself. An illustration of the resulting particles for phase $t/T_{ref} = 0$ is given in Figure 6.31b.

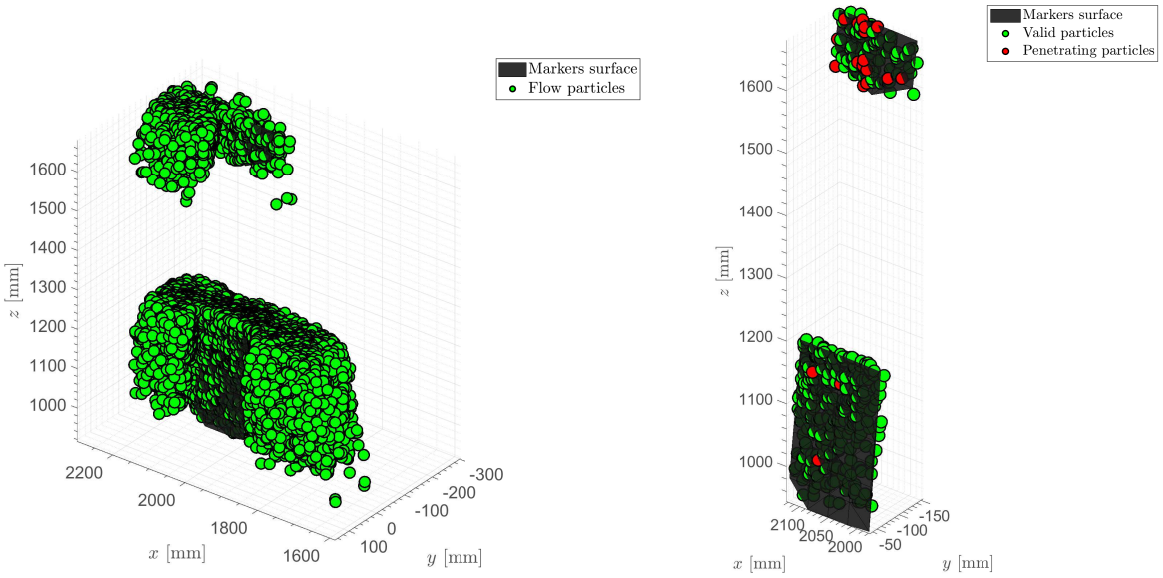

(a) Markers surface and entire set of tracked flow particles for the considered phase.

(b) Markers surface and reduced set of tracked flow particles, with an indication of the particles penetrating into the structure.

Figure 6.31: Illustration of the position of the flow particles with respect to the surface obtained from the triangulation of the plate's markers for phase $t/T_{ref} = 0$. The centre of the front side of the CVV probe for the tip acquisition has approximately the following coordinates: $[x, y, z] = [2327, -428, 1733]$ mm.

Once the particles penetrating into the structure are discerned for each phase from the valid particles it is possible to define a parameter called penetration probability and to investigate its variation over the average cycle. The penetration probability is defined taking the ratio between the number of penetrating particles

N_{pen} and the total number of particles falling within the distance threshold previously discussed N_{thr}:

$$P_{pen} = \frac{N_{pen}}{N_{thr}}. \tag{6.2}$$

Figure 6.32 shows the evolution of the penetration probability for both the midspan and the tip particles, providing also an indication of the plate's tip displacement corresponding to each phase. The phase-averaged tip displacement plot for the analysed case is given for reference in Figure 6.33 [5]. It can be observed how for the midspan particles a smoother evolution is found with respect to what calculated for the tip particles. This can be mainly ascribed to the limited number of particles available at the tip, as mentioned earlier, which results in a noisy penetration probability profile. However, it is evident how the average penetration probability of the tip particles is larger with respect to the one of the midspan particles. Furthermore, the curve of the latter reveals a clear higher level of penetration probability when plate moves away from the probe (positive tip displacement). Both observations are in agreement with expectations, as the positional uncertainty of the CVV probe along its imaging direction is known to increase with the distance from the probe itself. For this reason it is reasonable to expect that the furthest is the structure surface from the probe, the more particles penetrating such surface will be found.

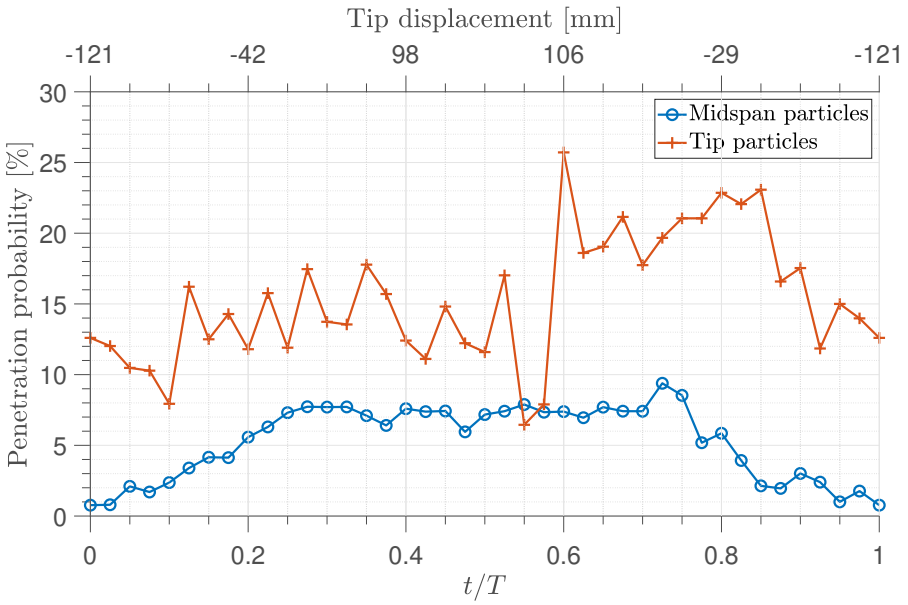

Figure 6.32: Phase-averaged markers and fitted surface for $t/T = 0$.

From Figure 6.32, the mean and maximum penetration probability of the midspan particles amount to 5.3% and 9.4%, respectively, while for the tip particles the corresponding values are 15.3% and 25.7%. Another important aspect for this assessment is constituted by the amount of penetration of the particles. This is evaluated in terms of the penetration distance, which is defined as the distance of the penetrating particles from the structure surface. The cumulative distribution function of the penetration distance of the midspan and of tip penetrating particles during the average cycle is calculated and plotted in Figure 6.34. The steeper initial gradient of the midspan curve suggests that the corresponding penetrating particles have a smaller penetration distance with respect to the penetrating particles of the tip group. Thus, the average smaller level of penetration probabilities for the midspan particles also coincides with a smaller penetration distance, which is in agreement with the argument of the positional uncertainty of the CVV probe along the imaging direction (more positional uncertainty corresponds to a larger potential difference from the real particle position and consequently to a larger penetration distance). In conclusion, it can be stated that for the analysed configuration 95% of penetrating flow particles located in the midspan portion of the plate is expected to have a penetration distance smaller than 6.7 mm, while the same amount of penetrating particles in the tip region is expected to have a penetration distance smaller than 7.6 mm.

[5] Here the tip displacement is calculated averaging the y position of the top 5 phase-averaged markers and subtracting the time-averaged y position of the same markers in the wind-tunnel off condition from the phase-averaged values.

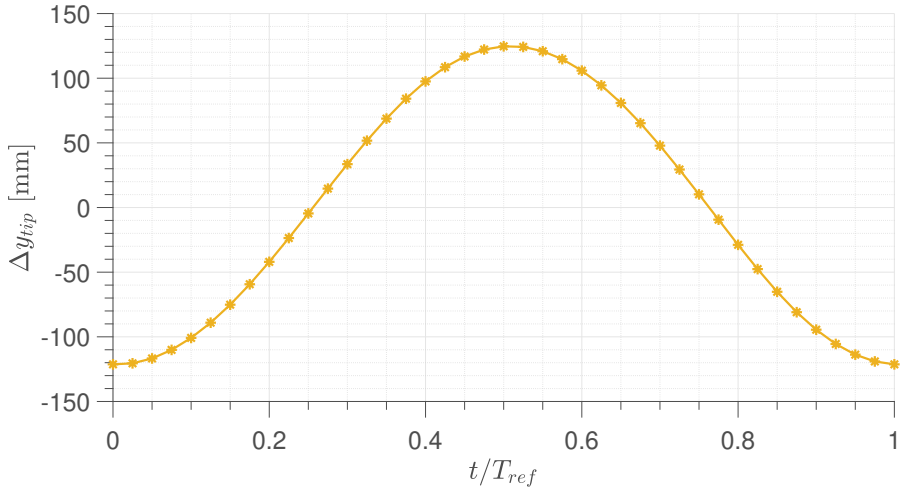

Figure 6.33: Phase-averaged tip displacement for the PIV-HFSB measurement set.

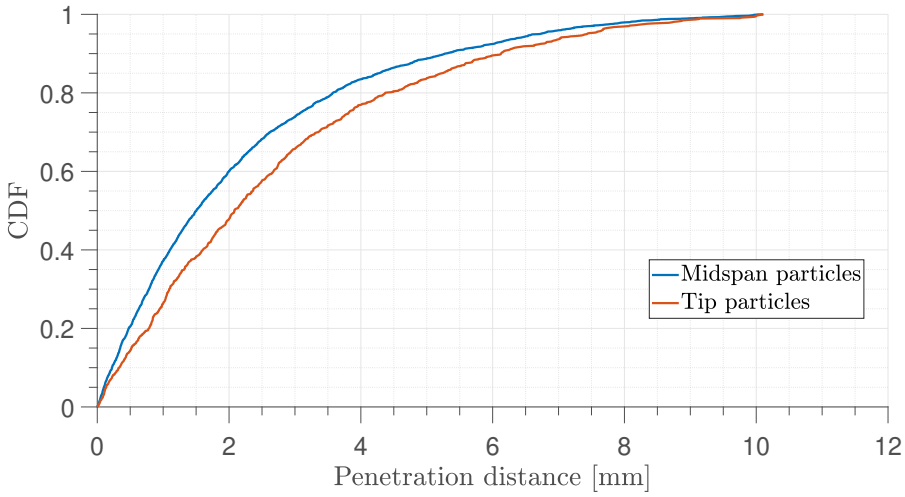

Figure 6.34: Cumulative distribution function of the penetration distance of the markers penetrating into the structure.

6.4. Fluid-structure interaction visualization

The combination of the phase-averaged description of flow and structure allows to visualize the FSI phenomenon studied, as it is done in Figure 6.35. The plate results are obtained processing one acquisition for each PIV volume shown in Figure 4.13b, thus using the data of the PIV-HFSB measurement set. Regarding the flow, four independent views in the midspan region of the plate and one in the tip region are considered, thus representing only a part of the plate and of the total measurement volume. At least six acquisitions are used for each view to obtain the results shown in the figure. A spatio-temporal ensemble average is carried out, using a quadratic polynomial fit. The spatial bin size is taken as $l_B = 28.3$ mm, corresponding to 1/6 of the plate chord, while the temporal bin size is taken as $t_B/T_{ref} = 1/16$. These sizes are chosen with the objective of reducing the noise of the mean flow field with respect to what was observed in the previous sections. Finally, the non-dimensional time window for the bin detection is taken as $1/(821/1.5)$, in order to have a smaller probability to leave empty valid bins.

Four different phases of the gust cycle are presented, namely $t/T_{ref} = 0$, $t/T_{ref} = 0.25$, $t/T_{ref} = 0.5$ and $t/T_{ref} = 0.75$. The corresponding phase-averaged tip displacement is the same of that shown in Figure 6.33. According to such figure, the selected phases correspond respectively to the plate tip being at the closest distance from the CVV probe, at an intermediate distance, at the largest distance and again at an intermediate distance.

The 3D view given in Figure 6.35 is composed by the plate surface, which is obtained by means of a triangulation of the measured markers, by a slice cut at $z = 1096$ mm (approximately 50% of the plate span)

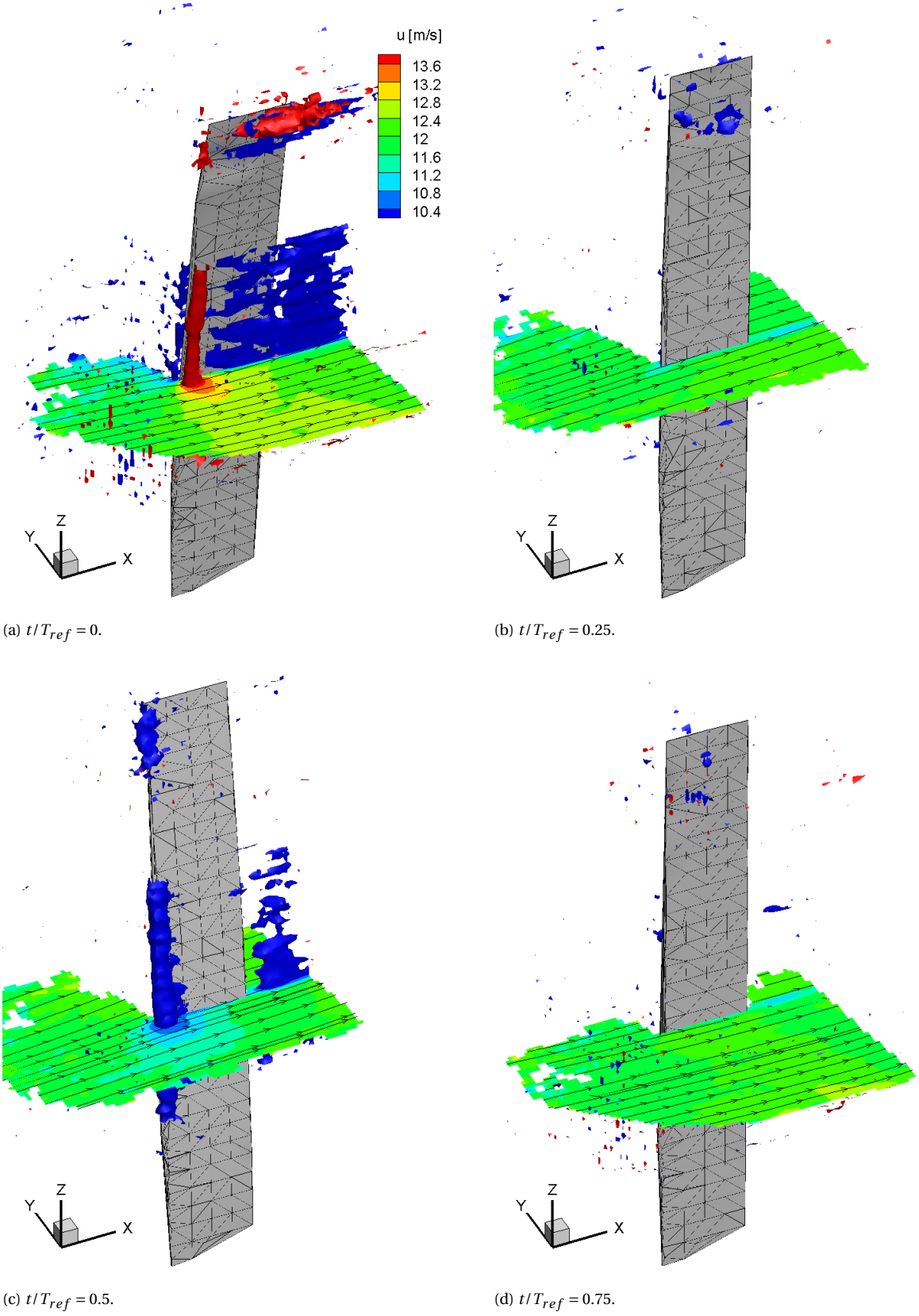

(a) $t/T_{ref} = 0$.

(b) $t/T_{ref} = 0.25$.

(c) $t/T_{ref} = 0.5$.

(d) $t/T_{ref} = 0.75$.

Figure 6.35: 3D visualization of the FSI phenomenon. Slice cut at $z = 1096$ mm with contour of the streamwise velocity u. Iso-surfaces of $u = 10.4$ m/s and $u = 13.8$ m/s.

coloured with the streamwise component of the velocity u and seeded with 3D streamlines, and by two iso-surfaces of the same velocity component, one for $u = 10.4$ m/s (corresponding to $u/u_\infty = 0.87$) and the other for $u = 13.8$ m/s (corresponding to $u/u_\infty = 1.15$). It is possible to notice that for phase $t/T_{ref} = 0$ a coherent structure of accelerated flow can be observed over the midspan region in the proximity of the quarter chord of the plate, while for the same region a coherent structure of decelerated flow is formed for phase $t/T_{ref} = 0.5$. This observation suggests that, as a consequence of the periodic gust field, the plate produces a positive and a negative lift force depending on the considered phase. In fact, the iso-surface of accelerated flow can be associated with a suction side, while the iso-surface of decelerated flow can be associated with a pressure side. The gust field is visible from the streamlines, which are deflected for phases $t/T_{ref} = 0$ and $t/T_{ref} = 0.5$. In the other two phases the streamlines are more straight and no accelerated or decelerated flow structures are observable. The iso-surface of decelerated flow can also be observed for $t/T_{ref} = 0$ and $t/T_{ref} = 0.5$ in the wake of the plate, while for the other two phases the slice reveal how a weaker wake is captured from the measurements. For phase $t/T_{ref} = 0$ the iso-surface of decelerated flow is also visible close to the plate surface. Given that the spatial bin size is one order of magnitude larger than the expected boundary layer thickness, such part of the iso-surface should not be considered as the start of the boundary layer. Rather, it has to be ascribed to the edge effect of the polynomial fit at the boundary of the cartesian grid.

The same slices of Figure 6.35 are shown from the top with a 2D view in Figure 6.36. There, the contour of the suction and pressure sides can be observed again, respectively for phase $t/T_{ref} = 0$ and $t/T_{ref} = 0.5$. Two-dimensional streamlines are also given in the plots, showing an evident deflection for the mentioned phases. Once again, for phases $t/T_{ref} = 0.25$ and $t/T_{ref} = 0.75$ it can be noticed how the streamlines appear to be undisturbed and no noticeable velocity acceleration or deceleration is observed, exception made for the small velocity deficit captured in the wake. The flow acceleration and deceleration are thus caused by a certain angle of attack of the incoming velocity seen by the plate, which is actually the effect of the combination of the gust field and the velocity of the plate itself. The contribution of the velocity of the plate to the effective angle of attack will be analysed later.

As far as the combined measurement is concerned, the results of the different phases suggest that the measured flow field follows coherently the movement of the plate, thus providing a qualitative confirmation of the consistency of the measurements. However, regions of permeation between flow and structure can be found looking for example at Figure 6.36b and with a proper 3D inspection of the domain. Indeed, in Section 6.3 it was shown that a certain number of flow particles penetrating into the structure can be expected due to the positional uncertainty of the CVV probe. However, another cause of the permeation regions stems from the ensemble averaging process. In fact, even if only particles from the correct side of the plate are found, interrogation bins spanning across the plate surface and having the centroid beyond it may result in a permeating portion of flow when particles fall inside the part of the bin on the observed side of the plate. A smart process for the generation of the structured cartesian grid used for the ensemble average should take into account the structural measurement in order to generate a compliant grid.

The same slice of Figure 6.36 is used to visualize the contour of the y component of the velocity, v, in order to have an overview of the gust field acting on the plate. This is shown in Figure 6.37, where it can be noticed how positive or negative values of v dominate the flow field depending on the considered phase. As expected from the previous discussion, larger absolute values of v can be observed for phases $t/T_{ref} = 0$ and $t/T_{ref} = 0.75$, while for the other phases more moderate values are found, suggesting that the flow is almost undisturbed with respect to the free-stream.

Interesting flow features can also be observed in the tip region of the plate. Figure 6.38 shows a 3D visualization of the plate at phase $t/T_{ref} = 0$ with the same iso-surfaces of the streamwise velocity as mentioned earlier, but with a different slice, this time taken at $z = 1725$ mm, so slightly above the tip of the plate. Such slice shows the contour of the z component of the velocity, w, and is seeded with 3D streamlines. A clear separation between positive and negative values of w can be spotted across what would be the projection of the tip of the plate on the slice plane. This indicates the presence of a tip vortex, with the air moving from the pressure side of the plate to the suction side. Furthermore, a coherent structure of accelerated flow can be noticed over the downstream half of the plate's chord. This has probably nothing to do with the interaction of the plate with the gust, rather it is likely related to the proximity of the CVV probe. In fact, such acceleration can be ascribed to the interaction of the plate moving closer to the probe providing a decrease in the cross-section available for the flow and thus resulting in an acceleration with respect to the free-stream. An iso-surface of decelerated flow can be noticed as well, with similar features with respect to what observed for the midspan region. In fact, a part of the surface is in the wake, while another part results close to the plate's surface. If the former can be considered physical, the latter has to be ascribed once again to the edge effect

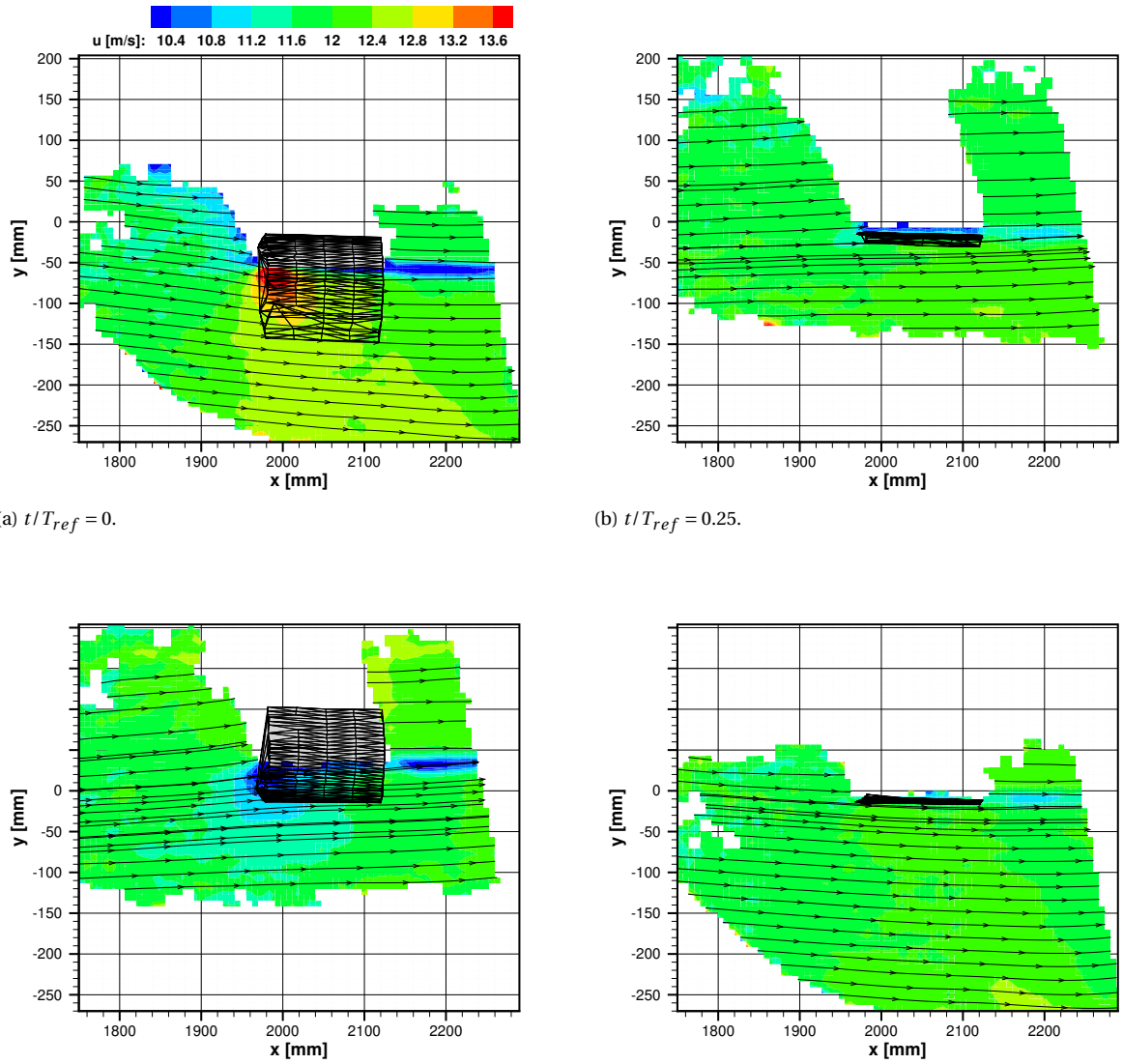

(a) $t/T_{ref} = 0$.

(b) $t/T_{ref} = 0.25$.

(c) $t/T_{ref} = 0.5$.

(d) $t/T_{ref} = 0.75$.

Figure 6.36: 2D top view of the streamwise velocity contour seeded with two-dimensional streamlines. Slice cut at z = 1096 mm.

of the polynomial fit.

The contour of w on the z = 1725 mm slice is shown in Figure 6.39 with a 2D view for the four phases considered earlier. The presence of the tip vortex is clearly noticeable for phase $t/T_{ref} = 0$, with positive values of w over the far side of the plate (corresponding to the pressure side) and with negative values on the close side (corresponding to the suction side) with respect to the CVV probe. For phase $t/T_{ref} = 0.25$ smaller absolute values of w are found, suggesting that the plate is not generating a significant lift. However, as soon as the plate's tip moves to the other side in phase $t/T_{ref} = 0.5$, a region with a relatively large positive value of w can be spotted again, this time on the close side of the plate, which acts as a pressure side. The region of negative w is too distant from the CVV probe to be capture in is entirety, however the transition from positive to negative values of w is visible. Finally, in phase $t/T_{ref} = 0.75$ the magnitude of w reduces, suggesting once again that the plate is not generating a significant lift.

Another interesting observation regarding the flow above the tip of the plate can be made looking at the v component, which is shown in Figure 6.40. The v component gives an indication on both the gust field and the tip vortex, since the air moving from the pressure to the suction side of the plate has to have a non zero velocity component in the y direction. For phases $t/T_{ref} = 0$ and $t/T_{ref} = 0.5$ (where lift is generated), a peak in the absolute value of v is indeed found over the downstream half of the plate's tip. This reveals an influence

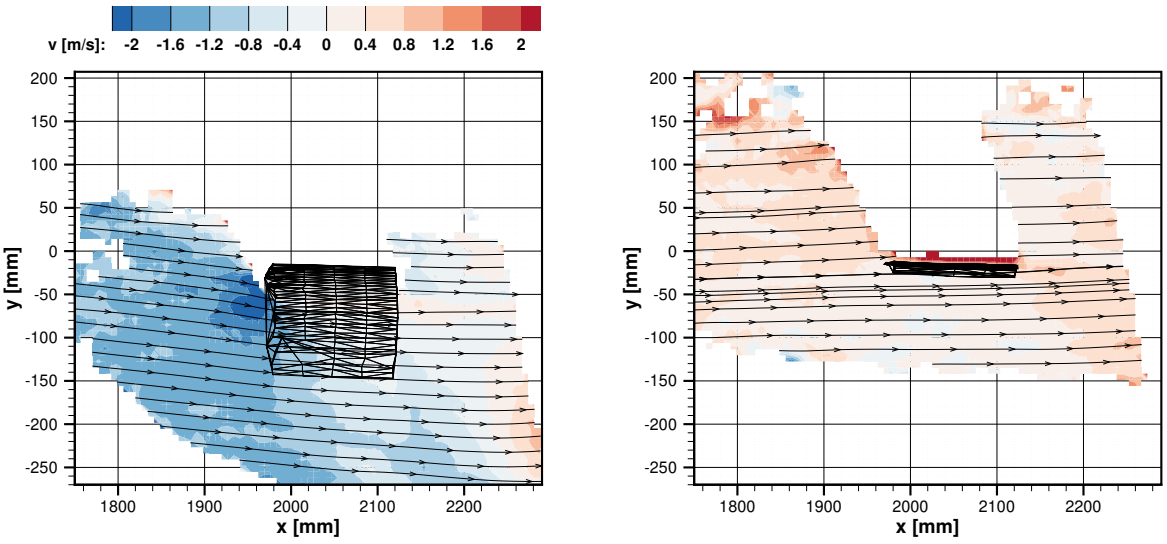

(a) $t/T_{ref} = 0$.

(b) $t/T_{ref} = 0.25$.

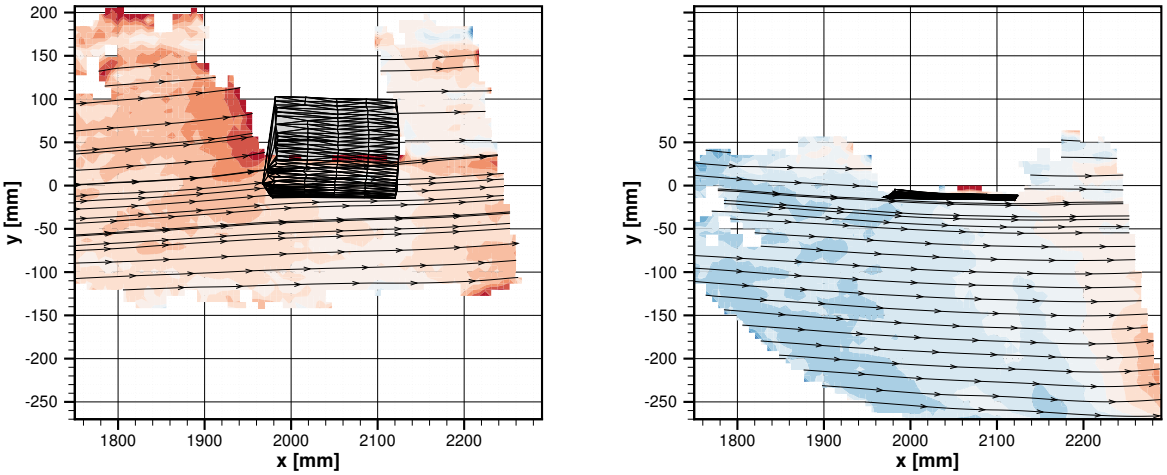

(c) $t/T_{ref} = 0.5$.

(d) $t/T_{ref} = 0.75$.

Figure 6.37: 2D top view of the y velocity contour seeded with two-dimensional streamlines. Slice cut at $z = 1096$ mm.

of the tip vortex on the gust field, since for the midspan region a peak in absolute value of v was found close to the leading edge of the plate. As far as the other phases are concerned, it can be observed once again that the magnitude of v is smaller, with the flow resulting closer to a free-stream condition.

A quantitative analysis of the dynamics of the FSI phenomenon is performed. The objective is to assess the relation among the angle of attack induced by the gust field α_{gust}, the angle of attack seen by the plate α_{plate} and the lift generated by the plate. The relation among the mentioned physical quantities can be explained by means of the sketch shown in Figure 6.41, where the dynamics of the studied phenomenon is illustrated. The gust field is generated through the actuation of the gust vanes, which provide an oscillating v component to the flow field. This oscillating v component is seen by the plate as an oscillating angle of attack of the incoming flow. The plate generates lift according to this angle of attack and it deforms according to its stiffness. The system is then governed by the interaction of aerodynamic, elastic and inertial forces, as described by Collar's triangle. However, while deforming the plate has a non-zero velocity in the y direction, which influences the effective angle of attack seen by the plate itself. It is then important to assess the influence of the plate velocity on the effective angle of attack.

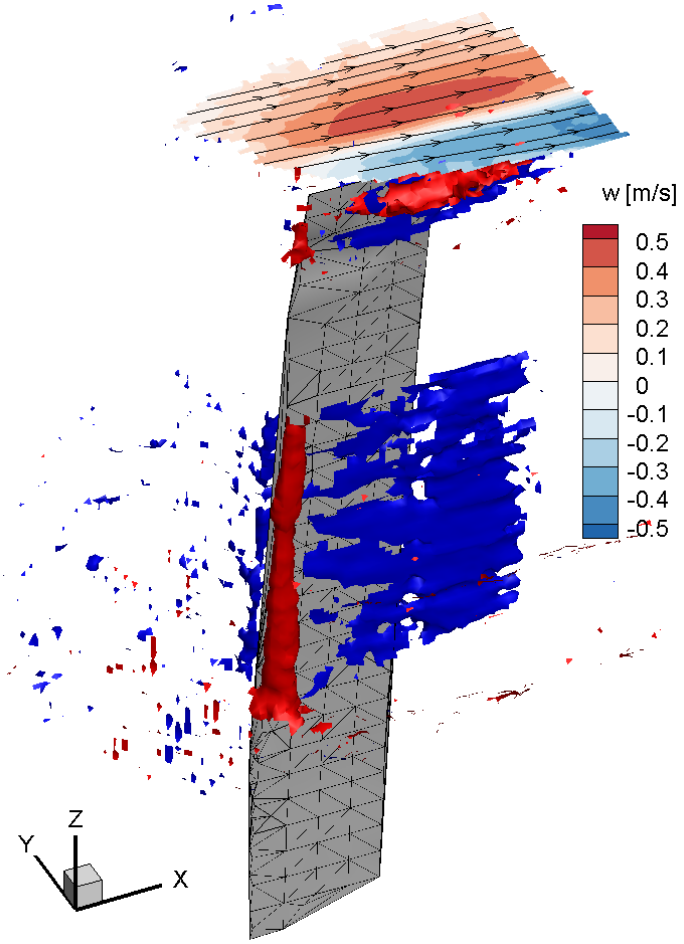

Figure 6.38: 3D visualization of the plate for $t/T_{ref} = 0$, with slice cut at $z = 1725$ mm showing the contour of the z component of the velocity. Iso-surfaces of $u = 10.4$ m/s and $u = 13.8$ m/s.

The angle of attack induced by the gust field is evaluated as:

$$\alpha_{gust} = \tan^{-1}\left(-v_{gust}/u_{\infty}\right), \tag{6.3}$$

while α_{plate} takes into account the velocity of the plate in the following way:

$$\alpha_{plate} = \tan^{-1}\left(-\left(v_{gust} - v_{plate}\right)/u_{\infty}\right). \tag{6.4}$$

u_{∞} is taken as the nominal value of 12 m/s, while v_{gust} is evaluated from the data of the slice shown in Figure 6.35, averaging the values found in the interval $y = [-0.1, 0.1]$ m half chord ahead of the plate leading edge ($x = 1955$ mm). v_{plate} is the y-velocity of the plate evaluated at the quarter chord point ($x = 1997.5$ mm). The lift generated by the plate can be related to the difference of the streamwise component of the velocity in proximity of the quarter chord of the plate with respect to the free-stream value:

$$\Delta u = u_{c/4} - u_{\infty}. \tag{6.5}$$

$u_{c/4}$ is evaluated averaging a segment of the same size of the spatial bin along the y direction starting from the closest point in the flow with respect to the point on the structure used for the calculation of v_{plate}. A positive value of Δu corresponds to the development of a suction side, while a negative value implies a pressure side. The negative sign in the definition of α_{gust} and α_{plate} is purely a convention to have a positive angle of attack corresponding to a positive Δu.

The analysis is carried out on the $z = 1096$ mm plane considered in the previous discussions and the results are shown in Figure 6.42. It is possible to notice how α_{plate} is slightly shifted in phase with respect to

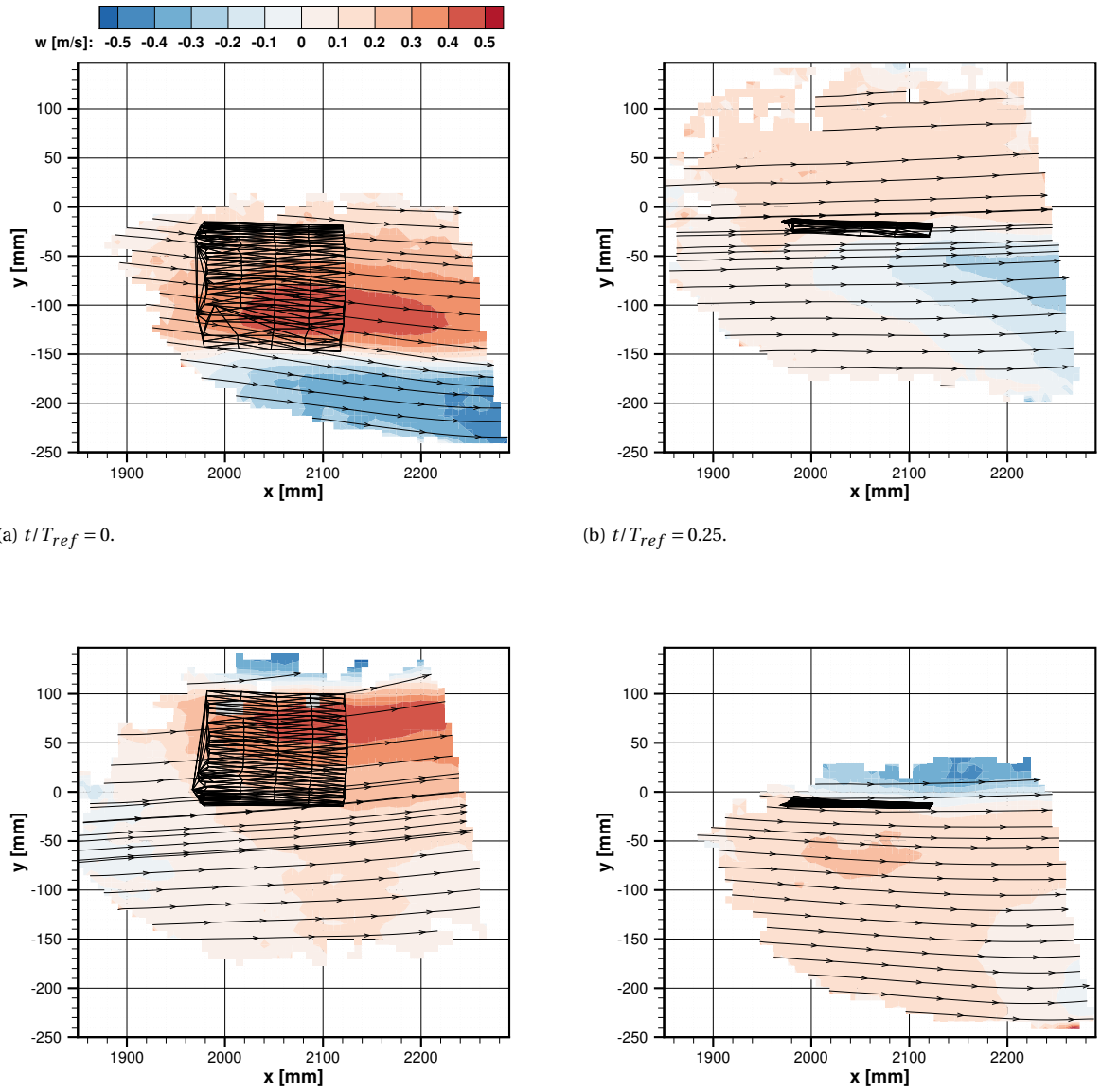

(a) $t/T_{ref} = 0$.

(b) $t/T_{ref} = 0.25$.

(c) $t/T_{ref} = 0.5$.

(d) $t/T_{ref} = 0.75$.

Figure 6.39: 2D top view of the z velocity contour seeded with two-dimensional streamlines. Slice cut at $z = 1725$ mm.

α_{gust} because of the contribution of the plate velocity. Besides this, the amplitude of α_{plate} is marginally smaller than the one of α_{gust}, meaning that for the studied case the velocity of the plate reduces the magnitude of the angle of attack seen by the plate itself. Also for Δu a phase shift can be noticed with respect to α_{plate}. This suggests that the unsteady lift has a slight delay with respect to the angle of attack seen by the plate, which can be related to the steady-state lift. The phase lag of lift is indeed a well-known phenomenon of unsteady aerodynamic flows. Two classical descriptions are given by the Theodorsen function for an airfoil oscillating in pitch and by Sears function for a fixed airfoil undergoing a sinusoidal gust [Wright and Cooper, 2014]. The case studied here could be simplified to an airfoil free to oscillate in heave and pitch under the action of a sinusoidal gust, thus representing a more complicated configuration. However, for small reduced frequencies such as in the case studied here ($k = 0.045$), the Theodorsen and the Sears functions are similar and as a consequence they can be taken as a rough reference. Figure 6.43 shows the comparison between the quasi-steady and the unsteady lift of an airfoil oscillating in pitch at a reduced frequency of $k = 0.05$. The slight phase lag of the unsteady lift seem to be comparable with the phase shift obtained for Δu in Figure 6.42.

In conclusion, the presented combined results of phase-averaged flow and structure, together with the

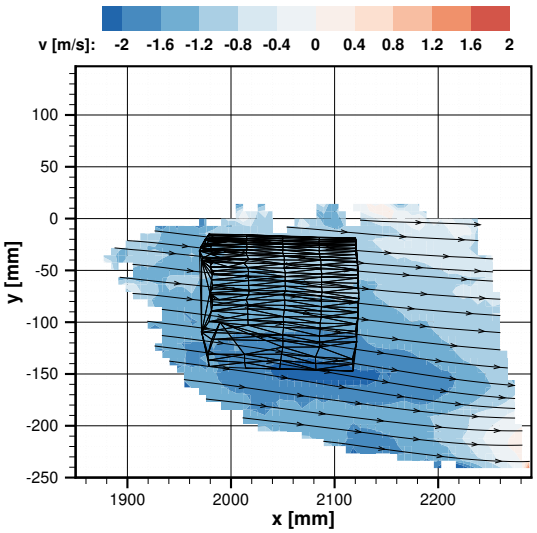

(a) $t/T_{ref} = 0$.

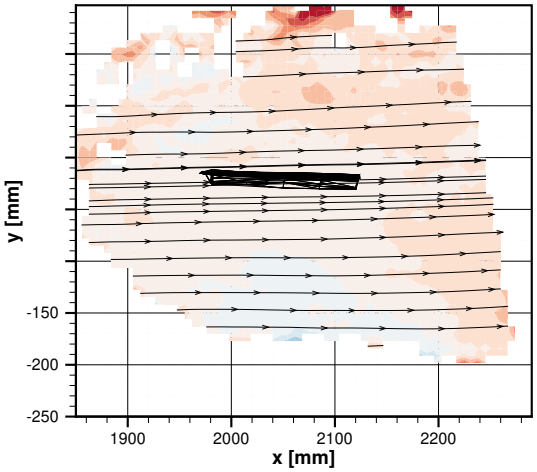

(b) $t/T_{ref} = 0.25$.

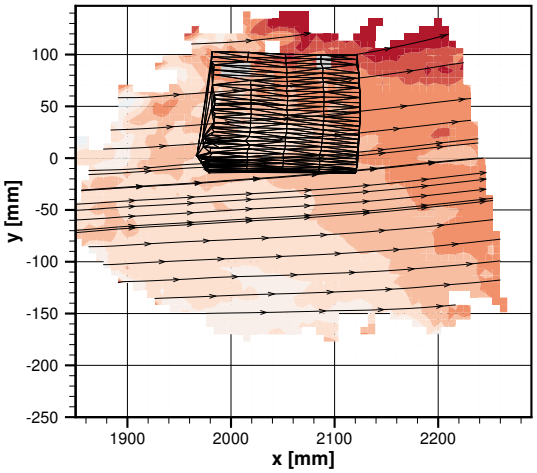

(c) $t/T_{ref} = 0.5$.

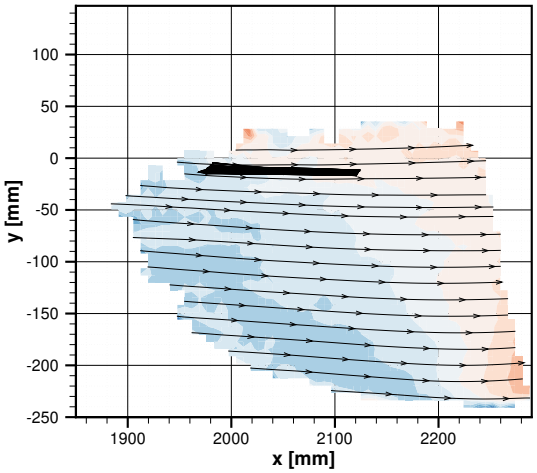

(d) $t/T_{ref} = 0.75$.

Figure 6.40: 2D top view of the y velocity contour seeded with two-dimensional streamlines. Slice cut at $z = 1725$ mm.

quantitative analysis performed, show the potential of Robotic Volumetric PIV for the characterization of FSI phenomena.

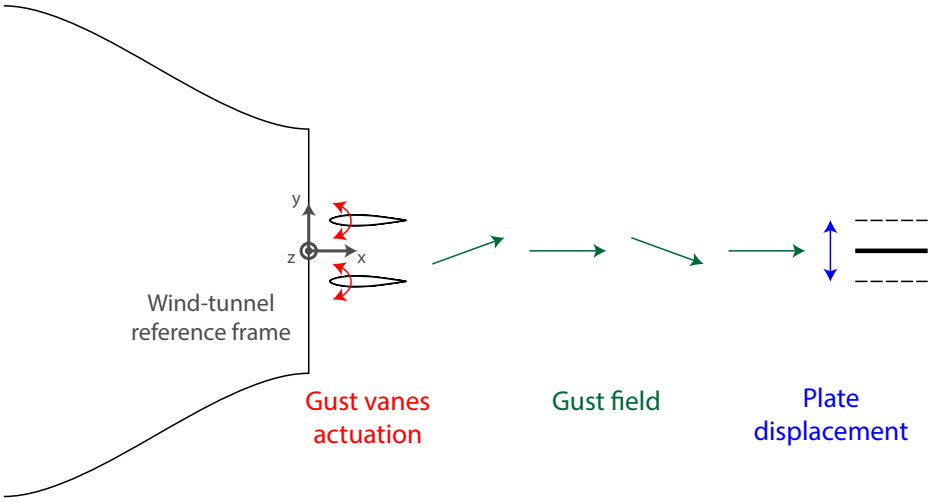

Figure 6.41: Illustration of the interaction between the gust field and the plate displacement.

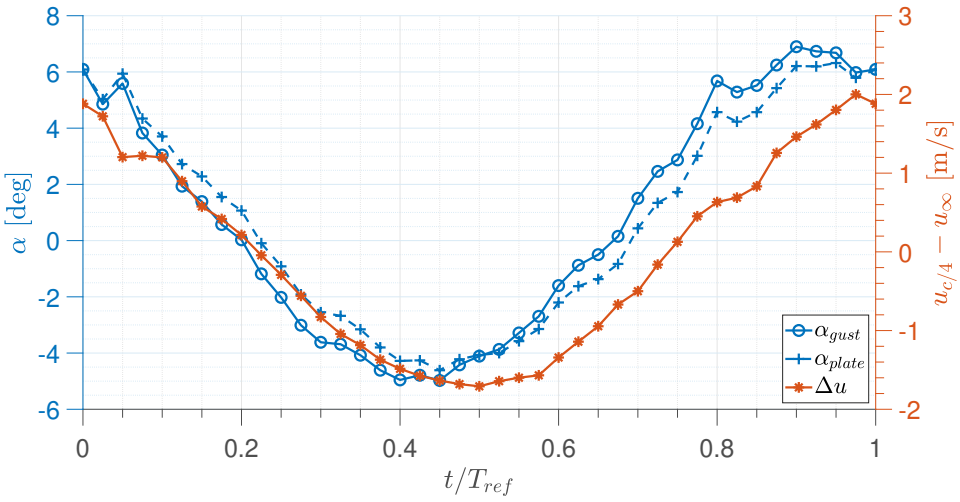

Figure 6.42: Comparison of the development of α_{gust}, α_{plate} and Δu during the average cycle.

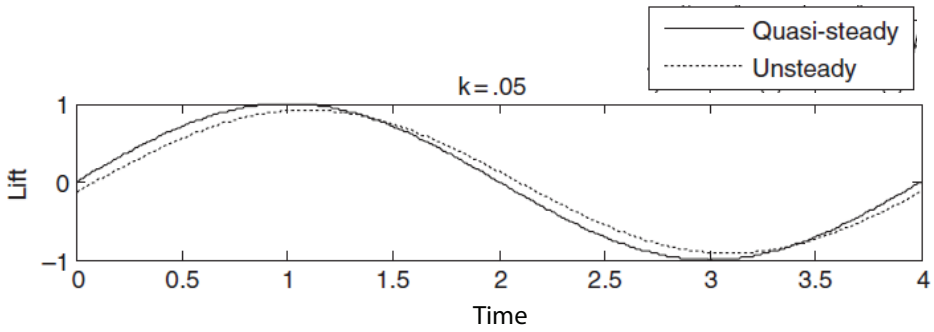

Figure 6.43: Lift for an aerofoil oscillating in pitch at a reduced frequency of $k = 0.05$. Adapted from Wright and Cooper [2014].

7

Conclusions and Recommendations

7.1. Conclusions

The motivation of the work presented in this master thesis originates from the challenges of modern aeronautical industry concerning the emission of air pollutants. This problem is usually tackled pursuing the design of lightweight vehicles, leading in this way to technical challenges in the field of aeroelasticity. Experimental work is still needed for verification of analitycal methods, understading of the physics underlying aeroelastic phenomena, assessment before flight tests and validation of computational tools. When investigating an aeroelastic phenomena in a wind-tunnel environment a proper characterization is needed for both the structural response and the developed flow field. A review of the state of the art showed how in literature there is a lack of quantitative flow visualization techniques, such as PIV, used in combination with structural measurement. The few examples available hardly ever achieve volumetric measurements of the flow and in general are limited to relatively small scale. Besides this the combination of aerodynamic and structural measurement is usually achieved by using two different systems, leading to a substantial complexity in the experimental setup caused by the combination of the measurement devices employed.

The advancement in large-scale aerodynamic measurements achieved with the introduction of Robotic Volumetric PIV [Jux et al., 2018] pave the way to new opportunities in the field of aeroelastic experiments. This work focused on the possibility of applying the Robotic Volumetric PIV technique to such field, with the aim of answering the following research question:

How feasible is the use of Robotic Volumetric PIV for large-scale experimental aeroelastic investigations, where both an unsteady flow field and dynamic structural displacements are simultaneously measured?

The use of Robotic Volumetric PIV for large-scale experimental aeroelastic investigation was demonstrated feasible by means of a wind-tunnel experiment involving the interaction of a flexible aluminium plate with a periodic gust. Velocities between 11 and 12 m/s and reduced frequencies between 0.044 and 0.045 were used for the experimental assessment. A set of sub-questions was formulated to give a more complete description of the research objective. The sub-questions are answered here based mainly on the results shown in Chapter 6

- *How is it possible to separate flow and structure by means of time-based filters using the images acquired by Robotic Volumetric PIV?*

The flow particles and the structural markers were separated by means of image pre-processing techniques based on time-filtering. The underlying hypothesis was that structural markers move much slower than flow particles in the acquired images. In this way a high-pass filter [Sciacchitano and Scarano, 2014] could be used to obtain a set of images containing only flow tracers and a time-minimum filter [LaVision, 2018a] could be used to obtain a set of images containing only structural markers. For the case studied in the present work the separation was successfully obtained, without any spurious contamination observed in the final results of flow and structure.

- *Are there any possible pitfalls within this approach?*

The use of the time minimum filter has a potential pitfall in case of the presence of a region of separated flow, where slow-moving flow particles in such region may appear in the structure images. Alternative filters avoiding this problem could consist in the dual of the temporal high pass filter proposed by Sciacchitano and Scarano [2014], so a temporal low pass filter, or in spatial filters where the separation between flow and structure would rely on an anisotropic shape of the structural markers.

- *What are the systematic and random errors of the instantaneous structural displacements measured by the Robotic Volumetric PIV system with respect to a reference measurement system?*

A *Polytec PSV-500 Scanning Vibrometer* was used as reference measurement system. The plate out-of-plane displacement of the centre-chord markers at different positions along the span of the plate was measured by both measurement systems. Three different positions were analysed: namely 9%, 49% and 96% of the span. The instantaneous measurement of the Robotic Volumetric PIV resulted in a bias error of 0.030, -0.096 and 0.144 mm and a random error of 0.380, 0.201 and 0.721 mm, respectively for the different span locations and based on 20 gust cycles.

- *What is the average standard deviation of the structural displacements of a single marker across the average cycle?*

The validity of the phase average approach for the structure was assessed evaluating the standard deviation of the displacements over the cycle, considering the point at 49% of the span used as well for the comparison of instantaneous measurements. The average standard deviation over the entire averaged cycle was approximately 0.379 mm, 0.518 mm and 0.450 mm for SV without HFSB, PIV without HFSB and PIV with HFSB, respectively. These results also indicated how the introduction of HFSB did not compromise the structural measurement performed with the Robotic Volumetric PIV system.

- *What is the mean and the standard deviation of the distance of multiple markers with respect to a physics-based model during the average cycle?*

The physical coherence of multiple markers resulting from different acquisitions was assessed comparing the position of the phase-averaged markers with a physical model fitted to the same markers. The physical model was based on a sine wave and on the first three vibrational modes of the plate, which were obtained with the commercial software MSC NASTRAN. The assessment was carried out considering a group of markers in the midspan region of the plate and another group of markers in the tip region of the plate. On average, the distance of the midspan markers from the fitted surface resulted to be 2.1 ± 1.2 mm, while for the tip markers it amounted to -1.3 ± 1.7 mm. Considering the largest mean distance of the two groups of markers in absolute value, the measured markers appeared to be consistent with the first three vibration modes of the plate within at worst 2.4 mm, corresponding to 2.5% of the tip displacement amplitude.

- *What is the range of standard deviation of the phase-averaged velocity field?*

The validity of the phase average approach was assessed also for the flow field looking at the standard deviation fields of the streamwise component of the velocity. Different ensemble average methods were employed and their results were compared together. Large parts of obtained flow fields had a standard deviation below 0.8 m/s, corresponding to 6.7% of the free-stream velocity. However, peaks in standard deviation were obtained in the region upstream of the plate, close to the plate's leading edge and in the plate's wake, where the value amounted up to 1.2 m/s, corresponding to 10% of the free-stream. The uncertainty of the mean velocity along the investigated spatial and temporal profiles resulted much smaller, ranging approximately between 0.05 m/s (0.4% of free-stream) and 0.12 (1% of free-stream) for the case of the spatio-temporal ensemble average.

- *What is the probability of finding flow particles penetrating into the measured structure during the average cycle?*

The consistency between the measured flow and structure was assessed finding the number of flow particles lying on the unobservable side of the plate and comparing such number with the total number of particles within a certain distance from the surface obtained from the measured markers. The distance threshold was taken as twice the positional uncertainty of the measurement system itself, considering the maximum

distance between the CVV probe and the plate's tip. Similarly to what done for the assessment of the physical coherence of multiple markers, two regions of the plate were considered: the midspan and the tip region. The mean and maximum penetration probability of the midspan flow particles amounted to 5.3% and 9.4%, respectively, while for the tip particles the corresponding values were 15.3% and 25.7%.

- *Considering the flow particles penetrating into the structure, how much do they penetrate it?*

The amount of penetration of the flow particles into the structure was studied looking at the cumulative distribution function of the penetration distance achieved by the particles lying on the unobservable side of the plate. For the analysed configuration, 95% of penetrating flow particles located in the midspan portion of the plate is expected to have a penetration distance smaller than 6.7 mm, while the same amount of penetrating particles in the tip region is expected to have a penetration distance smaller than 7.6mm.

- *To what extent is it possible to combine flow and structural measurements and to achieve a coherent description of the FSI phenomenon?*

The phase-averaged flow field and structural displacements were combined together offering a visualization of the FSI phenomenon. During the cycle, the plate and the flow region measured by the PIV system were shown to move accordingly. Few parts of flow permeating across the structure were found and were deemed to be caused not only by the positional uncertainty of the CVV system, but also by the ensemble averaging process. However, the Robotic Volumetric PIV system was demonstrated to be able to recognize the difference between the angle of attack induced by the gust field and the angle of attack effectively seen by the plate which was influenced by the plate's velocity. Furthermore, the velocity acceleration or deceleration with respect to the free-stream at the plate's quarter chord, considered as a surrogate of the lift generated by the plate, was shown to have a phase lag with respect to the change of the effective angle of attack seen by the plate. Such phase-lag was shown in qualitative agreement with analytical models considering the reduced frequency of the case studied ($k = 0.045$).

7.2. Recommendations

Although a first successful step in the application of Robotic Volumetric PIV to experimental aeroelastic investigations has been demonstrated in this work, several improvements can be envisioned. These concern various elements of the chain starting with the set-up of the experiment and finishing with the flow and structural results. More specifically, in this section recommendations for future work are provided regarding the experimental setup, the separation of flow and structure images, the post-processing of flow and structure tracks and the possibility of using the structural information to improve the flow measurement.

As far as the experimental setup is concerned, an improved understanding of the intrusiveness of the Robotic Volumetric PIV system in presence of moving objects is desirable. The results of the experimental case studied in this work suggests that the presence of the CVV probe causes noticeable flow accelerations when the object achieves the closest position to the probe itself, as it was observed for the tip of the plate. A dedicated investigation on the effect of interaction between the probe and moving objects is recommended in order to characterize the intrusiveness of the Robotic Volumetric PIV system for such cases.

In this work, separation of flow and structure images was achieved employing image pre-processing techniques that rely on the hypothesis that the movement of structural markers is on average much slower than the one of flow particles. This hypothesis may be limiting in case of large separated flow regions, where flow particles have low velocity, or in case of structures moving with relatively high frequencies. A possible way to overcome this limitation would be to employ markers painted with a particular shape and an advanced tracking algorithm able to distinguish flow particles from markers based on spatial filtering. More in particular, an anisotropic shape should be employed for markers, in order to make them different from the averagely isotropic shape of flow tracers recorded in the PIV images.

Regarding track post-processing, improvements can be recommended for both flow and structural analysis. As far as the latter is concerned, in the present study the instantaneous tracks were joined together to form the different markers of the plate surface using a purpose-developed algorithm. However a more global approach could be undertaken, for example describing the displacement of the entire structure with a function composed by a space-dependent component and a time-dependent component, similarly to what was done for the assessment of the physical coherence of multiple markers. The first can be assembled as a summation of the shape of the natural vibration modes of the object, in the same way as it is done for the calculation of dynamic aeroelastic response in commercial software such as NASTRAN. The time-dependent part can be

defined as a summation of sinusoids in a Fourier series style. A regression on all measured points retrieved by the particle tracking algorithm can then be carried out to find the coefficients of the function. In this way a smooth description in both space and time of the object motion would be obtained.

The post-processing of the flow tracks can also be improved. For example a structured or unstructured grid for ensemble averaging could be generated based on the measured surface of the object, similarly to how a CFD mesh is generated from the surface of a geometry. In this way the consistency between flow and structure would be imposed a-priori.

Finally, in this study the information related to the measured flow field and structural displacements are combined only for purpose of visualization. However, the velocity of the structural markers represent a boundary condition for the flow field. For this reason techniques for the assimilation of the structural velocities into the flow field should be developed, in order to increase the resolution of the measured velocity close to the wall. For example, boundary layer equations could be used to get the distribution of the velocity between the surface of the object and the first measured point of the flow field.

A

OptiTrack System

In Section 4.4.4 it was explained how one of the challenges of switching from the virtual experimental setup of RoboDK to the real experimental setup of the wind-tunnel consists in the estimation of the distances among the different components of the setup. In the same section it was also briefly introduced how this challenge was tackled using the *OptiTrack* system available in the OJF. In this appendix more information are given about the *OptiTrack* system and how it was used.

OptiTrack is an optical motion capture system where a set of synchronized cameras is used to compute the 3D position of objects by means of triangulation. To achieve this, the cameras are equipped with LED illumination providing IR light which is reflected by a set of retro-reflective markers placed on the tracked object. The *OptiTrack* system in the OJF is composed by 12 *Flex 13* cameras placed on the ceiling of the wind-tunnel as shown in Figure A.1. The system is completed by the Motive software, which is used to control the motion capture system, to process the acquired images and to manipulate the obtained 3D data.

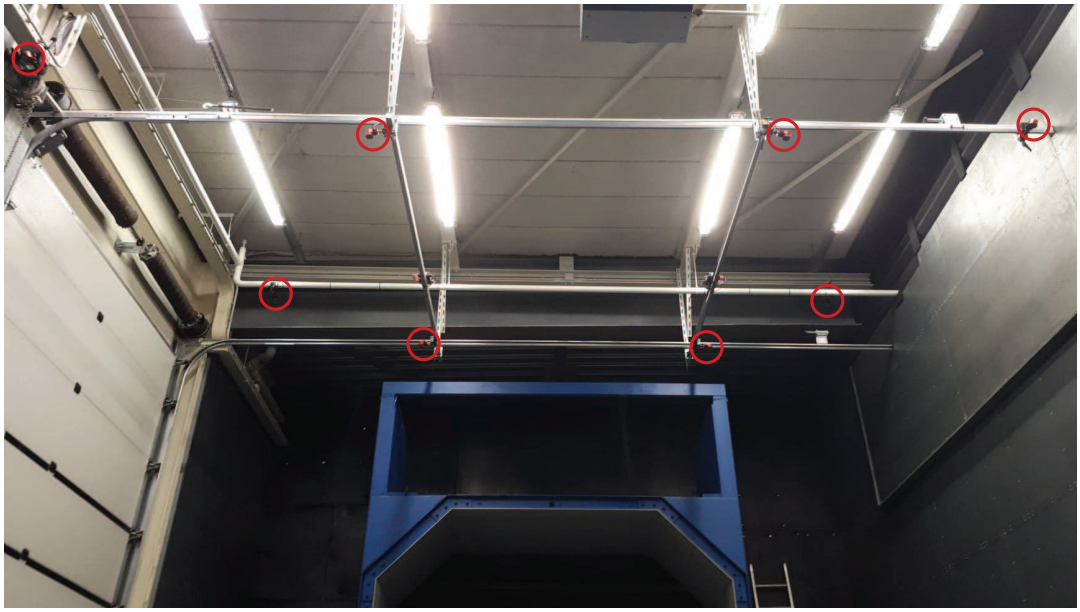

Figure A.1: Subset of the *Flex 13* cameras installed on the ceiling of the OJF.

A set of retro-reflective markers is placed on the surface of each interested object as shown in Figure A.2. With the markers in place, the *OptiTrack* system must be initially calibrated and this is done with two operations: wanding and setting the ground plane. The wanding process consists in repeatedly waving a calibration wand (see Figure A.3a) in front of the cameras, which record sample frames of the wand markers. During this operation a special care has to be taken such that the wand markers are recorded by each camera for a minimum amount of sample frames. The position of the markers in the 3D space is then calculated and

thanks to the known relative position of the markers on the wand the cameras are calibrated in terms of their position, orientation and amount of distortions in the captured images. In this way a 3D capture volume is obtained. The following operation consists in setting a ground plane and the origin of the reference system used for the marker tracking. This is achieved by means of a calibration square (see Figure A.3b) which is placed inside the 3D capture volume. For the present work the calibration square was placed on the floor of the wind-tunnel nozzle, with the x-axis aligned with the edge of the outlet section and the z-axis aligned with the wind-tunnel centreline. In this way, the origin of the tracking system was placed at the centre of the nozzle floor edge.

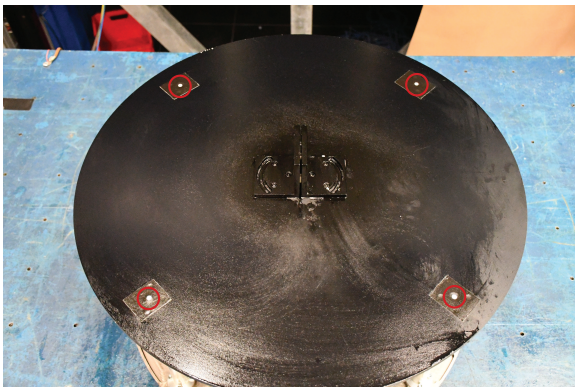

(a) Markers on the plate supporting the flexible plate.

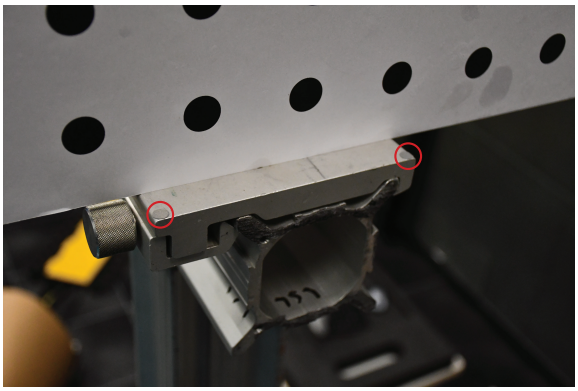

(b) Markers on the base of the calibration plate.

Figure A.2: Illustration of the retro-reflective markers placed on the objects forming the experimental setup.

(a) Calibration wand. Reproduced from: `https://www.optitrack.com/products/tools/`.

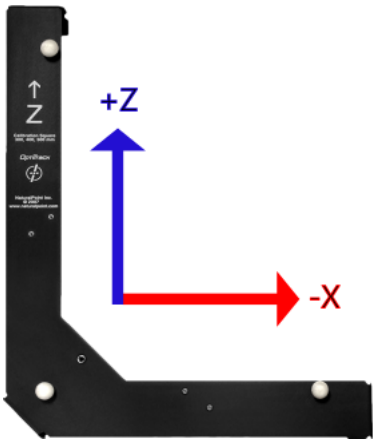

(b) Ground plane. Reproduced from: `https://v22.wiki.optitrack.com/index.php?title=Calibration_pane`.

Figure A.3: *OptiTrack* system calibration tools.

Once the tracking system is calibrated, a so called "rigid body" is build for each object from the respective markers. In this way the rigid bodies represent the upper surface of the objects and their centre is defined in MOTIVE as the pivot point. An illustration of the obtained rigid bodies is given in Figure A.4. At this point, using the live measurement probe tool, it is possible to measure the three components of the distance of a pivot point with respect to the origin of the reference frame or with respect to another pivot point, obtaining in this way the absolute or relative position of the rigid bodies. These distances are then used to specify the relative position of the objects in the ROBODK setup. However, it should be noticed how for this experiment the axes of *OptiTrack* reference frame are rotated with respect to the ones of the reference frame used for the PIV acquisitions (see Figure 4.10). The following relation has to be used when inputting the distances

measured with *OptiTrack* into RoboDK:

$$\begin{cases} \Delta x_{robodk} = -\Delta z_{optitrack} \\ \Delta y_{robodk} = -\Delta x_{optitrack} \\ \Delta z_{robodk} = \Delta y_{optitrack}. \end{cases} \tag{A.1}$$

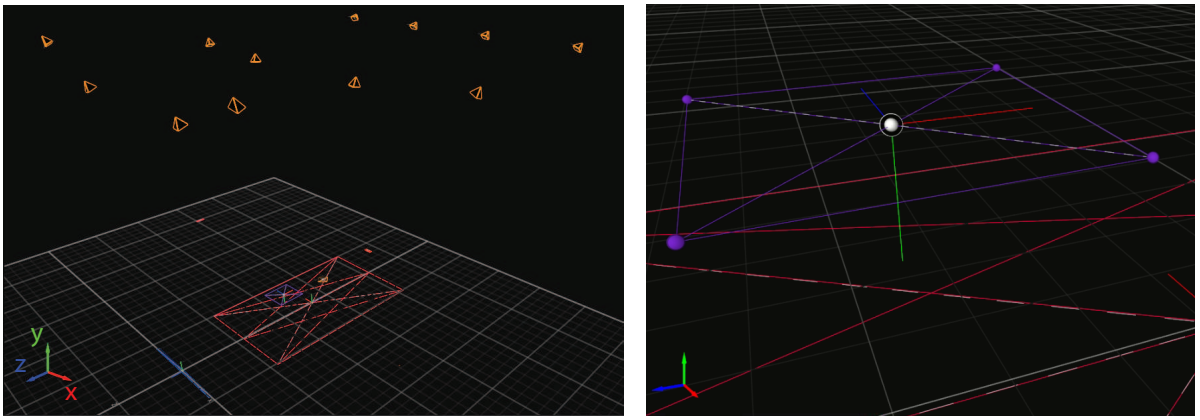

(a) Overview of the rigid bodies obtained in Motive (objects of different colours on the bottom) together with the calibrated camera system (orange objects on top).

(b) Detail of the rigid body representing the surface of the plate supporting the flexible plate (purple).

Figure A.4: Illustration of the rigid bodies obtained in the Motive software.

Bibliography

R. J. Adrian. Dynamic ranges of velocity and spatial resolution of particle image velocimetry. *Measurement Science and Technology*, 8(12):1393–1398, dec 1997. doi: 10.1088/0957-0233/8/12/003. URL https://doi.org/10.1088%2F0957-0233%2F8%2F12%2F003.

N. Agüera, G. Cafiero, T. Astarita, and S. Discetti. Ensemble 3d PTV for high resolution turbulent statistics. *Measurement Science and Technology*, 27(12):124011, oct 2016. doi: 10.1088/0957-0233/27/12/124011. URL https://doi.org/10.1088%2F0957-0233%2F27%2F12%2F124011.

J. Ballmann, A. Dafnis, H. Korsch, C. Buxel, H.-G. Reimerdes, K.-H. Brakhage, H. Olivier, C. Braun, A. Baars, and A. Boucke. *Experimental Analysis of high Reynolds Number structural Dynamics in ETW*. 2008. doi: 10.2514/6.2008-841. URL https://arc.aiaa.org/doi/abs/10.2514/6.2008-841.

R. Bleischwitz, R. de Kat, and B. Ganapathisubramani. On the fluid-structure interaction of flexible membrane wings for MAVs in and out of ground-effect. *Journal of Fluids and Structures*, 70:214 – 234, 2017. ISSN 0889-9746. doi: https://doi.org/10.1016/j.jfluidstructs.2016.12.001. URL http://www.sciencedirect.com/science/article/pii/S088997461630370X.

J. Bosbach, M. Kühn, and C. Wagner. Large scale particle image velocimetry with helium filled soap bubbles. *Experiments in Fluids*, 46(3):539–547, Mar 2009. ISSN 1432-1114. doi: 10.1007/s00348-008-0579-0. URL https://doi.org/10.1007/s00348-008-0579-0.

G. C. A. Caridi. *Development and Application of Helium-filled Soap Bubbles*. PhD thesis, Delft University of Technology, Mar 2018.

G. C. A. Caridi, D. Ragni, A. Sciacchitano, and F. Scarano. Hfsb-seeding for large-scale tomographic piv in wind tunnels. *Experiments in Fluids*, 57(12):190, Nov 2016. ISSN 1432-1114. doi: 10.1007/s00348-016-2277-7. URL https://doi.org/10.1007/s00348-016-2277-7.

A. R. Collar. The expanding domain of aeroelasticity. *The Journal of the Royal Aeronautical Society*, 50(428): 613–636, 1946. doi: 10.1017/S0368393100120358.

R. Del Rosario, J. M. Koudelka, R. Wahls, and N. Madavan. Nasa fixed wing project: Green technologies for future aircraft generation. https://ntrs.nasa.gov/archive/nasa/casi.ntrs.nasa.gov/20140012552.pdf, Jan 2014. Oral Presentation SciTech2014.

P. Deshpande and A. Modani. Experimental investigation of fluid–structure interaction in a bird-like flapping wing. *Journal of Fluids and Structures*, 91:102712, 2019. ISSN 0889-9746. doi: https://doi.org/10.1016/j.jfluidstructs.2019.102712. URL http://www.sciencedirect.com/science/article/pii/S0889974618310168.

European Commission. Flightpath 2050 europe's vision for aviation. https://www.acare4europe.org/sites/acare4europe.org/files/document/Flightpath2050_Final.pdf, 2011.

D. E. Faleiros, M. Tuinstra, A. Sciacchitano, and F. Scarano. Generation and control of helium-filled soap bubbles for piv. *Experiments in Fluids*, 60(3):40, Feb 2019. ISSN 1432-1114. doi: 10.1007/s00348-019-2687-4. URL https://doi.org/10.1007/s00348-019-2687-4.

S. Gesemann. From particle tracks to velocity and acceleration fields using b-splines and penalties, 2015.

C. Jux, A. Sciacchitano, J. F. G. Schneiders, and F. Scarano. Robotic volumetric PIV of a full-scale cyclist. *Experiments in Fluids*, 59(4):74, Apr 2018. ISSN 1432-1114. doi: 10.1007/s00348-018-2524-1. URL https://doi.org/10.1007/s00348-018-2524-1.

A. Kalmbach and M. Breuer. Experimental PIV/V3V measurements of vortex-induced fluid–structure interaction in turbulent flow—A new benchmark FSI-PfS-2a. *Journal of Fluids and Structures*, 42:369 – 387, 2013. ISSN 0889-9746. doi: https://doi.org/10.1016/j.jfluidstructs.2013.07.004. URL http://www.sciencedirect.com/science/article/pii/S0889974613001539.

S. Khosla, S. Murugappan, R. Paniello, J. Ying, and E. Gutmark. Role of vortices in voice production: Normal versus asymmetric tension. *The Laryngoscope*, 119(1):216–221, 2009. doi: 10.1002/lary.20026. URL https://onlinelibrary.wiley.com/doi/abs/10.1002/lary.20026.

P. Lancelot, J. Sodja, and R. De Breuker. Investigation of the unsteady flow over a wing under gust excitation. In *17th International Forum on Aeroelasticity and Structural Dynamics*, Jun 2017a. IFASD 2017 (Vol. 2017-June). [IFASD-2017-185] International Forum on Aeroelasticity and Structural Dynamics (IFASD).

P. Lancelot, J. Sodja, N. Werter, and R. De Breuker. Design and testing of a low subsonic wind tunnel gust generator. *Advances in Aircraft and Spacecraft Science*, 4(2):125–144, Mar 2017b. doi: 10.12989/aas.2017.4.2.125. URL http://dx.doi.org/10.12989/aas.2017.4.2.125.

LaVision. *DaVis 10.0 Software*. LaVision GmbH, Anna-Vandenhoeck-Ring 19, D-37081 Göttingen, 7 2018a. Product-Manual. Item-Number(s): 1105xxx.

LaVision. *FlowMaster Shake-the-Box (4D PTV)*. LaVision GmbH, Anna-Vandenhoeck-Ring 19, D-37081 Göttingen, 9 2018b. Product-Manual. Item-Number(s): 1105075.

L. E. M. Lignarolo. *On The Turbulent Mixing in Horizontal Axis Wind Turbine Wakes*. PhD thesis, Delft University of Technology, Apr 2016.

H. Mai, J. Neumann, and H. Hennings. Gust response: a validation experiment and preliminary numerical simulations. In *15th International Forum on Aeroelasticity and Structural Dynamics*, pages 1–20, 2011.

L. Marimon Giovannetti, J. Banks, S. R. Turnock, and S. W. Boyd. Uncertainty assessment of coupled Digital Image Correlation and Particle Image Velocimetry for fluid-structure interaction wind tunnel experiments. *Journal of Fluids and Structures*, 68:125 – 140, 2017. ISSN 0889-9746. doi: https://doi.org/10.1016/j.jfluidstructs.2016.09.002. URL http://www.sciencedirect.com/science/article/pii/S0889974615302231.

B. Martínez Gallar, B. W. van Oudheusden, A. Sciacchitano, and M. Karásek. Large-scale volumetric flow visualization of the unsteady wake of a flapping-wing micro air vehicle. *Experiments in Fluids*, 61(1):16, Dec 2019. ISSN 1432-1114. doi: 10.1007/s00348-019-2854-7. URL https://doi.org/10.1007/s00348-019-2854-7.

D. Ordóñez. Time-averaged pressure from robotic volumetric piv. Master's thesis, Delft University of Technology, 12 2018.

B. Pan, K. Qian, H. Xie, and A. Asundi. Two-dimensional digital image correlation for in-plane displacement and strain measurement: a review. *Measurement Science and Technology*, 20(6):062001, apr 2009. doi: 10.1088/0957-0233/20/6/062001. URL https://doi.org/10.1088%2F0957-0233%2F20%2F6%2F062001.

M. Raffel, C.E. Willert, F. Scarano, C.J. Kähler, S.T. Wereley, and J. Kompenhans. *Particle Image Velocimetry: A Practical Guide*. Experimental Fluid Mechanics. Springer International Publishing, 2018. ISBN 9783319688527. URL https://books.google.nl/books?id=wk9UDwAAQBAJ.

R. Ricketts. Experimental aeroelasticity - history, status and future in brief. In *31st Structures, Structural Dynamics and Materials Conference*, Structures, Structural Dynamics, and Materials and Co-located Conferences. American Institute of Aeronautics and Astronautics, Apr 1990. doi: 10.2514/6.1990-978. URL https://doi.org/10.2514/6.1990-978.

F. Scarano. Tomographic PIV: principles and practice. *Measurement Science and Technology*, 24(1):012001, oct 2012. doi: 10.1088/0957-0233/24/1/012001. URL https://doi.org/10.1088%2F0957-0233%2F24%2F1%2F012001.

F. Scarano, S. Ghaemi, G. C. A. Caridi, J. Bosbach, U. Dierksheide, and A. Sciacchitano. On the use of helium-filled soap bubbles for large-scale tomographic piv in wind tunnel experiments. *Experiments in Fluids*, 56 (2):42, Feb 2015. ISSN 1432-1114. doi: 10.1007/s00348-015-1909-7. URL https://doi.org/10.1007/s00348-015-1909-7.

D. Schanz, S. Gesemann, A. Schröder, B. Wieneke, and M. Novara. Non-uniform optical transfer functions in particle imaging: calibration and application to tomographic reconstruction. *Measurement Science and Technology*, 24(2):024009, dec 2012. doi: 10.1088/0957-0233/24/2/024009. URL https://doi.org/10.1088%2F0957-0233%2F24%2F2%2F024009.

D. Schanz, S. Gesemann, and A. Schröder. Shake-The-Box: Lagrangian particle tracking at high particle image densities. *Experiments in Fluids*, 57(5):70, Apr 2016. ISSN 1432-1114. doi: 10.1007/s00348-016-2157-1. URL https://doi.org/10.1007/s00348-016-2157-1.

J. F. G. Schneiders, I. Azijli, F. Scarano, and R. P. Dwight. Pouring time into space. In *11th International Symposium on Particle Image Velocimetry, PIV15, Santa Barbara, CA, USA, September 14-16 2015; Authors version*, 2015.

J. F. G. Schneiders, G. C. A. Caridi, A. Sciacchitano, and F. Scarano. Large-scale volumetric pressure from tomographic ptv with hfsb tracers. *Experiments in Fluids*, 57(11):164, Oct 2016. ISSN 1432-1114. doi: 10.1007/s00348-016-2258-x. URL https://doi.org/10.1007/s00348-016-2258-x.

J. F. G. Schneiders, F. Scarano, C. Jux, and A. Sciacchitano. Coaxial volumetric velocimetry. *Measurement Science and Technology*, 29(6):065201, apr 2018. doi: 10.1088/1361-6501/aab07d. URL https://doi.org/10.1088%2F1361-6501%2Faab07d.

D. M. Schuster, D. D. Liu, and L. J. Huttsell. Computational aeroelasticity: Success, progress, challenge. In *Collection of Technical Papers - AIAA/ASME/ASCE/AHS/ASC Structures, Structural Dynamics and Materials Conference*, volume 4, pages 2955–2977, 2003. URL https://www.scopus.com/inward/record.uri?eid=2-s2.0-0041509275&partnerID=40&md5=801d4119eed236b5fc9f5d8096d29485.

A. Sciacchitano and F. Scarano. Elimination of PIV light reflections via a temporal high pass filter. *Measurement Science and Technology*, 25(8):084009, jul 2014. doi: 10.1088/0957-0233/25/8/084009. URL https://doi.org/10.1088%2F0957-0233%2F25%2F8%2F084009.

W. Silva, B. Perry, J. Florance, M. Sanetrik, C. Wieseman, W. Stevens, C. Funk, J. Hur, D. Christhilf, and D. Coulson. *An Overview of the Semi-Span Super-Sonic Transport (S4T) Wind-Tunnel Model Program*. 2012. doi: 10.2514/6.2012-1552. URL https://arc.aiaa.org/doi/abs/10.2514/6.2012-1552.

A. Timpe, Z. Zhang, J. Hubner, and L. Ukeiley. Passive flow control by membrane wings for aerodynamic benefit. *Experiments in Fluids*, 54(3):1471, Feb 2013. ISSN 1432-1114. doi: 10.1007/s00348-013-1471-0. URL https://doi.org/10.1007/s00348-013-1471-0.

B. Wieneke. Volume self-calibration for 3d particle image velocimetry. *Experiments in Fluids*, 45(4):549–556, Oct 2008. ISSN 1432-1114. doi: 10.1007/s00348-008-0521-5. URL https://doi.org/10.1007/s00348-008-0521-5.

J. R. Wright and J. E. Cooper. *Introduction to Aircraft Aeroelasticity and Loads*. Aerospace Series. Wiley, 2014. ISBN 9781118700433. URL https://books.google.nl/books?id=nLzlBQAAQBAJ.

P. Zhang, S. D. Peterson, and Porfiri M. Combined particle image velocimetry/digital image correlation for load estimation. *Experimental Thermal and Fluid Science*, 100:207 – 221, 2019. ISSN 0894-1777. doi: https://doi.org/10.1016/j.expthermflusci.2018.09.011. URL http://www.sciencedirect.com/science/article/pii/S089417771831118X.